

# **Topological biases and feedbacks in proliferating tissues**

A dissertation presented

by

William Tyler Gibson

to

The Committee on Higher Degrees in Biophysics

in partial fulfillment of the requirements

for the degree of

Doctor of Philosophy

in the subject of

Biophysics

Harvard University  
Cambridge, Massachusetts

September, 2011

©2011, William Tyler Gibson  
All rights reserved.

## **Topological biases and feedbacks in proliferating tissues**

### **Abstract**

Development is often understood in terms of gene networks and deterministic decisions, yet the emergent, biophysical properties of a growing tissue are essential for its morphogenesis. These properties emerge stochastically and macroscopically, and cannot be explicitly encoded in the developmental-genetic program, even if that program is tuned to exploit them. Consequently, these properties are difficult to understand through the traditional logic of molecular-genetic analysis, requiring a complementary suite of mathematical approaches, simulations, and experiment. A case study in the constraints on biological form, the emergence of cell packing relationships in the context of a proliferating cell layer is perhaps one of the simplest such relationships in developmental biology. In this thesis, we investigate the processes underlying cell shape emergence along two principle axes. First, in the context of a packed, proliferating cell layer, we show that the polygonal shapes of individual cells can stochastically bias the cleavage plane orientations of their adjacent mitotic neighbors. Second, focusing on the population of dividing cells, we show using quantitative analysis that non-autonomous effects of neighboring cell divisions generate the characteristically shifted cell shape distribution for mitotic cells. Taken together, in the context of a local cellular neighborhood, this thesis identifies and characterizes a non-autonomous, bi-directional feedback between cell shape and cell division.

# Contents

Title Page .....	<i>i</i>
Abstract .....	<i>iii</i>
Table of Contents .....	<i>iv</i>
Citations to Previously Published Work .....	<i>v</i>
Acknowledgements .....	<i>vi</i>
<b>Chapter 1</b> .....	<b>1</b>
“Introduction and Background”	
<b>Chapter 2</b> .....	<b>23</b>
“Control of the mitotic cleavage plane by local epithelial topology”	
<b>Chapter 3</b> .....	<b>81</b>
“On the origins of the mitotic shift in proliferating cell layers”	
<b>Chapter 4</b> .....	<b>106</b>
“Implications and future directions”	
<b>Appendix A</b> .....	<b>113</b>
“Topological characterization of wing disc epithelia in <i>Dachsous</i> mutant animals”	
<b>Appendix B</b> .....	<b>123</b>
“Current and future directions for the Twin Spot Generator and Split Gal4 clone induction systems”	

## Citations to Previously Published Work

Paragraphs 1-7 and three of the figures from Chapter 1 have been previously published in the following review paper:

- Gibson, W., and Gibson, M. (2009). Cell topology, geometry, and morphogenesis in proliferating epithelia. *Current Topics in Developmental Biology* 89, 87-114.

Chapter 2 has been previously published in its entirety in the following journal paper:

- Gibson, W.T., Veldhuis, J.H., Rubinstein, B., Cartwright, H.N., Perrimon, N., Brodland, G.W., Nagpal, R., and Gibson, M.C. (2011). Control of the mitotic cleavage plane by local epithelial topology. *Cell* 144, 427-438.

## Acknowledgements

I would first especially like to thank my advisors Norbert and Radhika for their constant support, advice, and encouragement during my pre-doctoral training. I would also like to thank my collaborator Matthew Gibson for his constant support, which amounted to a role as a third advisor. I also thank my collaborator Boris Rubinstein, whose talent helped us to solve some of the problems described in this thesis. Additionally, I would like to thank my collaborators Wayne Brodland and James Veldhuis for their computational knowledge, assistance, and support; Ankit Patel for his innovative ideas and for paving the way for my dissertation; Heather Cartwright for her botanical skill and expertise; and Richard Binari for his instruction on *Drosophila* genetics. I would also like to thank the members of my Dissertation Advisory Committee – Professors Tim Mitchison, Clifford Tabin, Jacques Dumais, and Michael Brenner – for their helpful comments, constructive criticisms, academic advice, and general support. I am also especially grateful to Professor James Hogle and administrator Michele Jakoulov of the Harvard Biophysics Program, who have supported my scientific development from the beginning of graduate school to the end. In terms of day to day support, I would especially like to thank administrators Joanne Bourgeois, Laura Holderbaum, Lisa Mancini, and Lynnette Gutchewsky for their constant help and advice. I am also grateful to my classmates in the Harvard Biophysics Program for many interesting scientific discussions. Second to last but not least, I would like to thank my friends in the Perrimon, SSR, and Gibson labs, who created a non-competitive, collegial environment in which to pursue interesting scientific questions. Finally, I would like to thank my family and friends for their unwavering support, which helped me to complete this dissertation.

# **Chapter 1**

## **Introduction and Background**

**William T. Gibson<sup>1</sup> and Matthew C. Gibson<sup>2</sup>**

(1) Program in Biophysics, Harvard University (Cambridge, MA 02138, USA)

(2) Stowers Institute for Medical Research (Kansas City, MO 64110, USA)

## **Author contributions for Chapter 1**

Paper writing: WTG, with credit to MCG because paragraphs 1-7 are adapted from Gibson & Gibson (2009). Paragraphs 21-27 partly draw on material from Chapters 2-3.

**Summary:** Development is often understood in terms of gene networks and deterministic decisions, yet the emergent, biophysical properties of a growing tissue are essential for its morphogenesis. These properties emerge stochastically and macroscopically, and cannot be explicitly encoded in the developmental-genetic program, even if that program is tuned to exploit them. Consequently, these properties are difficult to understand through the traditional logic of molecular-genetic analysis, requiring a complementary suite of mathematical approaches, simulations, and experiment. A case study in the constraints on biological form, the emergence of cell packing relationships in the context of a proliferating cell layer is perhaps one of the simplest such relationships in developmental biology. In this thesis, we investigate the processes underlying cell shape emergence along two principle axes. First, in the context of a packed, proliferating cell layer, we show that the polygonal shapes of individual cells can stochastically bias the cleavage plane orientations of their adjacent mitotic neighbors. Second, focusing on the population of dividing cells, we show using quantitative analysis that non-autonomous effects of neighboring cell divisions generate the characteristically shifted cell shape distribution for mitotic cells. Taken together, in the context of a local cellular neighborhood, this thesis identifies and characterizes a non-autonomous, bi-directional feedback between cell shape and cell division. To place the work in context, here we provide a brief introduction to epithelial structure and morphogenesis, followed by an introduction to cellular topology. Next, we frame the thesis in terms of current models of cleavage plane orientation, and finally lay out the questions to be addressed in the Chapters 2 and 3.

### ***Introduction to epithelial structure and morphology***

The different types of epithelia are commonly classified by thickness, cellular morphology, and cellular connectivity. Simple epithelia are a single layer thick; stratified epithelia have two or more layers. Simple epithelia are typically classified as one of four types based on morphology of the component cells: squamous, cuboidal, columnar or pseudostratified. Squamous cells, for example, are shaped like flattened, interlocking polygonal plates or scales, whereas cuboidal cells are isometric in vertical section (Gray, 1995). Columnar cells have height to width ratios significantly greater than one, and like cuboidal cells, are polygonal when sectioned horizontally (Gray, 1995). There is one additional epithelial category (considered to be a simple epithelium), the pseudostratified type, where elongate, spindle-shaped cells inter-digitate their nuclei within the plane of the epithelium but nonetheless remain a monolayer (Wright and Alison, 1984). By analogy with the simple epithelia, the stratified epithelia also contain squamous, cuboidal, and columnar varieties. The critical difference between simple and stratified epithelia is that at least one layer of the latter category has lost contact with the basal lamina, and differentiated (Wright and Alison, 1984). For simplicity and analytical tractability, in this thesis we focus exclusively on simple columnar epithelia and the analogous structures in plants, monolayer epidermis.

While the essential features of epithelial construction are conserved among metazoa, there are clear differences in the architecture among different evolutionary clades (Knust and Bossinger, 2002; Tepass et al., 2001). The scope of animal epithelia

and plant epidermis covered here is sufficiently expansive that a full enumeration of the comparative structural differences is not possible. For purposes of illustration in discussing epithelial architecture, we place emphasis on *Drosophila* simple epithelia, which are particularly well characterized, both in terms of macroscopic and molecular structure.

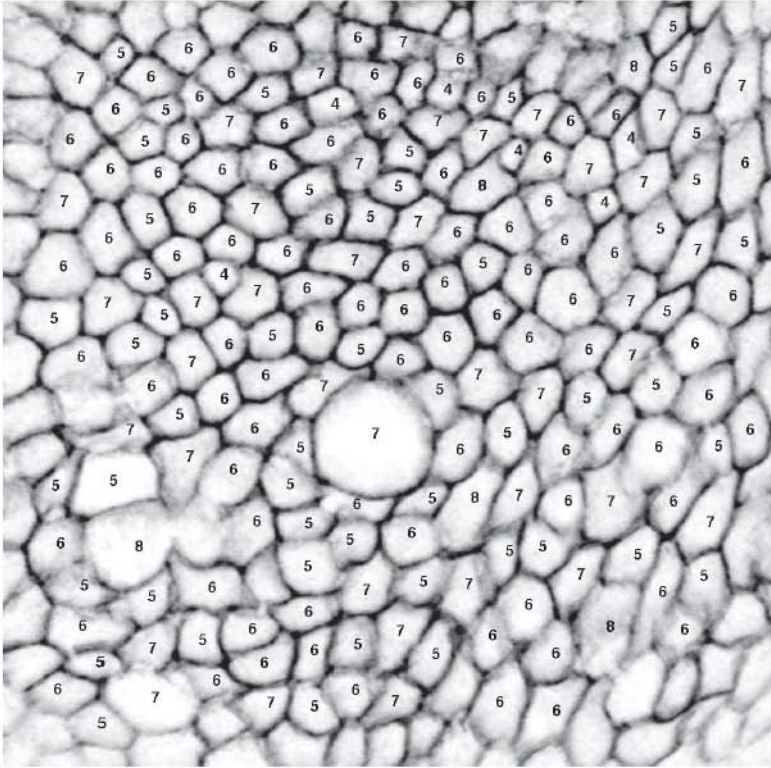
A primary feature of epithelia, in *Drosophila* and throughout the animal phyla, is cell polarization. Polarization, in turn, facilitates formation of a paracellular diffusion barrier, specialization of plasma membrane proteins, and directional transport in the form of secretion and absorption. The plasma membrane of each epithelial cell is divided into immiscible apical and basolateral domains (Tepass et al., 2001). Importantly, both the apical and the basal domains of the neighboring cells align with each other, endowing the epithelium with a globally faithful, local polarity. Separating the apical and basolateral domains is the zonula adherens (ZA), an adhesive belt encircling the cell (Knust and Bossinger, 2002). The apical zone is sub-divided into the apical surface and the marginal zone, a region of cell-cell contact apical to the ZA (Tepass et al., 2001). In *Drosophila*, septate junctions (SJs) lie basal to the ZA and constitute a paracellular permeability barrier, functionally analogous to the vertebrate tight junction (Bilder, 2001; Genova and Fehon, 2003; Gibson and Perrimon, 2003; Knust and Bossinger, 2002).

When sectioned apically, monolayer epithelial cells form ordered polygonal arrays, resembling a froth of soap bubbles (Figure 1.1 A-B). However, in pseudostratified epithelia, such as the *Drosophila* wing imaginal disc epithelium or that of the simple cnidarian *Nematostella vectensis*, the three-dimensional cellular geometry is considerably more complex below the level of the junctions. This cellular disorder can be attributed to the fact that the relatively large cell nuclei stochastically migrate along the apical-basal axis in concert with the cell cycle (Meyer et al., 2011). The mechanics of this process are particularly well understood in the case of the *Drosophila* wing disc. In the wing disc, during cell division, the nuclei are just beneath the apical surface, and the morphology of the dividing cell is almost spherical. The dividing cell thus deforms the apical geometries of its neighbors. Nevertheless, the contacts between neighboring cells tightly adhere and do not rearrange, in spite of the stretching and compression induced by their mitotic neighbor (Gibson et al., 2006). As a result, the interkinetic mode of cell division, reliant on cell cycle phase-coupled nuclear movements, has little effect on the polygonal geometry of the apical epithelial surface.

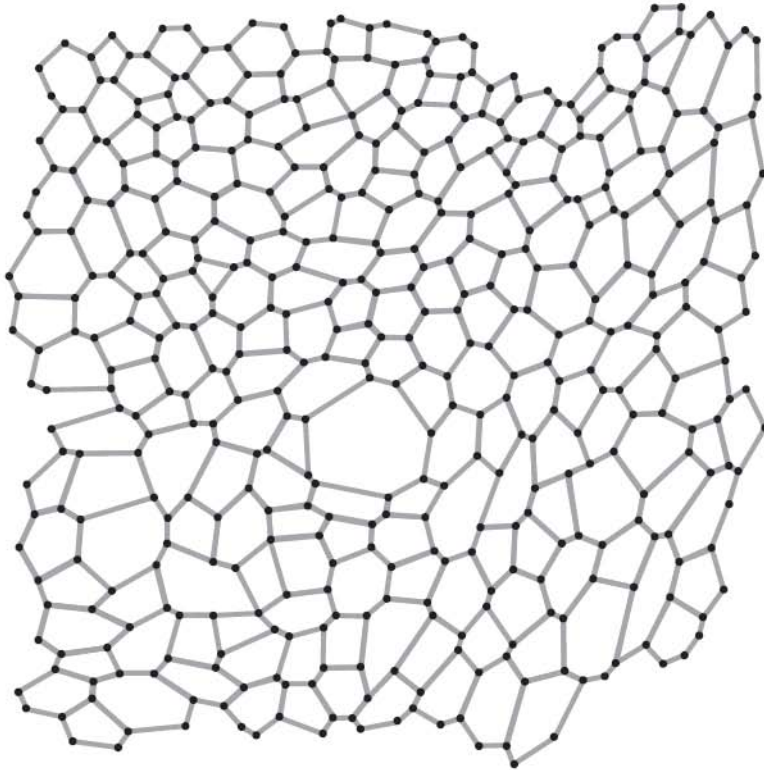
By comparison with the deformable cell contacts of animal epithelia, the geometry of plant epidermis appears to be simple, stiff, and regular, and without the complication of nuclear migration along the apical/basal axis. Cucumber epidermal cells, for example, have a slight apical curvature, and are either flat or have a shallow pyramidal point at the basal level. Overall, they are close to being simple, stiff, polygonal prisms (Lewis, 1928). In light of these fundamental structural differences, one might expect animal epithelia and plant epidermis to have very different cellular geometries. In fact, in apical cross section, their cellular geometries resemble one another to an unexpected degree.

Figure 1.1:

A



B



**Figure 1.1:** Epithelial topology at the level of cell-cell junctions. **(A)** An apical cross section through the pseudostratified *Drosophila* wing disc epithelium, stained with antibodies against the Septate Junction component Discs Large to outline cell boundaries. **(B)** A polygonal approximation to the apical section geometry. Note the presence of non-hexagonal cells.

## ***Introduction to cell topology***

In contrast to cellular geometry, which specifies cell shape, cellular topology instead refers to the connectivity among cells in a tissue. Intuitively, one can imagine stretching or deforming a sheet of cells in such a way that the cells' respective geometries change, but all neighbor relationships are preserved, thus preserving the sheet's topology. By

contrast, processes such as perforation or tearing, in which cell contacts are broken, or convergent extension, in which cell contacts are both made and broken, can change the sheet's topology significantly (Zallen and Zallen, 2004). In monolayer cell sheets, various elementary processes, such as cell division, cell rearrangement, and cell disappearance, can be shown to modify the topology of a cell sheet in stereotyped ways (Dubertret and Rivier, 1997). Moreover, in many biological systems, cell topology is expected to correlate with geometric variables, such as apical cellular surface area (Rivier and Lissowski, 1982). Therefore, as a first approximation to geometrically complex morphogenetic processes, topological descriptions can provide fundamental insight into how tissue-level connectivity emerges from elementary cellular transformations. This emergence, and the elementary transformations themselves, are directly observable for the case of a monolayer cell sheet. In this thesis, to facilitate analysis, we adopt simple, monolayer cell sheets as a model system. While simplistic, we anticipate that some of the properties uncovered in these simple, planar systems will also have analogues in multi-layered, three-dimensional tissues.

Having confined our analysis to mono-layer cell sheets, we first review and enumerate the strong constraints on cell shape imposed by the structure of a packed, polygonal cell layer. The first and most powerful constraint is that cells are adherent and space-filling, leaving no room for perforations. Therefore, the average area of a cell is simply the total area of the sheet,  $C$ , divided by the number of cells,  $F$ . The second constraint for a polygonal cell layer is that quaternary junctions are unstable. Specifically, we assume that at most, three cellular interfaces can meet at a point. Any quaternary junction at which four cellular interfaces meet is assumed to be transient and to resolve instantly into a pair of tri-cellular vertices (Rivier et al., 1995). The next constraint, which follows from the first two, is that the average number of neighbors for a cell is exactly six in the limit as the number of cells grows without bound (Graustein, 1931; Rivier et al., 1995). This result holds irrespective of the topology of the cell layer, whether for a torus, a sphere, or a plane (Rivier et al., 1995). Taken together, these are powerful constraints on the shapes of cells in a monolayer. In terms of maximum entropy theory, these constraints have been used to predict that the average area of a cell having  $N$  neighbors is linear in  $N$  (Lewis's law); that the many-sided and few-sided cells should anti-correlate in the tissue (the Aboav-Weaire law); and that there should be a universal relationship between the frequency of hexagonal cells and the second moment of the polygonal cell shape distribution (Lemaître's law) (Rivier et al., 1995). Remarkably, these relationships are observed across many different systems and species, confirming that elementary spatial constraints powerfully influence the packing arrangements and frequencies of polygonal cells (Lewis, 1928; Patel et al., 2009; Peshkin et al., 1991; Rivier et al., 1995).

While the constraints imposed by cell packing are strong enough to predict an approximate, binned-Gaussian estimate for the form of the distribution of cellular shapes, the field has not yet identified sufficiently many constraints to faithfully predict the true distribution of shapes, even allowing for a single tuning parameter (Rivier et al., 1995). Nevertheless, the empirical evidence strongly suggests that common principles are constraining the cell shape distributions of plant and animal cell layers. Such distributions are remarkably similar within select metazoan epithelia (differing by only a few percent), and are very similar between certain metazoans and some plant epidermis. From the metazoan epithelia of *Hydra*, *Drosophila*, and *Xenopus*, to the plant epidermis of *Cucumis*, *Allium*, and *Dryopteris*, the form of the distribution is unimodal with a hexagonal mode, just as the theory would predict (Gibson et al., 2006; Korn and Spalding, 1973; Lewis, 1928; Rivier et al., 1995). Yet the data diverge from the theory in that there is a pronounced asymmetry at equidistant intervals on either side of the hexagonal mode (Figure 1.2 A). For example, in both *Drosophila* and *Cucumis*, the frequency of pentagons is approximately 25%, whereas the frequency of heptagons is closer to 20%. Moving away from the mode by another unit, octagonal cells outnumber quadrilateral cells. Similarly, when we compare triangular and nonagonal frequencies (which are now three units from the mode), we find that the latter frequency vastly outnumbers the former. These eccentricities are reproducible both within and across select species, and may reflect fundamental constraints on cell shape emergence (see Chapter 3). Yet violations of this distribution certainly exist (Figure 1.2B). The plant *Anacharis* has a hexagonal frequency of nearly 60% (by comparison with most other systems, which exhibit hexagonal frequencies closer to 45%), and cell layers undergoing significant rearrangement, such as the *Drosophila* germ band, exhibit even more pronounced differences (Korn and Spalding, 1973; Zallen and Zallen, 2004). In order to reduce the complexity of the process of cell shape emergence, in this thesis, we will focus exclusively on cell layers exhibiting little to no rearrangement of cellular contacts, and for which mitosis is the dominant transformation.

Having narrowed our focus to cellular monolayers for which mitosis is the dominant transformation, we next consider the mitotic cell shape distribution, the origins and implications of which have long been a source of controversy in the field (Aegerter-Wilmsen et al., 2010; Dormer, 1980; Gibson et al., 2006; Gibson et al., 2011; Korn and Spalding, 1973; Lewis, 1943). The mitotic cell shape distribution has been characterized both in the epidermis of *Cucumis* and in the wing disc epithelium of *Drosophila* (Aegerter-Wilmsen et al., 2010; Gibson et al., 2006; Gibson et al., 2011; Lewis, 1928). For both systems (and especially in *Cucumis*), the mitotic cell shape distribution is almost identical to the overall cell shape distribution, but with one major difference. In particular, the distribution is shifted by an integer value such that the mode of the distribution is heptagonal, in contrast to the mode of the overall distribution of cell shapes, which is hexagonal (Gibson et al., 2006; Lewis, 1928). This *mitotic shift* is explored in depth in Chapter 3. First observed in 1928 by Frederick Lewis in the plant *Cucumis*, the shift reveals that in this tissue, cells having more sides are more likely to initiate mitosis per unit time (1928). Lewis later proposed that cells might become “especially apt” to divide (suggesting a causal relationship) following acquisition of additional neighbors due to neighboring cell divisions (Lewis, 1943). Reminiscent of this hypothesis, Aegerter-Wilmsen et al recently argued that mechanical feedback might

**Figure 1.2:**

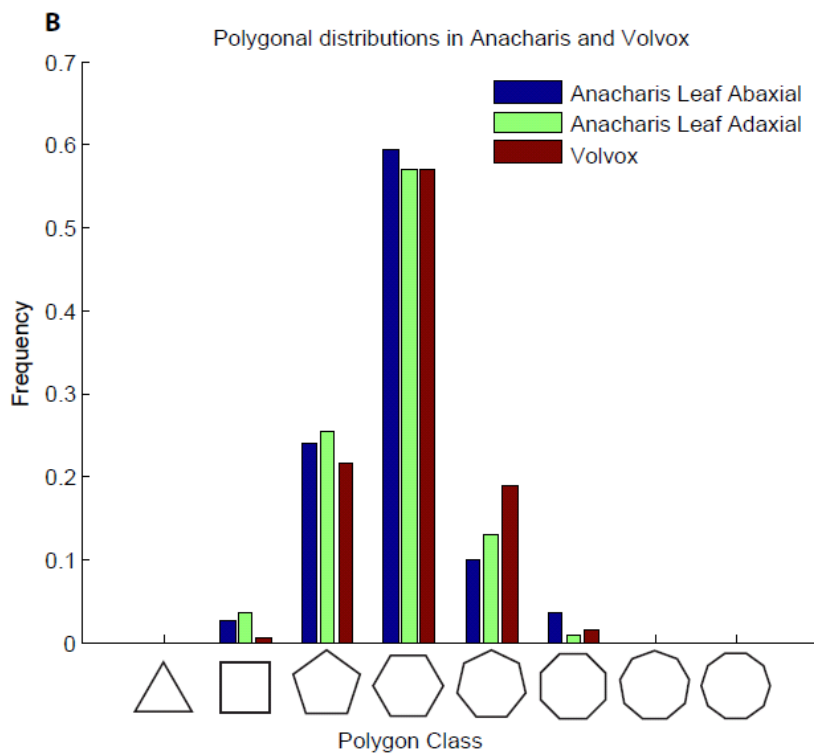
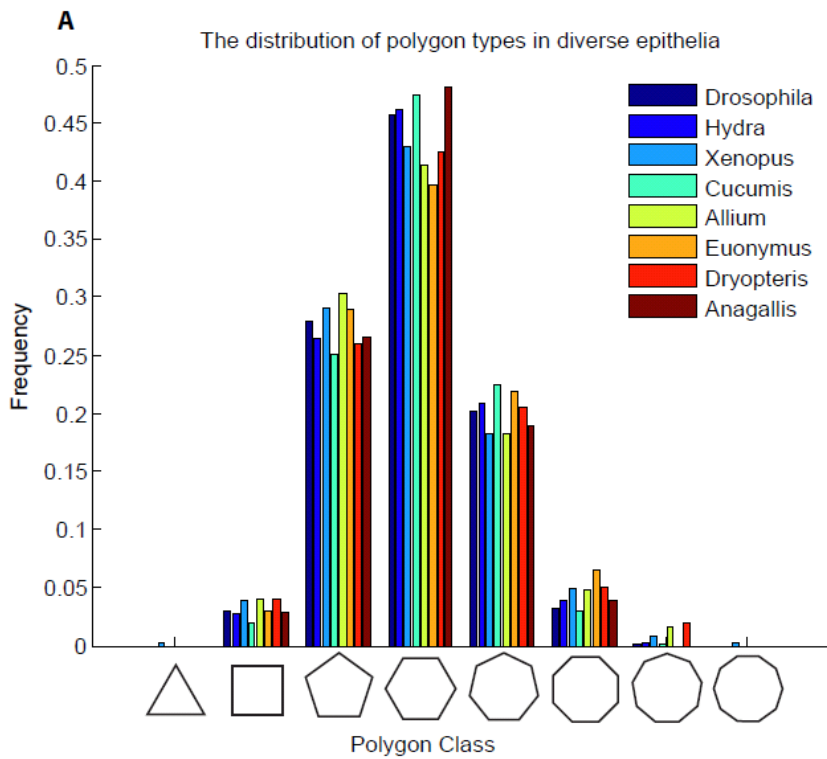


**Figure 1.2:** Distributions of cellular polygons in epithelia and plant epidermis. **(A)** The distribution of polygonal cell types in diverse animal epithelia and plant epidermis. Note the mode of hexagons, and the conservation of the general form in both plants and animals. **(B)** Two distributions of polygonal cell types that differ from the widely observed distribution seen in (A). Sources of data: *Drosophila*, *Hydra*, *Xenopus* (Gibson et al., 2006); *Cucumis* (Lewis, 1928); and *Allium*, *Dryopteris*, *Euonymus*, *Anacharis*, and *Volvox* (Korn and Spalding, 1973).

modulate the cell cycle in the polygonal cells of the *Drosophila* wing disc, which would cause increased division probability for higher order polygonal cells (2010). A simpler hypothesis is that the mitotic shift reflects side gaining over the course of the cell cycle. For each neighboring cell division, there is some probability that a cell will gain a new side, which occurs when the cleavage plane of the neighboring cell effectively cleaves their common interface, thus generating an additional polygonal neighbor. Multiple studies have suggested that this passive accumulation of new neighbor contacts may in fact generate the shift (Gibson et al., 2011; Korn and Spalding, 1973). Reinforcing this viewpoint, other studies have argued for an even simpler explanation, which is that the mitotic shift is actually an algebraic consequence of cell divisions having asynchronous cell cycle times. Dormer has shown mathematically that the average number of neighbors under these conditions is exactly seven for a dividing cell (1980). Other studies have developed a flux-balance equation to predict the mitotic distribution as a function of the overall cell shape distribution and also key parameters of mitosis (Rivier et al., 1995). While it is clear that passive effects and algebraic constraints play a strong role in producing the mitotic shift, it is not yet possible to rule out active, geometrically-based control of the cell cycle. In Chapter 3, we develop a computational framework that can in principle accommodate both influences, and which may facilitate analysis of whether active modulation is required for the shift.

Given that theoretical analysis has failed to uncover a simple derivation for the highly stereotyped form of the cell shape distribution in proliferating cell layers, and given the uncertainty about the origins and functional implications of the mitotic shift, the most natural approach for analyzing these systems is to develop models of the cell shape emergence process itself. To this end, numerous groups have developed mathematical, computational, and simulation-based models of proliferating cell layers (Aegerter-Wilmsen et al., 2010; Brodland and Veldhuis, 2002; Dubertret et al., 1998; Dubertret and Rivier, 1997; Farhadifar et al., 2007; Gibson et al., 2006; Korn and Spalding, 1973; Patel et al., 2009; Sahlin et al., 2009; Sahlin and Jonsson, 2010). Because we are focusing primarily on those models for which cell rearrangement and cell disappearance are completely absent, in this thesis we are concerned almost exclusively with division rules. Broadly defined, a division rule is an algorithm which specifies the shape and placement of the mitotic cleavage plane in a dividing cell. The inputs for a division rule might include cell signaling, cell mechanics, cell topology and cell geometry, among others. For simplicity, we assume that division rules do not interact with the division timing model, which determines the timing and frequency of mitosis. However, in principle, there is no reason that the two could not be coupled, either actively by biological control or passively by cell-cell mechanics.

### ***Models and paradigms for biological division rules and cell rounding, with applications to proliferative tissues***

In animal cells, the cleavage plane forms so as to orthogonally bisect the middle of the mitotic spindle (Grill and Hyman, 2005). By contrast, in plant cells, cytoskeletal structures designate the site of the future cleavage plane (Kost and Chua, 2002; Palevitz, 1987; Pickett-Heaps and Northcote, 1966; Sinnott and Bloch, 1940). Modern cell biology has extensively probed the molecular basis of cleavage plane orientation

(Buschmann et al., 2006; Fernandez-Minan et al., 2007; Johnston et al., 2009; Siller and Doe, 2009; Speicher et al., 2008; They et al., 2005; Traas et al., 1995; Vanstraelen et al., 2006; Walker et al., 2007; Wright et al., 2009). Yet the classical view of cleavage plane specification is based on cell geometry, whether via division orthogonal to the cellular long axis, via division in an orientation perpendicular to the previous direction of cleavage, or via division into equal areas according to an area-minimizing constraint (Besson and Dumais, 2011; Black and Vincent, 1988; Errera, 1886; Gray et al., 2004; Hertwig, 1893; Hofmeister, 1863; Minc et al., 2011; O'Connell and Wang, 2000; Strauss et al., 2006). More recent experiments involving manipulation of cell geometry have shown that HeLa cells are exquisitely sensitive to even small perturbations in cell shape during interphase. Indeed, cells plated on ECM micropatterns can be shown to follow mathematically predictable spindle orientations with respect to the shape of the plated pattern (They et al., 2007; They et al., 2005). Similarly, sea urchin embryos display highly predictable cleavage plane orientations and spindle orientations as a function of experimentally induced cellular geometries (Minc et al., 2011). These examples imply that the cell is able to effectively read its own planar pattern geometry, raising the question of how this is accomplished mechanistically (Flanders et al., 1990; Goodbody et al., 1991; Lloyd, 1991; Minc et al., 2011). Both the sea-urchin embryo and the plant *D. stramonium* have been suggested to use internal, tensile microtubules to read their cortical geometry (Flanders et al., 1990; Minc et al., 2011). Moreover, recent theoretical work suggests that maximum entropy considerations for cortical microtubule arrangements might generate the distribution of cleavage planes observed in plant cells (Besson and Dumais, 2011). An alternative hypothesis is that the cells of plants and animals are able to sense mechanical stress, and orient their mitotic cleavage planes in response to the stress field or to mechanical strain (Fink et al., 2011; Hamant et al., 2008; Lintilhac and Vesecky, 1984; Lynch and Lintilhac, 1997). While recent work has shown that HeLa cells use cortical stress fibers as mechanical inputs to orient the spindle, the actual motors moving the spindle in this system and in others may be sub-cortical, thus suggesting a combination of spatial and mechanical signals (Fink et al., 2011; Hamaguchi and Hiramoto, 1986; Wuhr et al., 2010). To conclude, the correlation between cell geometry and cleavage plane orientation is well-established on longer time scales, but the precise mechanisms and dynamics underlying this phenomenon are still being elucidated.

In addition to the dynamics occurring in the plane of the epithelium, in a wide variety of metazoan epithelia there are, as mentioned earlier, additional, cell-cycle dependent movements of the nuclei in the apical/basal direction (Meyer et al., 2011). Of particular interest in the plane of the epithelium is the deformation of a dividing cell and the process by which it compresses its neighbors just prior to cytokinesis. Termed “cell rounding,” this phenomenon is ubiquitous in metazoan epithelia (Meyer et al., 2011; They and Bornens, 2008). From the perspective of division plane orientation, cell rounding presents an obstacle to geometrical models of spindle orientation. In particular, the complex mechanical changes involved during the rounding process, when combined with the gross morphological shape changes, would appear to alter any pre-defined orientation and thus generate a randomly oriented cleavage plane. It is therefore intriguing that HeLa cells divide according to an axis determined not by the cell shape during mitosis – which is round – but rather by the shape of the cell before

the rounding took place (Thery et al., 2007; Thery et al., 2005). In Chapter 2, we describe an *in vivo* situation that approximately mirrors these dynamics. Specifically, for epithelial cells in the *Drosophila* wing disc, the best predictor of the eventual division plane orientation is the shape of the cell prior to cell rounding. Therefore, during cell rounding, the cell effectively remembers its interphase shape, and then places the cleavage furrow accordingly, both in HeLa cells and in the *Drosophila* wing disc epithelium. This form of cellular memory requires cortical stress fibers in HeLa cells (Fink et al., 2011). The mechanisms underlying such memory would be expected to indirectly contribute to cleavage plane control by coordinating the cleavage plane program with dynamic mechanical changes.

### **Cell division in a topological framework**

In order to analyze mitosis in the context of a packed, polygonal cell layer, we can express the process of cell division in terms of simple topological transformations. For analysis, we assume that cleavage planes cannot bisect an existing tri-cellular junction, and instead must form across cell edges so as to induce the creation of two new tri-cellular junctions (Figure 1.3). Under these conditions, the division of an  $m$ -sided topological cell always generates a pair of daughter cells having  $m+4$  sides in total. Yet different division rules will distribute these  $m+4$  sides differently. We can express the probability that a dividing  $m$ -sided cell gives rise to a daughter cell having an arbitrary number of sides in terms of the division kernel, which assigns probabilities to each daughter cell type. A rule giving rise to very topologically even divisions would be said to have a “tight” division kernel, by comparison with a rule for which daughter cell topologies are variable and more often dissimilar, which would be said to have a very “asymmetric” division kernel. In addition to generating daughter cells, mitosis also alters local topological relationships. When the cleavage plane of a mitotic cell bisects its shared common interface with two neighboring cells, each of the two neighbors gains an additional cell contact (see Figure 1.3). Whereas some division rules might stochastically bisect neighboring polygon classes in proportion to their frequency, other division rules might be biased in the direction of particular neighboring polygon classes. We can express the probability that the average neighboring  $N$ -sided cell is bisected by the cleavage plane in terms of the cleavage plane index, which is studied in depth in Chapter 2. Together, the division kernel and the cleavage plane index summarize the effects of cell division events on local topological relationships in the tissue.

Based on the division rules that have been explored in simulated cell sheets *in silico*, it is clear that the steady-state distribution of polygonal cell shapes can be quite sensitive to the division rules being implemented (Farhadifar et al., 2007; Patel et al., 2009; Sahlin et al., 2009; Sahlin and Jonsson, 2010). Intuitively, division rules having tighter division kernels produce cell shape distributions having reduced cell shape variance and an elevated frequency of hexagonal cells, because the daughter cell distribution is minimally variable at every step (Patel et al., 2009). Along similar lines, division rules for which the cleavage plane index is biased towards neighboring cells having fewer sides (Chapter 2) result in an increase in the frequency of hexagonal cells, because neighbor cells having fewer than six neighbors gain disproportionately many sides, whereas neighbor cells having more than six neighbors gain disproportionately

**Figure 1.3:**

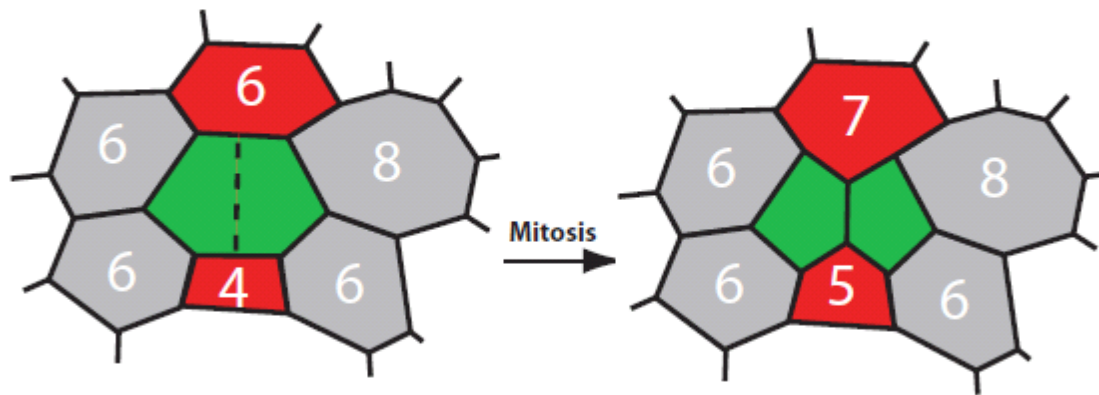


**Figure 1.3:** Mitosis in a polygonal cell. Following division of the central cell (*green*), the two neighboring cells abutting the cleavage plane (*red*) effectively gain one side each, transitioning from having 4 and 6 neighbors, respectively, to having 5 and 7 neighbors. Daughter cells of the division tend to have a lesser number of sides than the mother polygon.

few sides (Gibson et al., 2011; Patel et al., 2009). Geometrically, a very symmetrical division kernel corresponds to a division model in which the cleavage plane passes close to the center of mass (Sahlin and Jonsson, 2010). Moreover, biasing the cleavage plane towards polygonal cells having fewer neighbors corresponds to a model in which the cleavage plane is oriented orthogonal to the cellular long axis, which is believed to be a default mechanism in many plant and animal cells (Gibson et al., 2011; Hofmeister, 1863; O'Connell and Wang, 2000; Strauss et al., 2006). Based on the shapes of the cells in the tissue, it is also very clear that both the topology and the geometry of simulated cells are sensitive to the particular division rules being implemented (Farhadifar et al., 2007; Sahlin et al., 2009; Sahlin and Jonsson, 2010). Thus, division rules are important for maintaining both the cellular geometry and local topology in a population of dividing cells.

### ***The division timing model and cell shape evolution***

In addition to division rules, which constitute a potent mechanism by which a proliferating layer might control its topological variability by maximizing the frequency of hexagons, cell cycle control provides a complementary second mechanism. Recent studies using different division timing models show conflicting results regarding the ability of division rules to suppress shape variability, perhaps suggesting that these two influences have complex interactions (Gibson et al., 2011; Patel et al., 2009; Sahlin et al., 2009; Sahlin and Jonsson, 2010). In particular, division rules may be less powerful shape suppression mechanisms when they occur in cell layers for which division probability increases with polygon class, a phenomenon that has been demonstrated both in *Drosophila* and in the plant *Cucumis* (Gibson et al., 2011; Lewis, 1928; Patel et al., 2009). Cell cycle variability, which has been demonstrated using clone induction experiments in the *Drosophila* wing disc, is likely a causal factor in the emergence of correlations between polygon class and division probability (Milan et al., 1996). Specifically, variability in cell cycle times is what generates cell cycle asynchrony locally within the tissue. Cell cycle asynchrony, combined with a long cell cycle period, in turn, causes the fraction of cells undergoing mitosis per unit time to be low, measured to be on the order of 2% (Gibson et al., 2011; Milan et al., 1996). This low frequency of dividing cells permits the fraction of N-sided polygonal cells undergoing mitosis to differ dramatically from its respective tissue-level frequency. For instance, if all cells were to undergo mitosis simultaneously, as occurs in the *Drosophila* embryo, clearly there could be no difference between the fraction of dividing nonagons, and the overall fraction of nonagons (Lu et al., 2010). By contrast, in the *Drosophila* wing disc epithelium, or in the epidermis of *Cucumis*, a disproportionate number of nonagonal cells is undergoing mitosis compared with other polygon classes (Gibson et al., 2011; Lewis, 1928). Hence, while cell cycle variability does not necessarily drive suppression of cell shape variability, it certainly is a permissive factor.

As will be shown quantitatively in Chapter 3, cell cycle control also permits the existence of polygon-correlative division probabilities by providing a time delay. Recent work in the *Drosophila* wing disc suggests that this time delay (the cell cycle period) is set by a fold-change *Dpp* signaling threshold in the context of a dynamically scaled *Dpp* gradient (Wartlick et al., 2011). Intriguingly, in the absence of this time delay, no such

correlation would be expected to exist; instead, polygonal cells would be expected to divide in proportion to their frequency, and there would be no mitotic shift (Chapter 3). Thus, the existence of correlations between polygonal cell shape and division probability seems to occur in a region of intermediate cell cycle control and variability, being neither perfectly homogenous nor perfectly random.

To speculate, for the case of temporally randomized (or temporally synchronized) divisions, the frequencies of lower-order polygonal cell types might be expected to stabilize, because their relative division likelihoods would increase, thus increasing the chance that they would persist, especially for triangular and for quadrilateral cells, which, respectively, have daughter cells that are 50% and 100% quadrilateral under natural conditions (Gibson et al., 2011). Interestingly, previous work has suggested that the frequency of triangular cells increases when the mitosis promoting phosphatase *string* is over-expressed in the *Drosophila* wing imaginal disc (Gibson et al., 2006). Such cells would be expected to enter the cell cycle as quickly as possible, thus reducing both the time delay and the cell cycle variability. The only caveat to this data is that it was collected at a boundary between proliferating and non-proliferating cells, which could skew the results. While the dynamics of this process have not been fully characterized, this experiment suggests that alternative cell shape distributions might be achievable by adjusting the cell cycle variability and the cell cycle period.

### **Questions to be addressed in Chapter 2**

As early as the 19<sup>th</sup> century, cell biologists noted that the cells of plants and animals tend to follow stereotyped division rules with respect to cortical geometry (Besson and Dumais, 2011; Errera, 1886; Hertwig, 1893; Hofmeister, 1863; Minc et al., 2011; O'Connell and Wang, 2000; Strauss et al., 2006). Yet cell shape does not exist in isolation within a tissue. Instead, it is an emergent property of cell packing, growth, rearrangement, death, and indeed, cell division itself. In Chapter 2, we will consider how cell packing constrains cell division for the special case of a proliferating monolayer cell sheet in which the dominant transformation is cell division.

Using a simple mechanical model of epithelial cell geometry, we will show that fundamental packing constraints generate a robust correlation between the long axis orientation of a dividing cell and the polygonal shapes of its immediate neighbors. Based on a simple long-axis division rule, in the context of a cell layer this would predict that mitotic cleavage planes should be stochastically biased by local epithelial topology. In particular, we predict that mitotic cells should preferentially cleave their common interfaces with sub-hexagonal neighbors ( $N < 6$ ), and yet cleave common interfaces with super-hexagonal cells ( $N > 6$ ) at a disproportionately low frequency. Strikingly, analysis of both the *Drosophila* wing imaginal disc and the epidermis of the plant *Cucumis* confirms a strong correlation between cleavage plane orientation and local epithelial topology.

In order to verify that cells in the *Drosophila* wing disc approximately follow a long axis division rule, we performed time-lapse imaging of proliferating wing discs in *ex vivo* culture. Wing discs were mounted adjacent to air bubbles between a glass slide and cover slip in order to facilitate gas exchange. This technique eschews more technically

difficult tissue mounting techniques described elsewhere, and simultaneously traps the septate junctions in a narrow focal plane, thus facilitating imaging and analysis (Aldaz et al., 2010). Our live movies confirm that wing disc cells approximately obey a long-axis division mechanism, albeit with significant stochasticity.

We will next show that cleavage plane bias can be predicted from the angular constraints imposed by packing relationships among neighboring polygons, thus suggesting that cleavage plane bias is a truly topological effect that exists independent of neighbor cell size. We approximately confirmed this result using live imaging in the tissue. As a final consideration, we will examine the tissue-level impact of cleavage plane bias on cellular topology. In particular, consistent with intuition, we will show that hexagonal cell frequency is reduced by cleavage plane bias. Moreover, we will show that the shifted distribution of mitotic cell shapes is disrupted in the absence of bias. Thus, in addition to being a widespread property of cell layers, cleavage plane bias may play a role in generating both the mitotic shift (the subject of Chapter 3) and also the conserved distribution of cell shapes observed in many diverse multi-cellular organisms.

### **Questions to be addressed in Chapter 3**

First observed by F. T. Lewis in the cucumber in 1928, the characteristically shifted cell shape distribution for mitotic cells – which is otherwise identical to the overall distribution of cellular shapes – has been a subject of intense interest and debate since its discovery more than 80 years ago (Lewis, 1928). The reason for the mitotic distribution's heptagonal mean, which contrasts with the hexagonal mean for the overall cell shape distribution, has at various times been attributed to algebraic constraints, to flux-balance requirements, to side-gaining due to neighboring cell divisions, and most recently, to a hypothesized stress-induced feedback on the cell cycle (Dormer, 1980; Gibson et al., 2011; Korn and Spalding, 1973; Lewis, 1943; Rivier et al., 1995). In Chapter 3, we will examine the origins and implications of this *mitotic shift*, with emphasis on biological significance.

To test whether cellular memory is required to generate the mitotic shift, we will first examine a memoryless division process in which mitosis occurs with constant probability per time interval. Interestingly, we will find that a mitotic shift is impossible under these conditions. Thus, a time delay between mitoses, in this case provided by the cell cycle period, is required for the shift. It can also be shown that the mitotic shift would be absent for the case of completely synchronous divisions. Hence, a mitotic shift can exist neither for perfectly random nor for perfectly controlled division cycles, and must inhabit the region between these limiting cases.

Previous studies have invoked both cell autonomous and cell non-autonomous mechanisms to explain the shift. In order to probe the relative contributions of these two influences, we will develop a framework in which to compute the emergent form of the mitotic shift in terms of both polygon specific division likelihoods and side-gaining events due to neighboring cell divisions. Consistent with our findings that a time delay following mitosis is required for the shift, we will find that division likelihood functions that increase with polygon class best match the empirical data from *Drosophila* and from *Cucumis*. Yet it is unclear whether this type of likelihood function reflects

exclusively cell non-autonomous effects, or whether it also reflects shape-dependent feedback on the cell cycle state of a polygonal cell. To distinguish between these two scenarios, future work may permit computation of the likelihood function in terms of specific assumptions about the timing model and the division rules being implemented. Currently, we can show that the non-autonomous effects of neighboring cell divisions are responsible for much of the shift, but cannot rule out the possibility of shape-dependent feedback.

As a final consideration, we will address the functional implications of the mitotic shift. Specifically, for the idealized case of a perfect shift, we will identify strong constraints on any cell shape distribution that could exhibit both an increasing division likelihood function and a mitotic shift. Using cell shape distributions collected from the monolayer cell sheets of diverse taxa, we will then verify that the majority of such systems obey the identified constraints. Broad conservation of the cell shape distribution has been noted previously, but this analysis (combined with the findings from Chapter 2) may suggest that the form of the distribution may reflect fundamental constraints on cell shape emergence via mitosis.

## Chapter 1 References

- Aegerter-Wilmsen, T., Smith, A.C., Christen, A.J., Aegerter, C.M., Hafen, E., and Basler, K. (2010). Exploring the effects of mechanical feedback on epithelial topology. *Development* *137*, 499-506.
- Aldaz, S., Escudero, L.M., and Freeman, M. (2010). Live imaging of *Drosophila* imaginal disc development. *Proc Natl Acad Sci U S A* *107*, 14217-14222.
- Besson, S., and Dumais, J. (2011). Universal rule for the symmetric division of plant cells. *Proc Natl Acad Sci U S A* *108*, 6294-6299.
- Bilder, D. (2001). PDZ proteins and polarity: functions from the fly. *Trends Genet* *17*, 511-519.
- Black, S.D., and Vincent, J.P. (1988). The first cleavage plane and the embryonic axis are determined by separate mechanisms in *Xenopus laevis*. II. Experimental dissociation by lateral compression of the egg. *Dev Biol* *128*, 65-71.
- Brodland, G.W., and Veldhuis, J.H. (2002). Computer simulations of mitosis and interdependencies between mitosis orientation, cell shape and epithelia reshaping. *J Biomech* *35*, 673-681.
- Buschmann, H., Chan, J., Sanchez-Pulido, L., Andrade-Navarro, M.A., Doonan, J.H., and Lloyd, C.W. (2006). Microtubule-associated AIR9 recognizes the cortical division site at preprophase and cell-plate insertion. *Curr Biol* *16*, 1938-1943.
- Dormer, K.J. (1980). *Fundamental tissue geometry for biologists* (Cambridge, UK, Cambridge University Press).
- Dubertret, B., Aste, T., Ohlenbusch, H.M., and Rivier, N. (1998). Two-dimensional froths and the dynamics of biological tissues. *Physical Review E* *58*, 6368-6378.
- Dubertret, B., and Rivier, N. (1997). The renewal of the epidermis: a topological mechanism. *Biophys J* *73*, 38-44.
- Errera, L. (1886). Sur une condition fondamentale d'équilibre des cellules vivantes. *Comptes Rendus Hebdomadaires des Seances de l'Academie des Sciences* *103*, 822-824.
- Farhadifar, R., Roper, J.C., Aigouy, B., Eaton, S., and Julicher, F. (2007). The influence of cell mechanics, cell-cell interactions, and proliferation on epithelial packing. *Curr Biol* *17*, 2095-2104.
- Fernandez-Minan, A., Martin-Bermudo, M.D., and Gonzalez-Reyes, A. (2007). Integrin signaling regulates spindle orientation in *Drosophila* to preserve the follicular-epithelium monolayer. *Curr Biol* *17*, 683-688.
- Fink, J., Carpi, N., Betz, T., Betard, A., Chebah, M., Azioune, A., Bornens, M., Sykes, C., Fetler, L., Cuvelier, D., *et al.* (2011). External forces control mitotic spindle positioning. *Nat Cell Biol* *13*, 771-778.
- Flanders, D.J., Rawlins, D.J., Shaw, P.J., and Lloyd, C.W. (1990). Nucleus-associated microtubules help determine the division plane of plant epidermal cells: avoidance of four-way junctions and the role of cell geometry. *J Cell Biol* *110*, 1111-1122.
- Genova, J.L., and Fehon, R.G. (2003). Neuroglian, Gliotactin, and the Na<sup>+</sup>/K<sup>+</sup> ATPase are essential for septate junction function in *Drosophila*. *J Cell Biol* *161*, 979-989.
- Gibson, M.C., Patel, A.B., Nagpal, R., and Perrimon, N. (2006). The emergence of geometric order in proliferating metazoan epithelia. *Nature* *442*, 1038-1041.
- Gibson, M.C., and Perrimon, N. (2003). Apicobasal polarization: epithelial form and function. *Curr Opin Cell Biol* *15*, 747-752.
- Gibson, W., and Gibson, M. (2009). Cell topology, geometry, and morphogenesis in proliferating epithelia. *Current Topics in Developmental Biology* *89*, 87-114.
- Gibson, W.T., Veldhuis, J.H., Rubinstein, B., Cartwright, H.N., Perrimon, N., Brodland, G.W., Nagpal, R., and Gibson, M.C. (2011). Control of the mitotic cleavage plane by local epithelial topology. *Cell* *144*, 427-438.

Goodbody, K.C., Venverloo, C.J., and Lloyd, C.W. (1991). Laser microsurgery demonstrates that cytoplasmic strands anchoring the nucleus across the vacuole of premitotic plant cells are under tension. Implications for division plane alignment. *Development* 1991, 931-939.

Graustein, W.C. (1931). On the Average Number of Sides of Polygons of a Net. *The Annals of Mathematics, Second Series* 32, 149-153.

Gray, D., Plusa, B., Piotrowska, K., Na, J., Tom, B., Glover, D.M., and Zernicka-Goetz, M. (2004). First cleavage of the mouse embryo responds to change in egg shape at fertilization. *Curr Biol* 14, 397-405.

Gray, H. (1995). *Gray's anatomy: the anatomical basis of medicine and surgery* (New York: Edinburgh, Churchill Livingstone).

Grill, S.W., and Hyman, A.A. (2005). Spindle positioning by cortical pulling forces. *Dev Cell* 8, 461-465.

Hamaguchi, M.S., and Hiramoto, Y. (1986). Analysis of the Role of Astral Rays in Pronuclear Migration in Sand Dollar Eggs by the Colcemid-Uv Method. *Dev Growth Differ* 28, 143-156.

Hamant, O., Heisler, M.G., Jonsson, H., Krupinski, P., Uyttewaal, M., Bokov, P., Corson, F., Sahlin, P., Boudaoud, A., Meyerowitz, E.M., *et al.* (2008). Developmental patterning by mechanical signals in Arabidopsis. *Science* 322, 1650-1655.

Hertwig, O. (1893). Ueber den Werth der ersten Furchungszellen für die Organbildung des Embryo Experimentelle Studien am Frosch-und Tritonei. *Archiv für Mikroskopische Anatomie* 42, 662-807.

Hofmeister, W. (1863). Zusätze und Berichtigungen zu den 1851 veröffentlichten Untersuchungen der Entwicklung höherer Kryptogamen. *Jahrbucher für Wissenschaft und Botanik* 3, 259-293.

Johnston, C.A., Hirono, K., Prehoda, K.E., and Doe, C.Q. (2009). Identification of an Aurora-A/PinsLINKER/Dlg spindle orientation pathway using induced cell polarity in S2 cells. *Cell* 138, 1150-1163.

Knust, E., and Bossinger, O. (2002). Composition and formation of intercellular junctions in epithelial cells. *Science* 298, 1955-1959.

Korn, R.W., and Spalding, R.M. (1973). The Geometry of Plant Epidermal Cells. *New Phytologist* 72, 1357-1365.

Kost, B., and Chua, N.H. (2002). The plant cytoskeleton: Vacuoles and cell walls make the difference. *Cell* 108, 9-12.

Lewis, F.T. (1928). The Correlation Between Cell Division and the Shapes and Sizes of Prismatic Cells in the Epidermis of Cucumis. *The Anatomical Record* 38, 341-376.

Lewis, F.T. (1943). The geometry of growth and cell division in epithelial mosaics. *Am J Bot* 30, 766-776.

Lintilhac, P.M., and Vesecky, T.B. (1984). Stress-induced alignment of division plane in plant tissues grown *in vitro*. *Nature* 307, 363-364.

Lloyd, C.W. (1991). How Does the Cytoskeleton Read the Laws of Geometry in Aligning the Division Plane of Plant-Cells. *Development*, 55-65.

Lu, X., Drocco, J., and Wieschaus, E.F. (2010). Cell cycle regulation via inter-nuclear communication during the early embryonic development of *Drosophila melanogaster*. *Cell Cycle* 9, 2908-2910.

Lynch, T.M., and Lintilhac, P.M. (1997). Mechanical signals in plant development: a new method for single cell studies. *Dev Biol* 181, 246-256.

Meyer, E.J., Ikmi, A., and Gibson, M.C. (2011). Interkinetic nuclear migration is a broadly conserved feature of cell division in pseudostratified epithelia. *Curr Biol* 21, 485-491.

Milan, M., Campuzano, S., and Garcia-Bellido, A. (1996). Cell cycling and patterned cell proliferation in the wing primordium of *Drosophila*. *Proc Natl Acad Sci U S A* 93, 640-645.

Minc, N., Burgess, D., and Chang, F. (2011). Influence of cell geometry on division-plane positioning. *Cell* 144, 414-426.

O'Connell, C.B., and Wang, Y.L. (2000). Mammalian spindle orientation and position respond to changes in cell shape in a dynein-dependent fashion. *Mol Biol Cell* 11, 1765-1774.

Palevitz, B.A. (1987). Actin in the Preprophase Band of *Allium-Cepa*. *Journal of Cell Biology* 104, 1515-1519.

Patel, A.B., Gibson, W.T., Gibson, M.C., and Nagpal, R. (2009). Modeling and inferring cleavage patterns in proliferating epithelia. *PLoS Comput Biol* 5, e1000412.

Peshkin, M.A., Strandburg, K.J., and Rivier, N. (1991). Entropic predictions for cellular networks. *Phys Rev Lett* 67, 1803-1806.

Pickett-Heaps, J.D., and Northcote, D.H. (1966). Organization of microtubules and endoplasmic reticulum during mitosis and cytokinesis in wheat meristems. *J Cell Sci* 1, 109-120.

Rivier, N., and Lissowski, A. (1982). On the correlation between sizes and shapes of cells in epithelial mosaics. *J Phys A: Math Gen* 15, L143-L148.

Rivier, N., Schliecker, G., and Dubertret, B. (1995). The stationary state of epithelia. *Acta Biotheoretica* 43, 403-423.

Sahlin, P., Hamant, O., and Jönsson, H. (2009). Statistical Properties of Cell Topology and Geometry in a Tissue-Growth Model In *Complex Sciences: First International Conference, Complex 2009, Shanghai, China, February 23-25, 2009 Revised Papers, Part 1*, J. Zhou, ed. (Springer Berlin Heidelberg), pp. 971-979.

Sahlin, P., and Jonsson, H. (2010). A modeling study on how cell division affects properties of epithelial tissues under isotropic growth. *PLoS One* 5, e11750.

Siller, K.H., and Doe, C.Q. (2009). Spindle orientation during asymmetric cell division. *Nat Cell Biol* 11, 365-374.

Sinnott, E.W., and Bloch, R. (1940). Cytoplasmic behavior during division of vacuolate plant cells. *P Natl Acad Sci USA* 26, 223-227.

Speicher, S., Fischer, A., Knoblich, J., and Carmena, A. (2008). The PDZ protein Canoe regulates the asymmetric division of *Drosophila* neuroblasts and muscle progenitors. *Curr Biol* 18, 831-837.

Strauss, B., Adams, R.J., and Papalopulu, N. (2006). A default mechanism of spindle orientation based on cell shape is sufficient to generate cell fate diversity in polarised *Xenopus* blastomeres. *Development* 133, 3883-3893.

Tepass, U., Tanentzapf, G., Ward, R., and Fehon, R. (2001). Epithelial cell polarity and cell junctions in *Drosophila*. *Annu Rev Genet* 35, 747-784.

Thery, M., and Bornens, M. (2008). Get round and stiff for mitosis. *HFSP J* 2, 65-71.

Thery, M., Jimenez-Dalmaroni, A., Racine, V., Bornens, M., and Julicher, F. (2007). Experimental and theoretical study of mitotic spindle orientation. *Nature* 447, 493-496.

Thery, M., Racine, V., Pepin, A., Piel, M., Chen, Y., Sibarita, J.B., and Bornens, M. (2005). The extracellular matrix guides the orientation of the cell division axis. *Nat Cell Biol* 7, 947-953.

Traas, J., Bellini, C., Nacry, P., Kronenberger, J., Bouchez, D., and Caboche, M. (1995). Normal Differentiation Patterns in Plants Lacking Microtubular Preprophase Bands. *Nature* 375, 676-677.

Vanstraelen, M., Van Damme, D., De Rycke, R., Mylle, E., Inze, D., and Geelen, D. (2006). Cell cycle-dependent targeting of a kinesin at the plasma membrane demarcates the division site in plant cells. *Current Biology* 16, 308-314.

Walker, K.L., Muller, S., Moss, D., Ehrhardt, D.W., and Smith, L.G. (2007). Arabidopsis TANGLED identifies the division plane throughout mitosis and cytokinesis. *Curr Biol* 17, 1827-1836.

Wartlick, O., Mumcu, P., Kicheva, A., Bittig, T., Seum, C., Julicher, F., and Gonzalez-Gaitan, M. (2011). Dynamics of Dpp signaling and proliferation control. *Science* 331, 1154-1159.

Wright, A.J., Gallagher, K., and Smith, L.G. (2009). discordia1 and alternative discordia1 function redundantly at the cortical division site to promote preprophase band formation and orient division planes in maize. *Plant Cell* 21, 234-247.

Wright, N., and Alison, M. (1984). *The biology of epithelial cell populations* (New York, Oxford University Press).

Wuhr, M., Tan, E.S., Parker, S.K., Detrich, H.W., 3rd, and Mitchison, T.J. (2010). A model for cleavage plane determination in early amphibian and fish embryos. *Curr Biol* 20, 2040-2045.

Zallen, J.A., and Zallen, R. (2004). Cell-pattern disordering during convergent extension in *Drosophila*. *Journal of Physics: Condensed Matter* 16, S5073-S5080.

## **Chapter 2**

# **Control of the mitotic cleavage plane by local epithelial topology**

**William T. Gibson<sup>1-2,4-5</sup>, James H. Veldhuis<sup>3</sup>, Boris Rubinstein<sup>2</sup>, Heather N. Cartwright<sup>2</sup>, Norbert Perrimon<sup>4</sup>, G. Wayne Brodland<sup>3</sup>, Radhika Nagpal<sup>5</sup>, and Matthew C. Gibson<sup>2,6</sup>**

(1) Program in Biophysics, Harvard University (Cambridge, MA 02138, USA)

(2) Stowers Institute for Medical Research (Kansas City, MO 64110, USA)

(3) Department of Civil and Environmental Engineering, University of Waterloo (Waterloo, ON N2L 3G1, Canada)

(4) Department of Genetics, Howard Hughes Medical Institute, Harvard Medical School (Boston, MA 02115, USA)

(5) School of Engineering & Applied Sciences, Harvard University (Cambridge, MA 02138, USA)

(6) Department of Anatomy and Cell Biology, Kansas University Medical Center (Kansas City 64110, KS)

## Author contributions for Chapter 2

Supervision of research: MCG, RN, BR, NP, GWB.

Paper writing: WTG, MCG, RN.

Figures: WTG, MCG, RN.

Mechanical relaxation algorithm & analysis: WTG

Analytical computations: BR, WTG, RN

Data collection & analysis: WTG

Sample preparation & imaging: WTG (*Drosophila*) & HNC (*Cucumis*)

Topological simulations: WTG & JHV

Finite element simulations: JHV, WTG, & GWB

## SUMMARY

For nearly 150 years, it has been recognized that cell shape strongly influences the orientation of the mitotic cleavage plane (e.g. Hofmeister, 1863). However, we still understand little about the complex interplay between cell shape and cleavage plane orientation in epithelia, where polygonal cell geometries emerge from multiple factors, including cell packing, cell growth, and cell division itself. Here, using mechanical simulations, we show that the polygonal shapes of individual cells can systematically bias the long axis orientations of their adjacent mitotic neighbors. Strikingly, analysis of both animal epithelia and plant epidermis confirm a robust and nearly identical correlation between local cell topology and cleavage plane orientation *in vivo*. Using simple mathematics, we show that this effect derives from fundamental packing constraints. Our results suggest that local epithelial topology is a key determinant of cleavage plane orientation, and that cleavage plane bias may be a widespread property of polygonal cell sheets in plants and animals.

## HIGHLIGHTS

- Neighbor cell topology biases cleavage plane orientation in monolayer cell sheets.
- This “cleavage plane bias” is observed in both plants and animals.
- This effect can be explained by fundamental packing constraints.
- Cleavage plane bias influences global epithelial topology.

## INTRODUCTION

The active control of the mitotic cleavage plane is crucial to numerous processes, and the consequences of cleavage plane mis-orientation can be catastrophic, ranging from polycystic kidney disease and organ malformation to tumorigenesis (Baena-Lopez et al., 2005; Fischer et al., 2006; Gong et al., 2004; Quyn et al., 2010; Saburi et al., 2008). Although the control of cleavage plane orientation is usually understood from a molecular viewpoint (Buschmann et al., 2006; Fernandez-Minan et al., 2007; Johnston et al., 2009; Siller and Doe, 2009; Speicher et al., 2008; They et al., 2005; Traas et al., 1995; Vanstraelen et al., 2006; Walker et al., 2007; Wright et al., 2009), more than a century of observations show that mitotic cells in both plants and animals tend to divide orthogonal to their geometric long axis as a default mechanism (Gray et al., 2004; Hofmeister, 1863; O'Connell and Wang, 2000; Strauss et al., 2006). In plants, the geometric location of the division plane can be predicted by cytoskeletal structures (Kost and Chua, 2002; Palevitz, 1987; Pickett-Heaps and Northcote, 1966; Sinnott and Bloch, 1940), and biophysical experiments suggest that the cytoskeleton may be involved in the process of orienting the division

plane as dictated by cell geometry (Flanders et al., 1990; Goodbody et al., 1991; Katsuta et al., 1990; Lloyd, 1991). Further, in animal cells, recent studies implicate the geometry of cell-matrix adhesions as a key determinant of cleavage plane orientation (They et al., 2007; They et al., 2005). Cell geometry is thus a critical determinant of cleavage plane orientation, at both the molecular and biophysical level.

While the regulation of mitotic cleavage plane orientation by geometric cues has been extensively probed in unicellular systems, far less attention has been given to adherent epithelial and epidermal layers. In this context, cell geometry does not exist in isolation, because cell shapes emerge from the combined effects of growth, mitosis, and cellular packing. *A priori*, this complex interplay of biological processes, and the diverse genetic programs that have evolved to control them in plants and animals, would appear to suggest a staggering range of possible cell geometries within an epithelium. However, spatial considerations impose powerful constraints on the shapes of cells in monolayer sheets, from the distribution of polygonal cell types (Rivier et al., 1995) to their neighbor correlations (Peshkin et al., 1991) and relative sizes (Rivier and Lissowski, 1982). Indeed, empirical investigation confirms that many monolayer cell sheets across the plant and animal kingdoms converge on a default equilibrium distribution of cellular shapes, with approximately 45% hexagons, 25% pentagons, and 20% heptagons (Dubertret and Rivier, 1997; Gibson et al., 2006; Korn and Spalding, 1973; Lewis, 1928). Such clear conservation of cellular network architecture raises the question as to whether conserved cellular division mechanisms are responsible for generating such similar packing arrangements of cells, as recent computational studies have posited (Dubertret et al., 1998; Gibson et al., 2006; Korn and Spalding, 1973; Miri and Rivier, 2006; Patel et al., 2009). The strongest evidence to date that common mechanisms are used among plants and animals to generate conserved packing relationships can be found in the *mitotic shift*, wherein the distribution of mitotic cell shapes is shifted by a single polygon class to have a heptagonal mean, as opposed to a hexagonal mean as seen in interphase cells.

Here, we use computational modeling, experimental observation, and mathematical analysis to report that, as a default property, neighbor cell shape can strongly bias cleavage plane orientation in the monolayer cell sheets of both plants and animals. Intriguingly, we show that this bias increases the structural regularity of an epithelium by increasing the frequency of hexagons. Our analysis indicates that simultaneously, cleavage plane bias is also involved in specifying the mitotic shift. The mechanism through which cleavage plane bias accomplishes these effects is differential side-gaining, whereby dividing cells preferentially cleave their common interfaces with sub-hexagonal cells such as quadrilaterals, and avoid cleaving their common interfaces with super-hexagonal cells such as octagons. Together, our results suggest a common emergent

Figure 2.1:

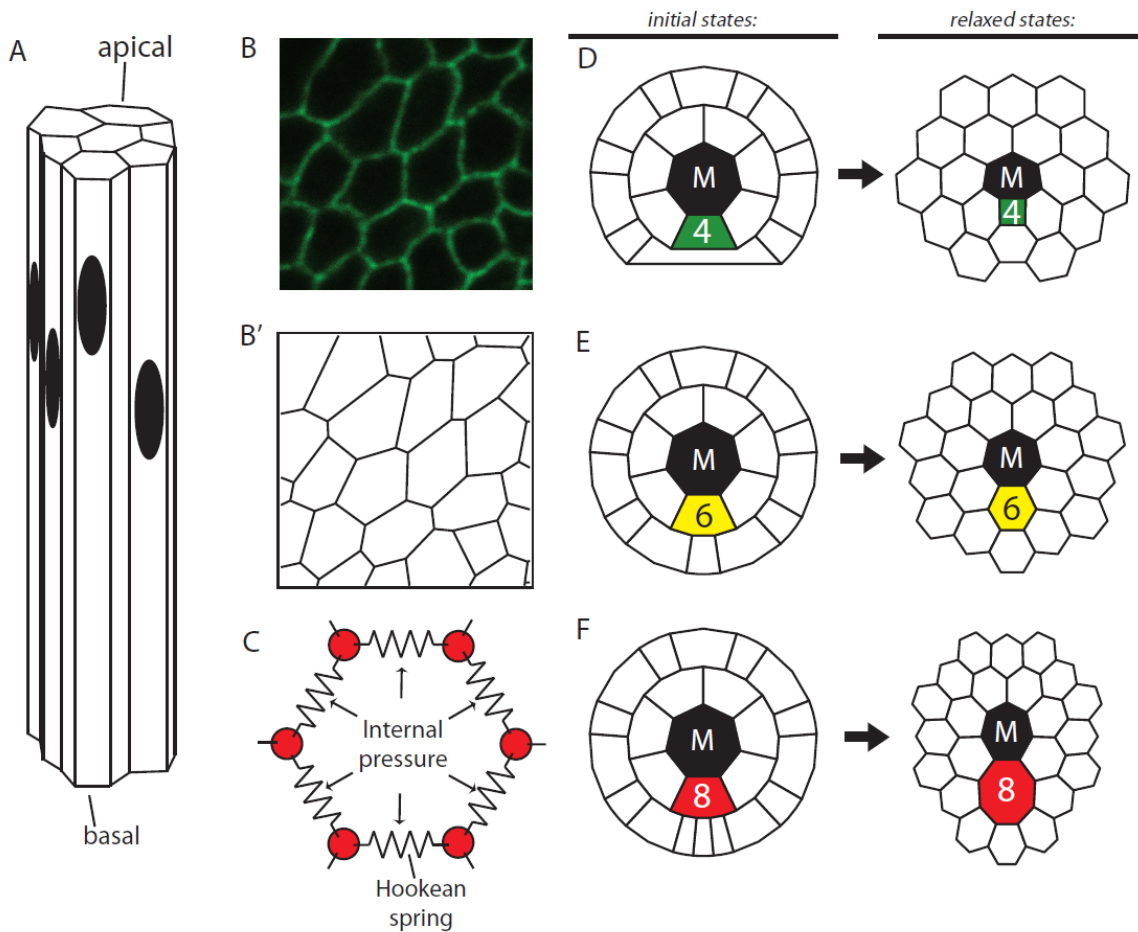


**Figure 2.1: Local epithelial topology is predicted to influence the geometry of an epithelial cell.**

**(A)** A stereotypical simple columnar epithelium. Black spots represent nuclei. **(B)** The *Drosophila* wing disc epithelium, with *nrg*-GFP (green) marking the septate junctions. **(B')** A planar network representation of (B). **(C)** A model for finding the minimum energy configuration of cell packing, based on internal pressure and ideal springs. **(D-F)** (*Initial states, left*) Initial conditions for the relaxation algorithm. Each case varies the topology of the marked cell. (*Relaxed states, right*) At equilibrium, cell shape is specified by a balance between pressure and tension. The central cell's shape is strongly influenced by the labeled cell's topology. See also Figure 2.S1.

mechanism in plants and animals for the control of tissue-level architecture by packing-mediated control of the mitotic cleavage plane.

## RESULTS

### The shape of a cell is predicted to be influenced by local topology

In epithelia, the tissue-level architecture at the apical junctions is a contiguous tiling of polygonal cell shapes (Figures 2.1A and B). This pattern can be described as a simple planar network wherein a cell's number of neighbors (topology) is equivalent to its polygon class (Figure 2.1B'). To investigate the effect of polygonal cell packing on mitotic cell shape, and by extension, cleavage plane orientation, we tested whether a cell's long axis is systematically influenced by the polygon class of neighboring cells.

To address this, we numerically solved for the minimal energy configuration of a local cellular neighborhood (Prusinkiewicz and Lindenmayer, 1990), defined to be a central mitotic cell ( $M$ ) and its first-order polygonal neighbors. Geometrically, cells were idealized as polygonal prisms with constant height (Figure 2.1A). For relaxation, cell mechanics were modeled in terms a balance between edge-length tensions, described using ideal springs, and internal pressure, modeled as an ideal gas (Figure 2.1C). The central mitotic cell,  $M$ , was a heptagon, consistent with the fact that the average mitotic cell is seven-sided *in vivo* (Aegerter-Wilmsen et al., 2010; Gibson et al., 2006). Parameters were chosen to be uniform for every cell, and initial conditions were arbitrary (Figures 2.1D-F). Given these choices, the effect of local topology on the shape of the central cell was an emergent property of the relaxed mechanical network at equilibrium (Figures 2.1D-F; Figure 2.S1; Extended Experimental Procedures).

To analyze the impact of local topology on the long axis of  $M$ , we replaced one neighbor hexagon with a single  $N$ -sided cell,  $N$ . Strikingly, inserting any non-hexagonal neighbor induced a clear long axis in  $M$ , with opposite orientation of the long axis for  $N < 6$  versus  $N > 6$  (Figures 2.1D-F; 2.2A). Specifically, the presence of quadrilateral or pentagonal neighbors induced a long axis parallel to the  $NM$  interface, while heptagons and octagons induced a long axis orthogonal to interface  $NM$ . These results suggest that in cell sheets, the orientation of a mitotic cell's longest axis can be strongly influenced by the polygon class of a single neighboring cell. As a consequence of this effect, neighbor cells with fewer sides (such as quadrilaterals and pentagons) tend to lie along the shortest axis of  $M$ , which is the location of the presumed cleavage plane.

To test whether this effect was robust under more realistic conditions, we numerically relaxed heterogeneous local neighborhoods that were stochastically generated from the known polygonal cell shape distribution of the *Drosophila melanogaster* wing epithelium (Figure 2.2B) (Aegerter-Wilmsen et al., 2010; Gibson et al., 2006). Even under these conditions, more than 70% of quadrilateral neighbors were positioned on the central cell's short axis, double

Figure 2.2:

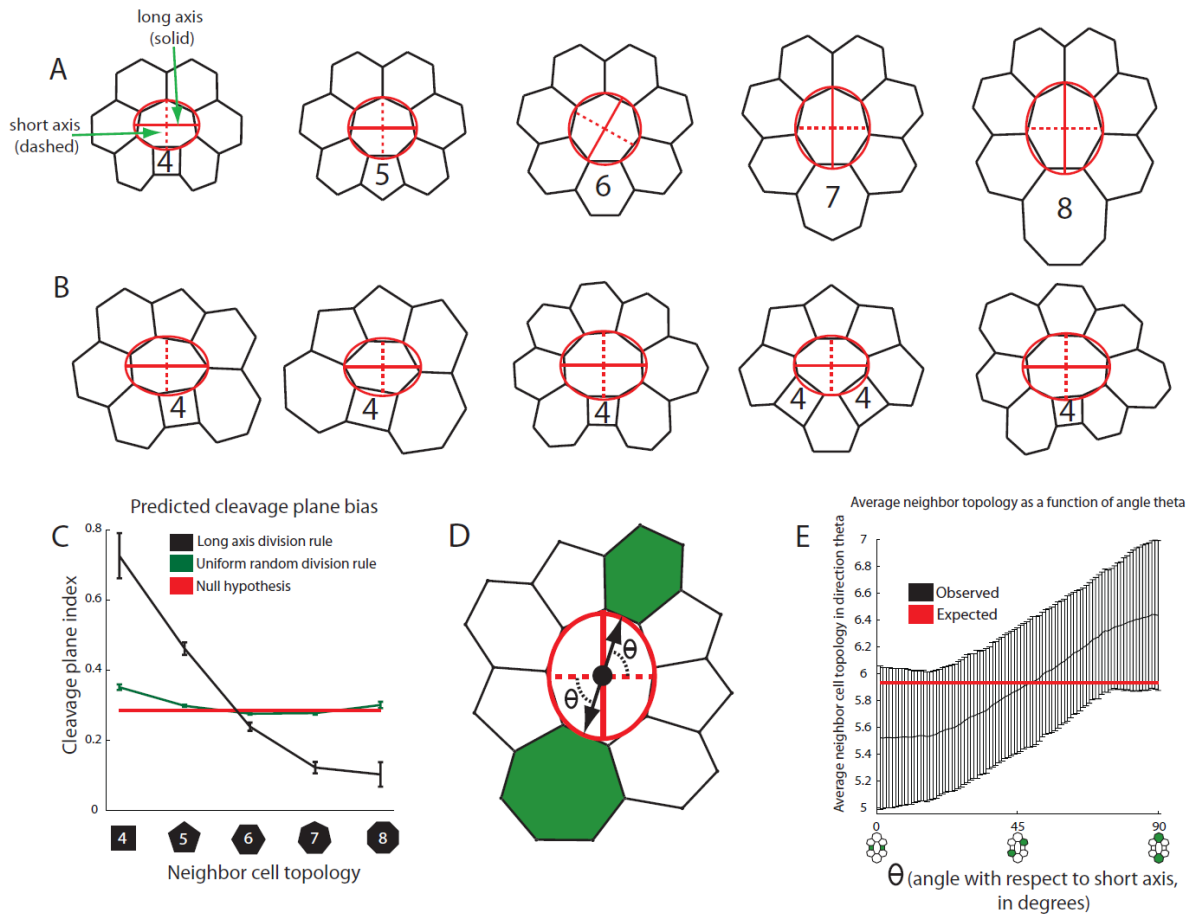


**Figure 2.2: The orientation of a cell's short axis is predicted to correlate with its quadrilateral and pentagonal neighbors, and to anti-correlate with heptagonal and octagonal neighbors.**

**(A)** Neighbor cell topology,  $N$ , influences the direction of the cellular long axis (*solid line*) and short axis (*dashed line*), based on an ellipse of best-fit (*red*). Second order and higher neighbors, which are uniformly hexagonal, are not shown. For  $N < 6$ , the short axis is oriented towards  $N$ -sided cell  $N$ ; for  $N > 6$ , it is oriented perpendicular to  $N$ . **(B)** The attraction of the short axis to quadrilateral cells ( $N=4$ ) is robust to heterogeneity in the local cell neighborhood. **(C)** We computed the cleavage plane index, or fraction of neighbors in each polygon class (*black line*) located adjacent to the central cell's short axis (presumed cleavage plane). Neighbor cells having  $N < 6$  are significantly enriched in this position. Conversely, neighbors having  $N > 6$  are under-represented. For comparison, for a randomly oriented division plane, all  $N$  values occur with similar frequency (*green*), which is close to the null hypothesis of  $2/7$  (*red*). **(D)**

We defined an acute angle,  $\theta$ , with respect to a cell's short axis (*dashed red line*), as well as the neighbor topology in direction  $\theta$  (*green cells*). **(E)** On average, neighbor topology (*black*) is an increasing function of acute angle  $\theta$ . Error bars represent the standard deviation in the sample mean topology in direction  $\theta$  per cell (an average of the 4 positions on the cell cortex corresponding to the  $\theta$ , over 420 such cells).

the percentage expected by chance (Figure 2.2C). To quantify this relationship, we defined an acute angle,  $\theta$ , with respect to the presumed cleavage plane along the central cell's short axis (see Figure 2.2D). On average, as a function of increasing  $\theta$ , the neighbor polygon class in direction  $\theta$  increased monotonically (Figure 2.2E). Therefore, even in a heterogeneous context, the topology of a cellular neighborhood robustly and systematically influenced the orientation of the long axis in a central cell.

### **Cleavage plane bias in the *Drosophila* wing disc**

In both plants and animals, cells are thought to divide their long axis by forming a cleavage plane along the short axis of the cell (Hofmeister, 1863; Strauss et al., 2006). If a cell's short axis consistently bisects its cellular neighbors having the fewest sides (Figure 2.2), then mitotic division planes should be disproportionately biased towards quadrilaterals and pentagons *in vivo*. To test this, we measured the correlation between neighbor cell polygon class and cleavage plane orientation in the *Drosophila* wing imaginal disc (Figure 2.3A). Here, cell division proceeds through a stereotyped process of cell rounding at the apical epithelial surface (Figures 2.3B-D;(Gibson et al., 2006)). To define the frequency with which different classes of polygonal neighbors were bisected by the cleavage plane, we examined 420 cells at the cytokinetic stage, which is the most stable and easily scored phase of mitosis (Figure 2.3E). For each case, we recorded the position of all primary neighboring polygons and computed the frequency with which each polygon class occupied the cleavage plane position (Figures 2.3F,G).

If the orientation of cell division were random with respect to local topology, approximately 28.6% of any given polygon class would be expected to correlate with the cleavage plane (two randomly-chosen cells out of seven neighbors). However, in the wing disc, we found that more than 50% of quadrilaterals in the primary neighborhood occupied the division plane position (Figure 2.3H;  $n=46/83$ ). Further, octagons were anti-correlated with the division plane, and occupied that position with less than 10% probability ( $n=6/77$ ). As predicted by the mechanical model, this cleavage plane bias was monotone decreasing across all polygon types. We conclude that in the *Drosophila* wing disc, the polygonal topology of local neighborhoods strongly influences cleavage plane orientation in mitotic cells.

In order to test the assumption that *Drosophila* wing disc cells actually divide their longest axis, we next performed time-lapse analysis of proliferating *Drosophila* wing discs in *ex vivo* culture (see Movie S1; Experimental Procedures). For each of 198 mitotic cells (Figure 2.4A), we measured the geometric long axis orientation during both interphase (Figure 2.4A', far left), and cytokinesis (Figure 2.4A', far right). We found a strong tendency for cells to follow a long-axis division mechanism, although with moderate noise in the orientation (Figure 2.4B). This tendency to divide the longest axis correlated with the interphase geometry (Figure 2.4B), and increased with the cell's interphase

Figure 2.3:

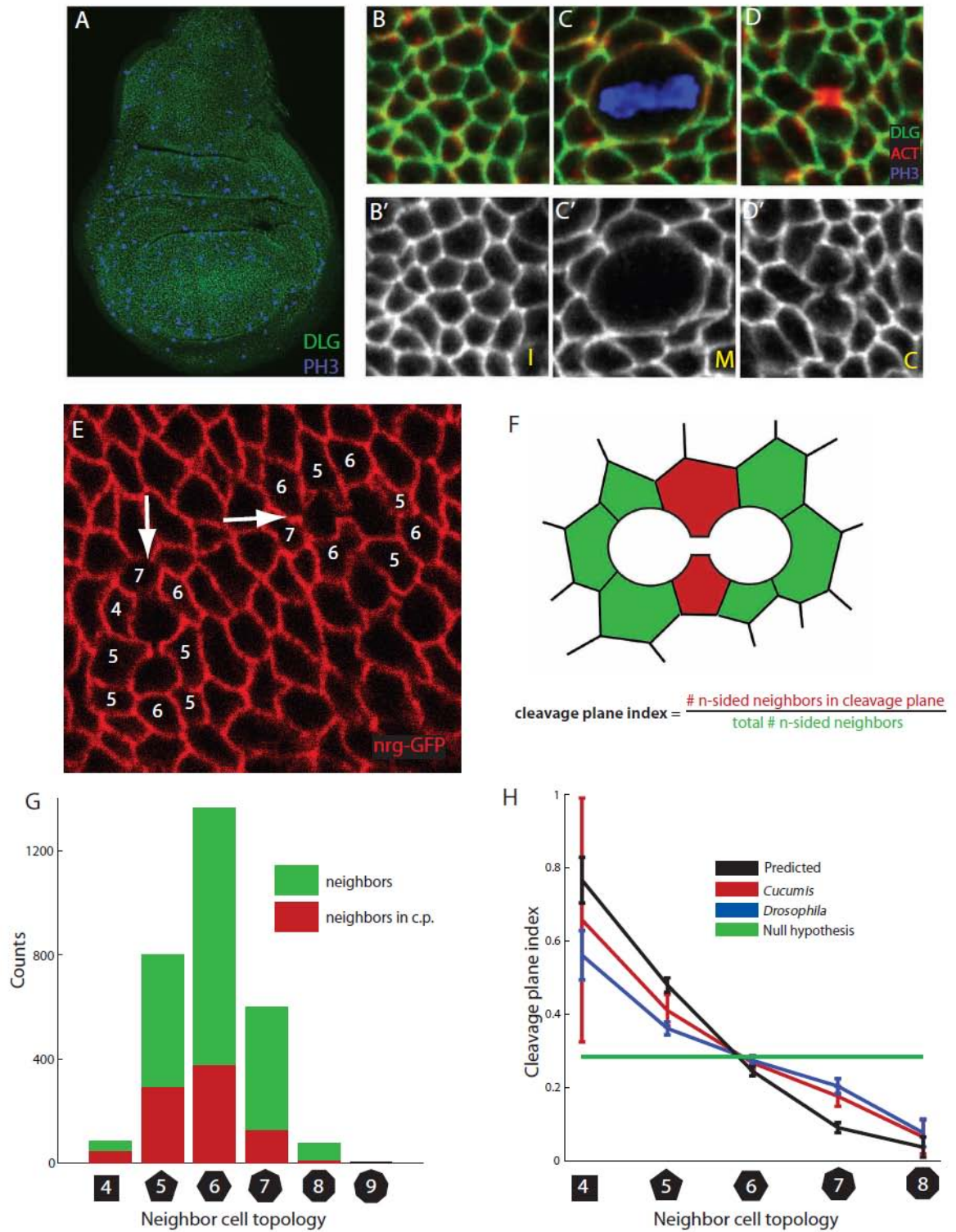


**Figure 2.3: In both plants and animals, a dividing cell's cleavage plane correlates with its quadrilateral and pentagonal neighbors, and anti-correlates with heptagonal and octagonal neighbors.**

**(A)** The *Drosophila* wing imaginal disc, stained with anti-DLG to mark the junctions (*green*) and anti-PH3 to mark chromatin (*blue*). **(B-D; B'-D')**, Cell division proceeds in the plane of the epithelium via a stereotyped division process including interphase (I), mitosis (M), and cytokinesis (C). Actin staining is shown in red. **(E)** We can infer the topological complement of neighbors, as well as the division orientation of dividing cells, from cytokinetic figures. Junctions are marked by a *nrg*-GFP protein trap (*red*). **(F-G)** We examined > 400 such figures, and sorted the neighbors by polygon class. The neighbors on the division plane (*red*) are a subset of the full complement of neighbors (*green and red*). **(H)** An overlay of the predicted mitotic cleavage plane bias based on our mechanical model (*black*), with the biases computed from both *Drosophila* wing disc epithelium (*blue*) and cucumber epidermis (*red*). Each is compared with the topological null hypothesis (*green*). See also Figure 2.S2 for further information.

elongation ratio (the ratio of the long axis to the short axis; Extended Experimental Procedures). For example, for the 99 cells having an elongation ratio below the median value of 1.68, the average deviation from a long axis-division mechanism was about 33°; by contrast, for the 99 cells having an elongation ratio above the median value, the average deviation was about 21° (data not shown). This dependence on the relative axis lengths suggests that these cells might be able to adjust their spindle orientations to their newly acquired shapes following mechanical strain, as has been previously reported in cell culture and in vertebrate embryonic cells (Black and Vincent, 1988; Gray et al., 2004; O'Connell and Wang, 2000; Strauss et al., 2006).

To test whether deviation from the long axis division mechanism could explain the discrepancy between our cleavage plane bias predictions and the empirical measurements, we incorporated the measured deviation into our original model (Figure 2.4C; Extended Experimental Procedures). Interestingly, when the measured deviation was incorporated, the mechanical predictions were significantly improved (compare the red and black curves in Figure 2.4C), closely matching the empirically measured bias (Figure 2.4C, blue curve). Therefore, cleavage plane bias is likely to be robust to noise in the cleavage plane mechanism, and may be present even when cell divisions do not perfectly obey a long axis division scheme.

### **Cleavage plane bias in plant epidermis**

Because our original predictions were mechanically motivated (Figures 2.1 and 2.2), and are expected to persist even when there is moderate noise in the cleavage plane (Figure 2.4), we reasoned that cleavage plane bias should be equally likely to appear in plant tissues. To test this, we used data from FT Lewis's classical study of cucumber epidermal cell topology (*Cucumis sativus*) to compute the probability with which an N-sided polygonal cell occupies the division plane of a mitotic neighbor (Extended Experimental Procedures; Lewis, 1928). Remarkably, in *Cucumis*, the cleavage plane bias was almost indistinguishable from that measured in the *Drosophila* wing disc (Figure 2.3H). We once again observed strong enrichment for 4-sided cells along the cleavage planes of mitotic cells, while 8-sided cells were underrepresented. In order to verify our inferences from Lewis's data (1928), we also directly examined the relationship between local topology and cellular long axis orientation in the epidermis of *Cucumis* (Figure 2.S3A). From fixed samples of cucumber epidermis, we studied a population of 501 epidermal cells having the same polygonal distribution as the original population of 500 mitotic cells studied by Lewis (1928). Cells were selected in a spatially constrained, impartial manner based solely on polygon class (Extended Experimental Procedures). We next tested whether a naïve long-axis division rule was sufficient to generate cleavage plane bias in *Cucumis*. Based on an ellipse of best fit to each cell's geometry (Figure 2.S3A; Extended Experimental Procedures), we were able to reproduce not only the cleavage plane enrichment observed in Lewis's original data (Figure 2.S3C), but also the inferred cleavage plane bias (Figure 2.S3D). Taken

Figure 2.4:

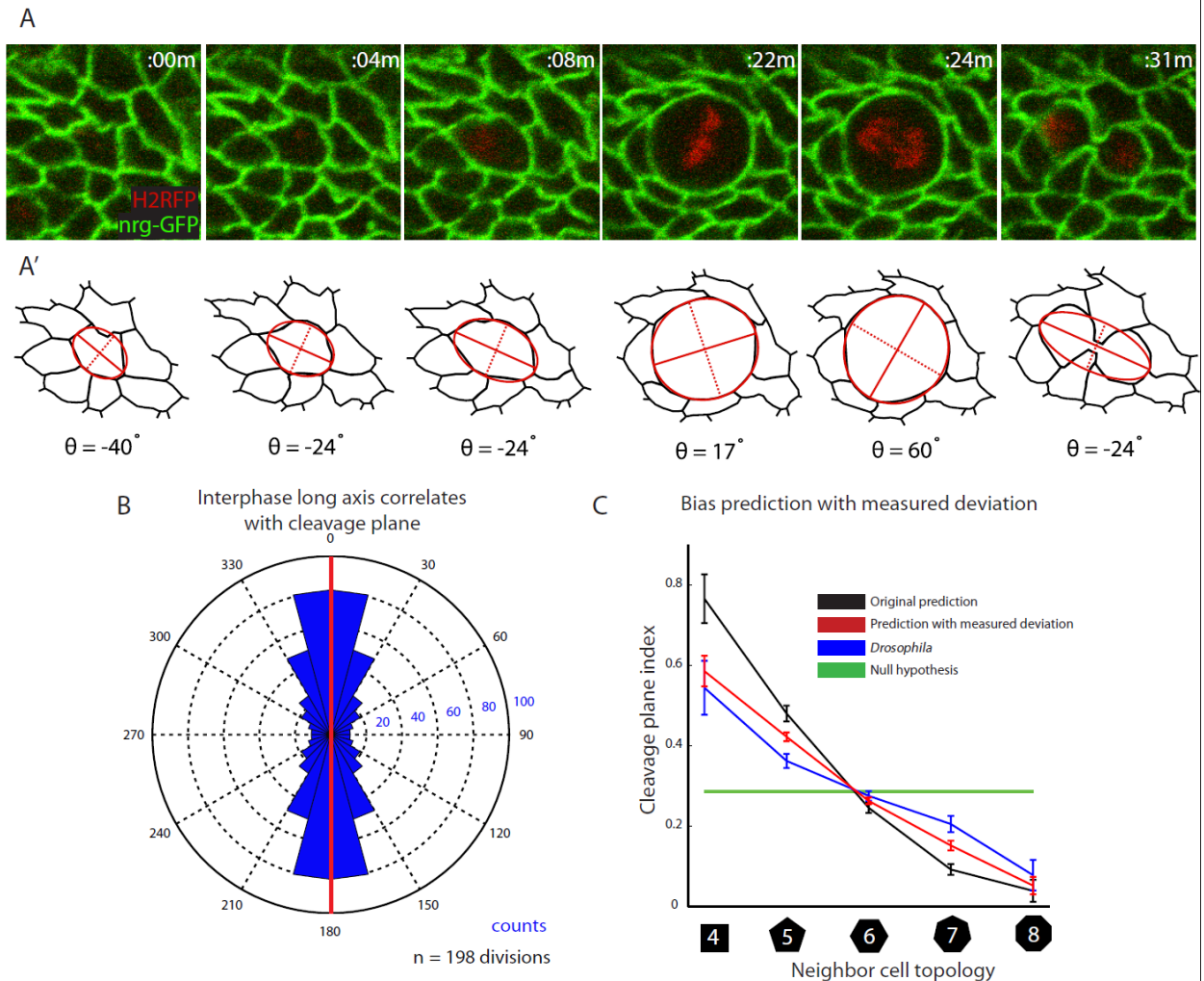


**Figure 2.4: *Drosophila* wing disc cells approximately obey a long-axis division rule.**

**(A)** Time series analysis illustrates the process in which an interphase cell entering mitosis gradually dilates before reaching full rounding, and then subsequently undergoes cytokinesis, in an orientation approximately predicted by its interphase long axis. **(A')** Drawings of the process described in the corresponding panels in A, including the mitotic cell and its immediate neighbors. The long axis of the ellipse of best fit (red) is labeled with a solid line, whereas the dashed line (predicted cleavage plane) represents the short axis. **(B)** The eventual orientation of the cleavage plane can be predicted based on the interphase long axis orientation. The red line (zero deviation from long-axis division) represents a perfect correlation between the interphase long axis and the long axis of the resulting cytokinetic figure. Blue bars show the number of cells (represented by radial distance from the center) that divided with a

particular angular deviation from the interphase long axis. On average, the deviation was approximately 27.1 degrees. The data is represented by the first quadrant (0° to 90°), which is also displayed symmetrically in the other three quadrants (90° to 360°). **(C)** The bias curve prediction that incorporates the measured deviation of 27 degrees from the long axis (*red*) is significantly closer to the empirically measured cleavage plane bias (*blue*) than the naïve long-axis prediction is (*black*). A Gaussian noise model with 27 degree standard deviation gives a similar result (data not shown). We controlled for the influence of topological relationships by using the same local neighborhoods as were measured from the empirical data (*blue*). See also the Extended Experimental Procedures and Figure 2.S3, which suggests a long axis mechanism may also operate in *Cucumis*.

together, our results suggest that cleavage plane bias occurs in polygonal cell sheets as an emergent effect of cell packing, independent of species-specific considerations.

### Cleavage plane bias and the topological constraints on cell geometry

The quantitative similarity of cleavage plane bias in plants, animals, and *in silico* suggests the underlying mechanism is geometric, rather than molecular. In fact, fundamental geometric constraints imposed by the internal angles of neighboring polygons are sufficient to explain this phenomenon. For illustration, consider the comparison between a tiling of three hexagons versus two hexagons and a square (Figures 2.5A and B). From elementary geometry, a square (N=4) has internal angles of 90°, while the internal angles of a hexagon (N=6) average 120° (for an N-sided polygon, average internal angles are 180°(N-2)/N). In the context of a contiguous layer, the presence of 90° internal angles within the square forces the internal angles of the adjacent hexagon to increase to 135° (Figure 2.5B). Intuitively, this deformation results in elongation of these hexagons parallel to the interface with the square, thus generating a cellular long axis.

The constraints imposed by the internal angles of one cell upon the long axis of its neighbor can be formalized for the arbitrary case of an N-sided cell, surrounded by N symmetric hexagonal neighbors (Figure 2.5C). Assume that a mitotic cell, *M*, is situated vertically above cell *N*, resulting in a horizontal interface *NM* of length *L*. In the simplest case, all side lengths, including *L*, are equal, and without loss of generality can be set to one. Further, the internal angles  $\alpha_N$  and  $\beta_M$  can be computed as a function of *N*. Using simple trigonometry and exploiting the symmetric configuration of neighbors, we can solve for the ratio of the horizontal axis,  $d_m$ , to the vertical axis,  $h_m$ , for the ellipse of best fit to cell *M* (Figure 2.5C; Extended Experimental Procedures):

$$\frac{d_m}{h_m} \approx \sec\left(\frac{\pi}{N}\right) \sqrt{\sin\left(\frac{\pi}{N}\right) \left(1 + \sin\left(\frac{\pi}{N}\right)\right)} \quad (2.1)$$

In this framework, the direction of *M*'s short axis (presumed cleavage plane) is described by the ratio  $d_m:h_m$ , which the above equation shows is determined by the *N* value (Figure 2.5D). Geometrically, the ratio  $d_m:h_m$  varies with *N* because the length  $d_m$  decreases for *N*>6 and increases for *N*<6 (Figure 2.5E). Consequently, when *N*>6 ( $d_m:h_m < 1$ ),  $d_m$  forms the short axis parallel to interface *NM*. Conversely, if *N*<6 ( $d_m:h_m > 1$ ), then  $h_m$  forms the short axis, or presumed cleavage plane, in the direction of *N*, perpendicular to the interface *NM*.

Figure 2.5:

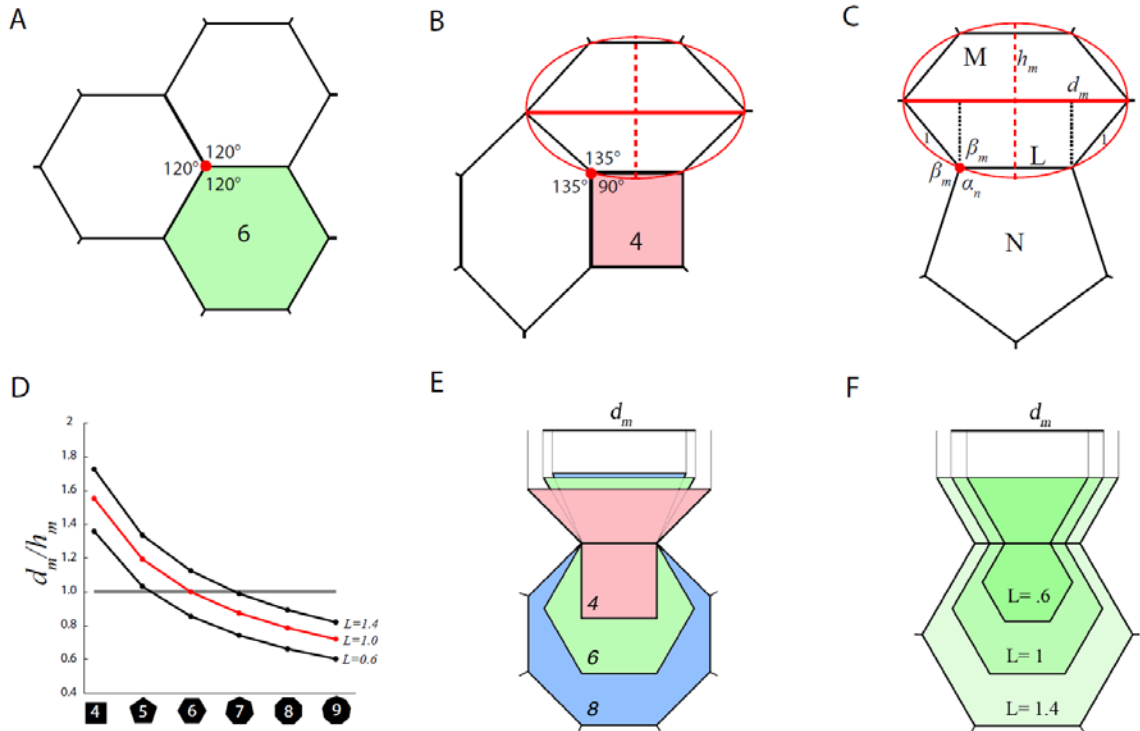


**Figure 2.5: Fundamental packing constraints are sufficient to explain cleavage plane bias.**

**(A)** Hexagons pack at 120-degree angles. **(B)** A 4-sided cell distorts the internal angles of the surrounding hexagons, inducing a long axis. **(C)** A geometrical argument for division plane bias. The N-sided neighbor cell influences the ratio of the horizontal axis,  $d_m$  to the vertical axis,  $h_m$ , in the M-cell. When  $d_m:h_m > 1$ , the N cell is in the predicted cleavage plane position for the M-cell. **(D)** A plot of the ratio  $d_m:h_m$ , for different values of N and L. Above the gray line, the N-cell is in the M-cell's predicted division plane; the opposite is true below the gray line. **(E-F)** Both N and L influence the direction of the long axis in the M cell. **(E)** The value of N influences the direction of the long axis in the M cell (top cell), for constant L. **(F)** The long axis of the M-cell is influenced by the side length, L, for a constant N-value. See also Figure 2.S4.

## Cleavage plane bias is predicted to be robust to side length and cell size differences

Intuitively, differential side lengths of N-sided neighbors would also affect the short axis orientation of  $M$  (Figure 2.5F). To analyze the relative contributions of angular constraints versus side lengths, consider the more realistic case when the edge lengths are non-uniform ( $L \neq 1$ ). Here,  $d_m:h_m$  depends on both  $N$  and  $L$  (Figure 2.5D and Extended Experimental Procedures):

$$\frac{d_m}{h_m} \approx \sec\left(\frac{\pi}{N}\right) \sqrt{\sin\left(\frac{\pi}{N}\right) \left(L + \sin\left(\frac{\pi}{N}\right)\right)} \quad (2.2)$$

For the simplified case when  $L=1$ , the direction of the short axis undergoes a  $90^\circ$  rotation (between horizontal and vertical) when  $d_m:h_m$  passes through the value 1, which corresponds to  $N=6$  (*red line*, Figure 2.5D). Changing the value of  $L$  changes the length  $d_m$  (Figure 2.5F), and thus alters the  $N$  value at which this transition occurs (*black lines*, Figure 2.5D). The long axis orientation of  $M$  is thus determined by the interplay between the polygon class and apposed side length of each neighbor,  $N$ . In the *Drosophila* wing disc, the value of  $L$  fluctuates by about 40% on average (Table 2.1). Equation (2.2) predicts that a 40% deviation in  $L$  value would change the point of rotation by only a single  $N$  value, suggesting that cleavage plane bias should be noisy yet reproducible.

Supporting this analysis, cell size has a surprisingly weak influence compared to polygon class in our mechanical simulations (Figure 2.S4). Consistent with our simulations, based on live imaging analysis of local neighborhoods surrounding dividing cells in the *Drosophila* wing disc epithelium, there was no discernable difference in average area for cells occupying the cleavage plane position (Figure 2.S4D). We conclude that internal angle constraints linked to the polygon class of neighboring cells are likely the dominant cause of cleavage plane bias, with a lesser contribution from the effects of differential side lengths.

## Cleavage plane bias is predicted to alter global tissue topology

Numerous recent studies have used mathematical or computational approaches to understand the equilibrium topology of proliferating epithelia (Aegerter-Wilmsen et al., 2010; Cowan and Morris, 1988; Dubertret et al., 1998; Dubertret and Rivier, 1997; Gibson et al., 2006; Korn and Spalding, 1973; Miri and Rivier, 2006; Patel et al., 2009). Intuitively, cleavage plane bias must alter the topology of a cell sheet because it modulates the rates at which specific polygon classes gain sides due to neighbor cell mitoses. We therefore investigated the implications of cleavage plane bias for the distribution of polygonal cell shapes. We used two distinct computational simulations informed by the empirical division parameters (Figure 2.S2A-C) to model global topology with and without cleavage plane bias (Figures 2.6 and 2.S5-2.S6). For both simulation types, the cleavage plane bias values approximated those measured

Figure 2.6:

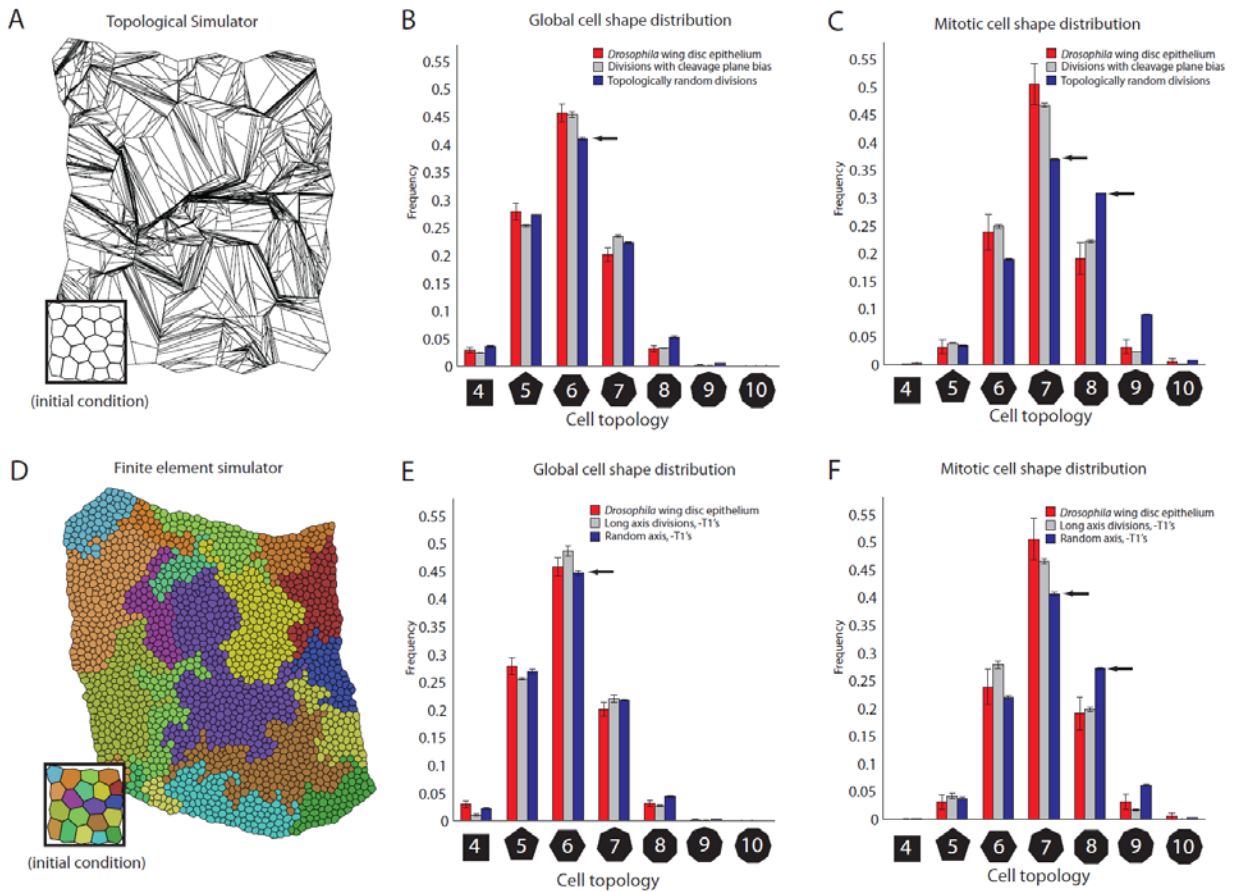


**Figure 2.6: Cleavage plane bias participates in cell shape emergence, and is required for wild-type cell packing.**

**(A)** The topological simulator does not model cellular mechanics, but does explicitly keep track of topological neighbor relationships. Based on topological weights, division likelihood, division symmetry, and cleavage plane bias are matched to empirically measured statistics in a Monte-Carlo framework (see Figures 2.S2A-C). **(B)** Hexagonal frequency declines by approximately 4% in the absence of bias. Arrows highlight this difference. **(C)** The distribution of mitotic cells shows pronounced alterations in the absence of bias. Arrows highlight the differences. **(D)** The finite element simulator models cellular mechanics, division, and rearrangement. The simulator captures mechanics in terms of a net, interfacial tension, which is modeled using rod-like finite elements. Division likelihoods are informed by the empirically measured values Figure 2.S2A). Cleavage plane bias approximates the empirical values, and is achieved using long-axis divisions. For finite element simulations incorporating cellular rearrangements (T1 transitions), see Figure 2.S6. **(E)** In the absence of bias,

hexagonal frequency declines by about 4% (compare with panel B). **(F)** The distribution of mitotic cells again shows pronounced alterations (compare with panel C). See also Figures 2.S5-2.S6.

empirically (Figures 2.S5F and 2.S6H). Both an abstract, topological simulator using a Monte-Carlo framework based on topological weights (Figure 2.6A) (Patel et al., 2009) and a mechanical model of tissue growth based on long-axis divisions (Figure 2.6D) (Brodland and Veldhuis, 2002) confirmed that cleavage plane bias affects the frequency of hexagonal cells (Figures 2.6B,E). Moreover, the distribution of mitotic polygonal cells was severely disrupted in the absence of bias, resulting in decreased frequencies of heptagons and increased frequencies of octagons and nonagons (Figures 2.6C,F). Taken together, these results suggest that cleavage plane bias is required to achieve the normal equilibrium distribution of cell shapes.

## DISCUSSION

The results presented here raise several important questions. First, while our analysis provides a geometrical rationale for cleavage plane bias based on interphase polygon topology (Figure 2.5), we still cannot rule out the simultaneous action of molecular cues at the cell cortex. In metazoans, epithelial cells often undergo mitosis-induced deformation prior to cleavage (Figures 2.3C,C'; Figures 2.4A,A') (Gibson et al., 2006; They and Bornens, 2008), and our live imaging results from *Drosophila* strongly suggest that a cellular long axis present in interphase can inform spindle orientation during mitosis (Figure 2.4). One intriguing possibility is that the interphase distribution of cell-cell contacts determines the localization of cortical cues important for spindle alignment, as has been previously reported (They et al., 2007; They et al., 2005).

For plant cells, by contrast, our results indicate that local cell packing influences, either directly or indirectly, the placement of the phragmosome and/or pre-prophase band (Pickett-Heaps and Northcote, 1966; Sinnott and Bloch, 1940). There are multiple ways in which this might be accomplished, potentially including stress or strain sensing mechanisms (Hamant et al., 2008; Lintilhac and Vesecky, 1984; Lynch and Lintilhac, 1997), or more simply, based on cytoskeletal mechanisms that are able to sense cell shape (Flanders et al., 1990; Goodbody et al., 1991; Katsuta et al., 1990). To conclude, in addition to our purely geometrical interpretation, our results are also consistent with a hypothesis that in both animals and in plants, local epithelial topology may coordinately specify both the cellular long axis and the distribution of cortical determinants of the eventual cleavage plane.

A second important question concerns the broader implications of cleavage plane bias for the emergence of cell shape. Previous studies of proliferating cell sheets in *Drosophila* and in *Cucumis* have shown that the distribution of mitotic cell shapes is shifted to have a heptagonal mean, as opposed to the hexagonal mean observed in the population of cells overall (Aegerter-Wilmsen et al., 2010; Gibson et al., 2006; Lewis, 1928). Our simulations (Figures 2.6A,D) suggest that the mitotic cell distribution is disrupted in the absence of cleavage plane bias (Figures 2.6C,F), which is consistent with the view that in both *Drosophila* and *Cucumis*, interphase cells passively gain additional sides as a consequence of neighbor cell divisions. This interpretation contrasts with the idea that the mitotic

shift reflects modulation of the cell cycle by topology-dependent mechanical stress (Aegerter-Wilmsen et al., 2010). Moreover, cleavage plane bias is actually expected to synergize with the mitotic shift. By enriching for super-hexagonal cells in the mitotic cell population, which are entropically favored to neighbor sub-hexagonal cells (Peshkin et al., 1991), the mitotic shift intuitively must amplify the effects of cleavage plane bias.

In summary, by varying the orientation of cell division based on neighbor cell geometry, cells and tissues are able to achieve increased geometric regularity via a dynamic, topology-mediated feedback and control system. Precisely how the default geometric forces that bias cleavage plane orientation interact with other mechanisms of division plane control (Baena-Lopez et al., 2005; Gong et al., 2004; Li et al., 2009; Segalen et al., 2010; Siller et al., 2006; Willemsen et al., 2008) should be an important avenue for future research.

**Table 2.1:** *The effective L value changes by approximately 40% in wild type Drosophila tissues.*

N-cell polygon class	Average effective L Value	Standard deviation in effective L Value	Sample size (hexagonal interfaces with N-cells)
4	1.2504	.4165	22 interfaces
5	1.1158	.4141	231 interfaces
6	1.0580	.4053	487 interfaces
7	.9237	.4081	341 interfaces
8	.9620	.5405	46 interfaces

**Table 2.1 legend:** For each value of N (column 1), the average effective L value has been computed (column 2), as well as the sample standard deviation (column 3), using empirically extracted cellular networks from the *Drosophila* wing imaginal disc (Extended Experimental Procedures). The sample size for each calculation is given in column 4. The effective L value, computed for hexagonal cells, is the average value of an edge shared with an N-sided neighbor, divided by the average length of the remaining 5 edges.

## Experimental Procedures:

**Fly strains:** To visualize the septate junctions, we used a *neuroglian-GFP* exon trap line, which was described in a previous study (Morin et al., 2001). To visualize the chromosomes in parallel, we generated a stock also carrying a Histone-2 RFP marker ((Schuh et al., 2007); Bloomington stock 23650).

**Wing disc sample preparation & imaging:** Wing discs were dissected from wandering 3<sup>rd</sup> instar larvae in Ringers' solution, fixed in 4% paraformaldehyde in PBS, and then mounted in 70% glycerol/PBS. For live imaging, discs were carefully dissected and placed in a 50:50 mixture of Ringer's solution (130mM NaCl, 5 mM KCl, 1.5 mM MgCl<sub>2</sub>), and a second solution (Aldaz et al., 2010), consisting of 2% FBS (Gibco) and 0.5% Pen/Strep (Gibco; 5,000 units/mL penicillin; 5,000 µg/mL streptomycin) in Shields and Sang M3 Insect media (Sigma). Live discs were mounted between two pieces Scotch double-sided tape (3M). Air bubbles were added to the medium using an insulin syringe (BD Ultra-fine with a 30-gauge needle) to potentiate gas exchange. Wing discs were maintained in culture for up to four hours, and imaged at intervals of 15-30 seconds. All samples, live and fixed, were imaged on a Leica SP5 or Leica SP2 confocal microscope with a 63X glycerol or oil objective.

**Cucumis sample preparation and imaging:** Epidermis was collected from freshly gathered cucumbers approximately 10 cm in length and 2 cm in diameter (Red Ridge Farm, Odessa, MO). Epidermis was peeled in thin layers and fixed in 4% paraformaldehyde in 50 mM KPO<sub>4</sub>, 5.0 mM EDTA and 0.2% Tween20 (pH 7) for at least 2 hours at room temperature (adapted from Gallagher and Smith (1999)). Tissue pieces were then washed 2-5 times in dH<sub>2</sub>O, and incubated in 5 mg/mL Calcofluor White (Sigma) in PBS for at least 10 minutes before imaging. Images were collected using a Zeiss LSM 510 Meta with a 20x Plan-Apochromat objective, NA 0.8.

**Error bars:** Unless otherwise specified, error bars refer to a single standard deviation. For the case of ratio distributions, we have reported an average value of the standard deviation. This was computed as follows: the data were randomized and broken into three sub-samples of equal size in order to compute an average value for the standard deviation, based on 1000 random shuffles of the data.

**Annotation of *Drosophila* wing disc cytokinetic figures in fixed preparations:** A total of 420 cytokinetic figures and their 2946 cellular neighbors were scored by hand, in multiple focal planes to ensure accuracy of topological counts. Out of the 2946 neighbors, 840, or exactly two per cytokinetic figure, were designated as being in the division plane position. Cells were interpreted to be in the division plane position when they occupied the majority of the cytokinetic furrow. Due to the ambiguity of division ordering, cytokinetic figures adjacent to other cytokinetic figures were not considered for analysis.

**Annotation of fixed *Drosophila* wing disc epithelial cell sheets:** Images of contiguous epithelial regions from *Drosophila* wing disc epithelia were annotated by hand using Microsoft Powerpoint. We used custom-built software to digitize the annotations for analysis in MATLAB. A total of three such cell sheets, containing 254, 195, and 233 cells, respectively, were analyzed to compute the effective L value (table 2.1), which is described in the text (Figure 2.4C). See Extended Experimental Procedures for additional details.

**Live imaging analysis of mitosis in the *Drosophila* wing disc:** From live movies, a total of 198 mitotic cells in the *Drosophila* wing disc epithelium were analyzed by hand using ImageJ. With the exception of cells located on compartment boundaries, every scoreable cell on the epithelium was used. To control for possible mechanical influences due to neighboring divisions, we did not consider dividing cells neighboring each other to be scoreable if they rounded up at the same time. Interphase geometry measurements were based on the earliest available time point (the first movie frame), except in rare cases when epithelial morphology obscured the cell in question, in which case a slightly later time point was used. The long axis orientation of each cell was computed using imageJ, including curvature, based on manual input from the Polygon Selections tool. The identical procedure was used for each cell at later stages, including the eventual cytokinetic figure (see Figure 2.4A' for an illustration). See the Extended Experimental Procedures for additional details.

#### **Analysis of *Cucumis* epidermal cell sheets:**

Images of contiguous regions of *Cucumis* epidermis were annotated by hand using ImageJ. Cell geometry was outlined using the Polygon Selections tool, with one node placed per tri-cellular junction, except in cases of very curved cellular edges, in which additional nodes were used to increase annotation accuracy. To visualize the ellipse of best fit to cell geometry, we used a custom-made ImageJ macro. See the Extended Experimental Procedures for additional information.

**Algorithm for computing the minimal energy configuration for local cellular neighborhoods:** We used a mechanical relaxation algorithm for cellular networks that has been previously described (Prusinkiewicz and Lindenmayer, 1990). For relaxation (Figure 2.1), cellular networks were modeled in terms of a balance between edge length tensions (described using ideal springs) and internal pressure (Figure 2.S1). Relaxation was implemented in terms of a system of ordinary differential equations that were solved numerically using the ODE45 solver in MATLAB (Mathworks). See the Extended Experimental Procedures for additional information.

**Topological simulations of proliferation:** Proliferation was simulated in terms of a network containing exclusively tri-cellular nodes, with wrapping boundary conditions. All division parameters, including division likelihoods of polygonal cells, the statistical partitioning of mother cell nodes, and the likelihoods of orienting the division plane in the direction of specific polygonal neighbor cell

types, are matched to the empirically measured statistics for the *Drosophila* wing disc (see Figure 2.S2A-C). The algorithmic details are described in the Extended Experimental Procedures.

**Finite element models of proliferating cell sheets:** The FEM simulations (Brodland and Veldhuis, 2002; Chen and Brodland, 2000) model apical contractility, cell-cell adhesion, and all other forces along the cellular edge lengths in terms of a net, interfacial tension,  $\gamma$ , which is generated by rod-like finite elements. Proliferation is modeled in terms of long-axis divisions. Cell-cell rearrangements (T1 transitions) are permitted when cellular edge lengths shrink below a threshold value. See Figure 2.S6 for a comparison between simulations in which T1 transitions are active, versus those for which they are inactive. Additional details are described in the Extended Experimental Procedures.

#### **ACKNOWLEDGEMENTS:**

The authors gratefully acknowledge support for this research from the Stowers Institute for Medical Research and the Burroughs Wellcome Fund (to M.C.G.), from the National Science Foundation (to R.N.), from the Natural Sciences and Engineering Research Council of Canada (to G.W.B) and the Howard Hughes Medical Institute (to N.P.). W.T.G. was supported in part by NIH/NIGMS Molecular Biophysics Training Grant #T32 GM008313 and CTC grant 1029 to MCG.

## Chapter 2 References:

- Aegerter-Wilmsen, T., Smith, A.C., Christen, A.J., Aegerter, C.M., Hafen, E., and Basler, K. (2010). Exploring the effects of mechanical feedback on epithelial topology. *Development* 137, 499-506.
- Aldaz, S., Escudero, L.M., and Freeman, M. (2010). Live imaging of *Drosophila* imaginal disc development. *Proc Natl Acad Sci U S A* 107, 14217-14222.
- Baena-Lopez, L.A., Baonza, A., and Garcia-Bellido, A. (2005). The orientation of cell divisions determines the shape of *Drosophila* organs. *Curr Biol* 15, 1640-1644.
- Black, S.D., and Vincent, J.P. (1988). The first cleavage plane and the embryonic axis are determined by separate mechanisms in *Xenopus laevis*. II. Experimental dissociation by lateral compression of the egg. *Dev Biol* 128, 65-71.
- Brodland, G.W., and Veldhuis, J.H. (2002). Computer simulations of mitosis and interdependencies between mitosis orientation, cell shape and epithelia reshaping. *J Biomech* 35, 673-681.
- Buschmann, H., Chan, J., Sanchez-Pulido, L., Andrade-Navarro, M.A., Doonan, J.H., and Lloyd, C.W. (2006). Microtubule-associated AIR9 recognizes the cortical division site at preprophase and cell-plate insertion. *Curr Biol* 16, 1938-1943.
- Chen, H.H., and Brodland, G.W. (2000). Cell-level finite element studies of viscous cells in planar aggregates. *J Biomech Eng* 122, 394-401.
- Cowan, R., and Morris, V.B. (1988). Division rules for polygonal cells. *J Theor Biol* 131, 33-42.
- Dubertret, B., Aste, T., Ohlenbusch, H.M., and Rivier, N. (1998). Two-dimensional froths and the dynamics of biological tissues. *Physical Review E* 58, 6368-6378
- Dubertret, B., and Rivier, N. (1997). The renewal of the epidermis: a topological mechanism. *Biophys J* 73, 38-44.
- Fernandez-Minan, A., Martin-Bermudo, M.D., and Gonzalez-Reyes, A. (2007). Integrin signaling regulates spindle orientation in *Drosophila* to preserve the follicular-epithelium monolayer. *Curr Biol* 17, 683-688.
- Fischer, E., Legue, E., Doyen, A., Nato, F., Nicolas, J.F., Torres, V., Yaniv, M., and Pontoglio, M. (2006). Defective planar cell polarity in polycystic kidney disease. *Nat Genet* 38, 21-23.
- Flanders, D.J., Rawlins, D.J., Shaw, P.J., and Lloyd, C.W. (1990). Nucleus-associated microtubules help determine the division plane of plant epidermal cells: avoidance of four-way junctions and the role of cell geometry. *J Cell Biol* 110, 1111-1122.
- Gallagher, K., and Smith, L.G. (1999). discordia mutations specifically misorient asymmetric cell divisions during development of the maize leaf epidermis. *Development* 126, 4623-4633.
- Gibson, M.C., Patel, A.B., Nagpal, R., and Perrimon, N. (2006). The emergence of geometric order in proliferating metazoan epithelia. *Nature* 442, 1038-1041.
- Gong, Y., Mo, C., and Fraser, S.E. (2004). Planar cell polarity signalling controls cell division orientation during zebrafish gastrulation. *Nature* 430, 689-693.
- Goodbody, K.C., Venverloo, C.J., and Lloyd, C.W. (1991). Laser Microsurgery Demonstrates That Cytoplasmic Strands Anchoring the Nucleus across the Vacuole of Premitotic Plant-Cells Are under Tension - Implications for Division Plane Alignment. *Development* 113, 931-939.
- Gray, D., Plusa, B., Piotrowska, K., Na, J., Tom, B., Glover, D.M., and Zernicka-Goetz, M. (2004). First cleavage of the mouse embryo responds to change in egg shape at fertilization. *Curr Biol* 14, 397-405.
- Hamant, O., Heisler, M.G., Jonsson, H., Krupinski, P., Uyttewaal, M., Bokov, P., Corson, F., Sahlin, P., Boudaoud, A., Meyerowitz, E.M., *et al.* (2008). Developmental patterning by mechanical signals in *Arabidopsis*. *Science* 322, 1650-1655.
- Hofmeister, W. (1863). Zusätze und Berichtigungen zu den 1851 veröffentlichten Untersuchungen der Entwicklung höherer Kryptogamen. *Jahrbucher für Wissenschaft und Botanik* 3, 259-293.

Johnston, C.A., Hirono, K., Prehoda, K.E., and Doe, C.Q. (2009). Identification of an Aurora-A/Pins/LINKER/Dlg spindle orientation pathway using induced cell polarity in S2 cells. *Cell* **138**, 1150-1163.

Katsuta, J., Hashiguchi, Y., and Shibaoka, H. (1990). The Role of the Cytoskeleton in Positioning of the Nucleus in Premitotic Tobacco by-2 Cells. *J Cell Sci* **95**, 413-422.

Korn, R.W., and Spalding, R.M. (1973). The Geometry of Plant Epidermal Cells. *New Phytologist* **72**, 1357-1365.

Kost, B., and Chua, N.H. (2002). The plant cytoskeleton: Vacuoles and cell walls make the difference. *Cell* **108**, 9-12.

Lewis, F.T. (1928). The Correlation Between Cell Division and the Shapes and Sizes of Prismatic Cells in the Epidermis of Cucumis. *The Anatomical Record* **38**, 341-376.

Li, W., Kale, A., and Baker, N.E. (2009). Oriented cell division as a response to cell death and cell competition. *Curr Biol* **19**, 1821-1826.

Lintilhac, P.M., and Vesecky, T.B. (1984). Stress-induced alignment of division plane in plant tissues grown *in vitro*. *Nature* **307**, 363-364.

Lloyd, C.W. (1991). How Does the Cytoskeleton Read the Laws of Geometry in Aligning the Division Plane of Plant-Cells. *Development*, 55-65.

Lynch, T.M., and Lintilhac, P.M. (1997). Mechanical signals in plant development: a new method for single cell studies. *Dev Biol* **181**, 246-256.

Miri, M., and Rivier, N. (2006). Universality in two-dimensional cellular structures evolving by cell division and disappearance. *Phys Rev E Stat Nonlin Soft Matter Phys* **73**, 031101.

Morin, X., Daneman, R., Zavortink, M., and Chia, W. (2001). A protein trap strategy to detect GFP-tagged proteins expressed from their endogenous loci in *Drosophila*. *Proc Natl Acad Sci U S A* **98**, 15050-15055.

O'Connell, C.B., and Wang, Y.L. (2000). Mammalian spindle orientation and position respond to changes in cell shape in a dynein-dependent fashion. *Mol Biol Cell* **11**, 1765-1774.

Palevitz, B.A. (1987). Actin in the Preprophase Band of *Allium-Cepa*. *Journal of Cell Biology* **104**, 1515-1519.

Patel, A.B., Gibson, W.T., Gibson, M.C., and Nagpal, R. (2009). Modeling and inferring cleavage patterns in proliferating epithelia. *PLoS Comput Biol* **5**, e1000412.

Peshkin, M.A., Strandburg, K.J., and Rivier, N. (1991). Entropic predictions for cellular networks. *Phys Rev Lett* **67**, 1803-1806.

Pickett-Heaps, J.D., and Northcote, D.H. (1966). Organization of microtubules and endoplasmic reticulum during mitosis and cytokinesis in wheat meristems. *J Cell Sci* **1**, 109-120.

Prusinkiewicz, P., and Lindenmayer, A. (1990). *The Algorithmic Beauty of Plants* (New York, Springer-Verlag).

Quyn, A.J., Appleton, P.L., Carey, F.A., Steele, R.J., Barker, N., Clevers, H., Ridgway, R.A., Sansom, O.J., and Nathke, I.S. (2010). Spindle orientation bias in gut epithelial stem cell compartments is lost in precancerous tissue. *Cell Stem Cell* **6**, 175-181.

Rivier, N., and Lissowski, A. (1982). On the correlation between sizes and shapes of cells in epithelial mosaics. *J Phys A: Math Gen* **15**, L143-L148.

Rivier, N., Schliecker, G., and Dubertret, B. (1995). The stationary state of epithelia. *Acta Biotheoretica* **43**, 403-423.

Saburi, S., Hester, I., Fischer, E., Pontoglio, M., Eremina, V., Gessler, M., Quaggin, S.E., Harrison, R., Mount, R., and McNeill, H. (2008). Loss of Fat4 disrupts PCP signaling and oriented cell division and leads to cystic kidney disease. *Nat Genet* **40**, 1010-1015.

Schuh, M., Lehner, C.F., and Heidmann, S. (2007). Incorporation of *Drosophila* CID/CENP-A and CENP-C into centromeres during early embryonic anaphase. *Curr Biol* **17**, 237-243.

Segalen, M., Johnston, C.A., Martin, C.A., Dumortier, J.G., Prehoda, K.E., David, N.B., Doe, C.Q., and Bellaiche, Y. (2010). The Fz-Dsh planar cell polarity pathway induces oriented cell division via Mud/NuMA in *Drosophila* and zebrafish. *Dev Cell* **19**, 740-752.

Siller, K.H., Cabernard, C., and Doe, C.Q. (2006). The NuMA-related Mud protein binds Pins and regulates spindle orientation in *Drosophila* neuroblasts. *Nat Cell Biol* 8, 594-600.

Siller, K.H., and Doe, C.Q. (2009). Spindle orientation during asymmetric cell division. *Nat Cell Biol* 11, 365-374.

Sinnott, E.W., and Bloch, R. (1940). Cytoplasmic behavior during division of vacuolate plant cells. *P Natl Acad Sci USA* 26, 223-227.

Speicher, S., Fischer, A., Knoblich, J., and Carmena, A. (2008). The PDZ protein Canoe regulates the asymmetric division of *Drosophila* neuroblasts and muscle progenitors. *Curr Biol* 18, 831-837.

Strauss, B., Adams, R.J., and Papalopulu, N. (2006). A default mechanism of spindle orientation based on cell shape is sufficient to generate cell fate diversity in polarised *Xenopus* blastomeres. *Development* 133, 3883-3893.

They, M., and Bornens, M. (2008). Get round and stiff for mitosis. *HFSP J* 2, 65-71.

They, M., Jimenez-Dalmaroni, A., Racine, V., Bornens, M., and Julicher, F. (2007). Experimental and theoretical study of mitotic spindle orientation. *Nature* 447, 493-496.

They, M., Racine, V., Pepin, A., Piel, M., Chen, Y., Sibarita, J.B., and Bornens, M. (2005). The extracellular matrix guides the orientation of the cell division axis. *Nat Cell Biol* 7, 947-953.

Traas, J., Bellini, C., Nacry, P., Kronenberger, J., Bouchez, D., and Caboche, M. (1995). Normal Differentiation Patterns in Plants Lacking Microtubular Preprophase Bands. *Nature* 375, 676-677.

Vanstraelen, M., Van Damme, D., De Rycke, R., Mylle, E., Inze, D., and Geelen, D. (2006). Cell cycle-dependent targeting of a kinesin at the plasma membrane demarcates the division site in plant cells. *Current Biology* 16, 308-314.

Walker, K.L., Muller, S., Moss, D., Ehrhardt, D.W., and Smith, L.G. (2007). Arabidopsis TANGLED identifies the division plane throughout mitosis and cytokinesis. *Curr Biol* 17, 1827-1836.

Willemsen, V., Bauch, M., Bennett, T., Campilho, A., Wolkenfelt, H., Xu, J., Haseloff, J., and Scheres, B. (2008). The NAC domain transcription factors FEZ and SOMBRERO control the orientation of cell division plane in Arabidopsis root stem cells. *Dev Cell* 15, 913-922.

Wright, A.J., Gallagher, K., and Smith, L.G. (2009). discordia1 and alternative discordia1 function redundantly at the cortical division site to promote preprophase band formation and orient division planes in maize. *Plant Cell* 21, 234-247.

## Extended Experimental Procedures:

### (2.S1) Algorithm for computing the minimal energy configuration of local cellular neighborhoods

To understand how the shape of a cell is influenced by the shapes of its surrounding neighbors, we implemented an algorithm to find minimal energy configurations of cell packing, similar to that described by Prusinkiewicz and Lindenmayer (1990). Here, we discuss the algorithm's functional form, boundary conditions, parameters, and implementation. For a diagram of the algorithmic details, see Figure 2.S1.

The algorithm assumes that, at equilibrium, apical cell areas are determined by a balance between internal cellular pressure and contractile forces along cellular edge lengths (Figure 2.S1A). For relaxation, cells are modeled as two dimensional polygons at their apical surface, and referred to as "faces." Nodes and edges are modeled, respectively, as point masses and ideal springs (Figure 2.S1A). The assumption that the nodes have mass is irrelevant at equilibrium. Internal pressure is modeled as an ideal gas. During relaxation, damping is achieved using friction, proportional to node velocity. These relationships are captured as a system of coupled ordinary differential equations:

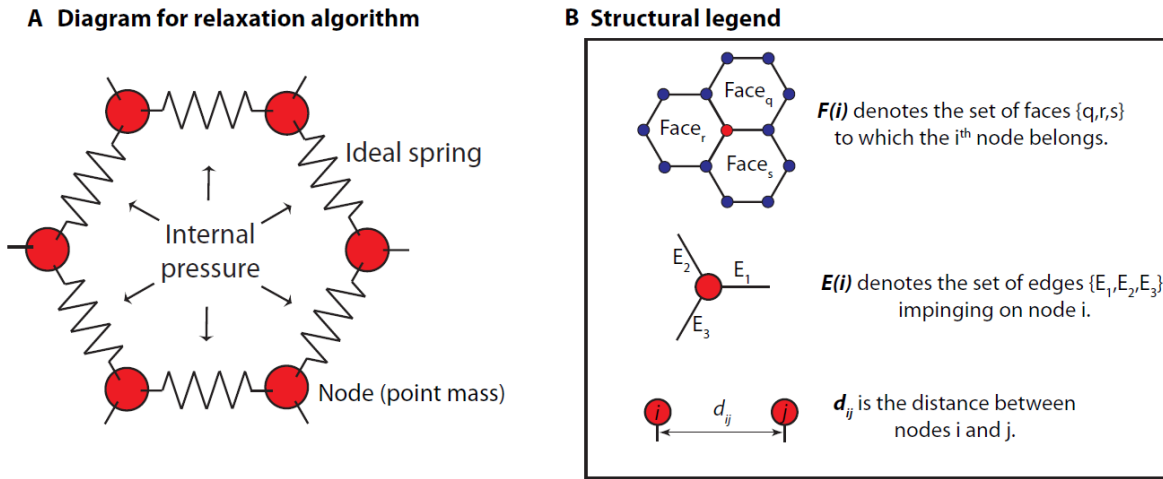
$$q_i \frac{d^2}{dt^2}(\vec{x}_i) = \left[ \sum_{\substack{j \in E(i) \\ k \in F(i)}} \vec{T}_{ij} + \frac{1}{2} \vec{P}_{ij}(k) \right] - C_i \frac{d}{dt}(\vec{x}_i) \quad (2.S1)$$

where "q<sub>i</sub>" is the mass of the i<sup>th</sup> node,  $\mathbf{x}_i$  is the 2D vector position of node i, d/dt and d<sup>2</sup>/dt<sup>2</sup> are time derivative operators, E(i) refers to the set of edges incident to node i, F(i) is the set of faces to which node i belongs,  $\mathbf{T}_{ij}$  refers to the tensional force exerted on node i by the spring connecting nodes i and j, C<sub>i</sub> is the friction coefficient for node i, and  $\mathbf{P}_{ij}(\mathbf{k})$  is the force exerted on nodes i and j due to internal pressure from face k (to which nodes i and j belong). The magnitude for the force due to internal pressure is given by the following expression:

$$\|P_{ij}(k)\| = \frac{d_{ij} n_k H_k}{A_k} \quad (2.S2)$$

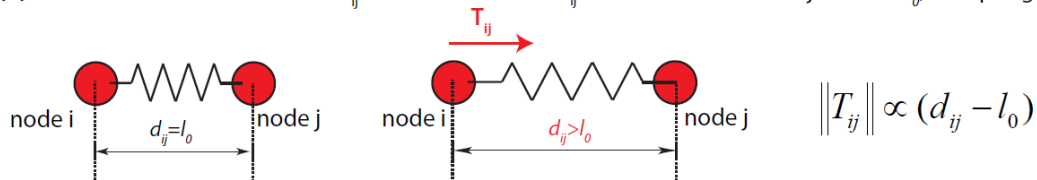
where n<sub>k</sub> is the number of moles of ideal gas inside face k, A<sub>k</sub> is the area of face k, d<sub>ij</sub> is the distance between nodes i and j, and H<sub>k</sub> encapsulates the universal gas constant as well as the temperature. We assume without loss of generality that the height of all polygonal cells is 1. Hence, to recover the force exerted by the ideal gas, we simply multiply the pressure expression by d<sub>ij</sub>, which is equivalent to the area of the interface between the two cells.

Figure 2.S1:

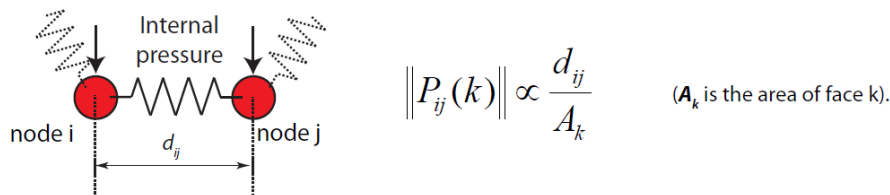


**C Outline of algorithmic terms**

(1) Node  $i$  feels a tensional force  $T_{ij}$  when the distance  $d_{ij}$  between nodes  $i$  and  $j$  exceeds  $l_0$ , the spring's rest length.



(2) Nodes  $i$  and  $j$  feel a force of expansion  $P_{ij}(k)$  due to internal pressure from within face  $k$ .



(3) A frictional force opposes the motion of node  $i$ , and is proportional to node  $i$ 's velocity.



**D. Equation used to compute the equilibrium configuration**

$$q_i \frac{d^2}{dt^2}(\vec{x}_i) = \left[ \sum_{\substack{j \in E(i) \\ k \in F(i)}} \vec{T}_{ij} + \frac{1}{2} \vec{P}_{ij}(k) \right] - C_i \frac{d}{dt}(\vec{x}_i)$$

↑  $q_i$  is the mass for the  $i^{\text{th}}$  node

↑ frictional force

tensile force      force of expansion

**Figure 2.S1, related to Figure 2.1: A diagram for the mechanical relaxation algorithm.**

**(A)** Diagram for an individual cell as represented by the relaxation algorithm. Red-filled circles represent nodes, which are assumed to behave as point masses during relaxation. Jagged lines represent ideal springs, which provide a contractile force to the cellular edge lengths. Internal pressure, which is assumed to be uniform in all directions, and which opposes this contractile force, is diagrammed using arrows. **(B)** Structural legend. The relaxation algorithm is implemented in terms of a set of interconnected nodes, edges and faces. The notation  $F(i)$  refers to the set of faces to which node  $i$  belongs. Except for cases along the boundary, in our simulations each node will belong to exactly three faces. Similarly, except in boundary cases, the  $i^{\text{th}}$  node will have exactly three edges  $E(i)$  impinging on it. The notation  $d_{ij}$  refers to the distance between nodes “ $i$ ” and “ $j$ .” **(C)** The relaxation algorithm is implemented in terms of the sum of three forces acting at the nodes. The first, tension, is implemented in terms of an ideal spring, whose force is proportional to the distance between the spring’s current length and its rest length. The second force, internal pressure, is modeled as an ideal gas. The third force, friction, opposes node motion and is implemented in order to bring the system towards a minimal energy configuration. **(D)** The general form of the equations used to numerically solve for the system’s equilibrium, in terms of forces and structural relationships between nodes, faces, and edges.

The magnitude of the tension is captured by the following Hookean relation:

$$\|T_{ij}\| = G_{ij}(d_{ij} - l_0) \quad (2.S3)$$

where  $G_{ij}$  is the stiffness constant for the spring placed between nodes  $i$  and  $j$ , and  $l_0$  is the rest length.

For our simulations, parameters were chosen to be equal for all cells. The following values were used:  $q_i = 0.0001$ , for point masses;  $l_0 = .0001$ , for the rest lengths of springs;  $C_i = 2.0$ , for the friction coefficients;  $1.0$ , for the product  $n_k H_k$ ; and  $G_{ij} = 5.0$ , for spring stiffness constants. Rest lengths were chosen such that cellular edge lengths were much longer than the rest lengths of springs at steady-state, thus placing them under considerable tension. Friction coefficients were chosen such that the system would approach steady-state within a reasonable time frame. We used free boundary conditions, where the central cell and its immediate neighbors are surrounded by three outer rows of hexagonal cells to mitigate edge effects. Equations were integrated numerically using the ode45 solver in MATLAB (Mathworks). Integration was continued until the total squared velocity of the nodes summed over the entire cell sheet dropped below an arbitrary threshold cutoff, taken to be 0.003.

## **(2.S2) Description of simulated cell divisions:**

In the main text, we use two different models of cell division: random-axis divisions and long-axis divisions (Figure 2.S6E). Here, we specify the algorithms and implementation methods that were used for each. The same algorithms were used for both simulated cell shapes and experimental cell shapes.

**(2.S2.1) Computation of the cellular long and short axes:** We defined the long and short axes of a cell in terms of an elliptical fit to the cell's vertices. To determine the ellipse of best fit, we used a direct least-squares fitting procedure, which has been described elsewhere (Fitzgibbon et al., 1999). For an improved framework that is more numerically stable, please see the following URL: <http://research.microsoft.com/en-us/um/people/awf/ellipse/fitellipse.html>.

**(2.S2.2) Definition of the long-axis division:** The division plane for a long-axis division is taken to be the short axis of the ellipse of best fit, which bisects the long axis. There is one additional caveat, which is that we require the division plane to pass through the cell's centroid. This is achieved by fitting a line through the centroid with the same orientation as the short axis. For polygonal cells, the distance between the centroid and the center of the ellipse is very small.

**(2.S2.3) Definition of the randomly oriented division:** The random-axis division model describes the division plane as a straight line passing through the

cell's centroid, with an orientation drawn from a uniform random distribution, from 0 to  $2\pi$ .

**(2.S2.4) Determination of which neighbor cells are in the division plane position:**

The neighbor cells in the division plane position are determined by finding the intersection points of the line representing the division plane with the polygonal cell cortex. The polygonal neighbors sharing the intersected edges are considered to be in the division plane position.

**(2.S2.5) Computation of the cellular centroid:** The centroid  $(C_x, C_y)$  is computed in terms of the  $N$  vertices, where the set of coordinates for vertex  $i$  is denoted  $(x_i, y_i)$ . The vertices are assumed to be ordered with counter-clockwise orientation, where vertex  $i=0$  is equivalent to vertex  $i=N$ . The centroid is found in the following manner (Bashein and Detmer, 1994):

$$C_x = \frac{1}{6A} \sum_{i=0}^{N-1} (x_i + x_{i+1})(x_i y_{i+1} - x_{i+1} y_i)$$

$$C_y = \frac{1}{6A} \sum_{i=0}^{N-1} (y_i + y_{i+1})(x_i y_{i+1} - x_{i+1} y_i) \tag{2.S4}$$

The area  $A$  of the polygon is found as:

$$A = \frac{1}{2} \sum_{i=0}^{N-1} (x_i y_{i+1} - x_{i+1} y_i). \tag{2.S5}$$

**(2.S3) Empirical analysis of proliferation parameters in the *Drosophila* wing disc:**

In order to understand the role of cleavage plane bias *in vivo*, it was necessary to understand the dynamic context in which the bias operates. To this end, we empirically measured the parameters governing cell shape emergence in the *Drosophila* wing disc. Below we describe how the empirical rate constants for the *Drosophila* wing disc were either directly computed or statistically inferred from our measurements of cytokinetic figures (Figure 2.3E; Experimental Procedures). For all probabilities and rate parameters described below, the relevant time scale,  $\tau$ , for the measurement is the duration of M-phase.

**(2.S3.1) Polygon-specific cleavage plane bias:** From a sample of 420 dividing cells and their 2946 immediate neighbors, cleavage plane bias was computed as the fraction of  $N$ -sided cells in the division plane furrow (Figure 2.3; Experimental Procedures).

**(2.S3.2) Polygon-specific division equality measurements:** For all mitotic polygon classes, we have measured the fraction of  $M$ -sided cells that give rise to a  $J$ -sided daughter, where  $M$  and  $J$  are arbitrary. We can summarize these measurements as a matrix, which is referred to as the division kernel. The division kernel was inferred from 418 cytokinetic figures (Figure 2.3E;

Experimental Procedures). Kernel values were computed according to the formula  $M+4=N_1+N_2$ , where  $M$  is the topology of the mother cell, and  $N_1$  and  $N_2$  are the topologies of the two daughter cells.

**(2.S3.3) Mitotic index for the *Drosophila* wing disc:** The mitotic index over all polygon classes,  $P(D)$ , is defined to be the percentage of cells that are in M-phase. Experimentally,  $P(D)$  is calculated as an average percentage of cells in fixed tissues that positively stain for M-phase markers. We have measured  $P(D)$  for the *Drosophila* wing disc in 96-hour wandering larvae to be approximately 1.76% (+/- .17%, corrected 95% confidence interval).

**(2.S3.4) Polygon-specific mitotic indices for the *Drosophila* wing disc:** We have found that in the *Drosophila* wing disc, the fraction of cells dividing in any one polygon class may differ from the overall mitotic index  $P(D)$ , which is an average over the different polygon classes. Therefore, there is a *conditional mitotic index*,  $P(D|N)$ , for each polygon class, which gives the fraction of  $N$ -sided cells dividing, where  $N$  ranges from 4 to 9. Equivalently,  $P(D|N)$  can be thought of as the probability in unit time  $\tau$  that a randomly selected cell is in M phase given that it has  $N$  sides. To infer  $P(D|N)$ , we used Bayes' rule:

$$P(D | N) = \frac{P(N | D)P(D)}{P(N)} \quad (2.S6).$$

Here,  $P(N|D)$  is the polygonal cell shape distribution for cells that are in M phase,  $P(D)$  is the mitotic index, and  $P(N)$  is the global distribution of polygon types.  $P(N|D)$  has been measured experimentally from 418 cytokinetic figures (Figure 2.3E; Figure 2.S3D; Experimental Procedures).  $P(N)$  was measured in a previous study (Gibson et al., 2006). Based on the assumption that empirical wing disc epithelial topology has reached steady-state, we infer that the form of  $P(D|N)$  is closely approximated ( $R^2$  coefficient  $>.99$ ) by an exponential function in the number of edges  $N$ , with exponential constant,  $K$ . This is consistent with previous measurements in plants (Dubertret et al., 1998). To compute  $K$ , we used the `cftool` function in MATLAB (Mathworks). Using all data points ( $N=4\dots9$ ), we obtain a  $K$  value of approximately 1.25. To visualize the polygon-specific mitotic index for each polygon class, see Figure 2.S2A.

**(2.S3.5) Rates of T1 transitions in the *Drosophila* wing disc:** Based on live imaging studies and the contiguity of marked cell clones, cellular rearrangement is rare in the *Drosophila* wing disc. Based on analysis of 2-cell clones, it can be inferred from a previous study that about 6% of edges undergo T1 transitions per 11 hours (Gibson et al., 2006). For an illustration of a T1 transition, see Figure 2.S6N. The 6% figure may be an over-estimate, because it is based primarily on dividing cells, which are subjected to increased mechanical stress during mitosis. If T1 transitions are more common under mechanical stress, then the true rate of cellular rearrangement might be lower than 6%.

Figure 2.S2:

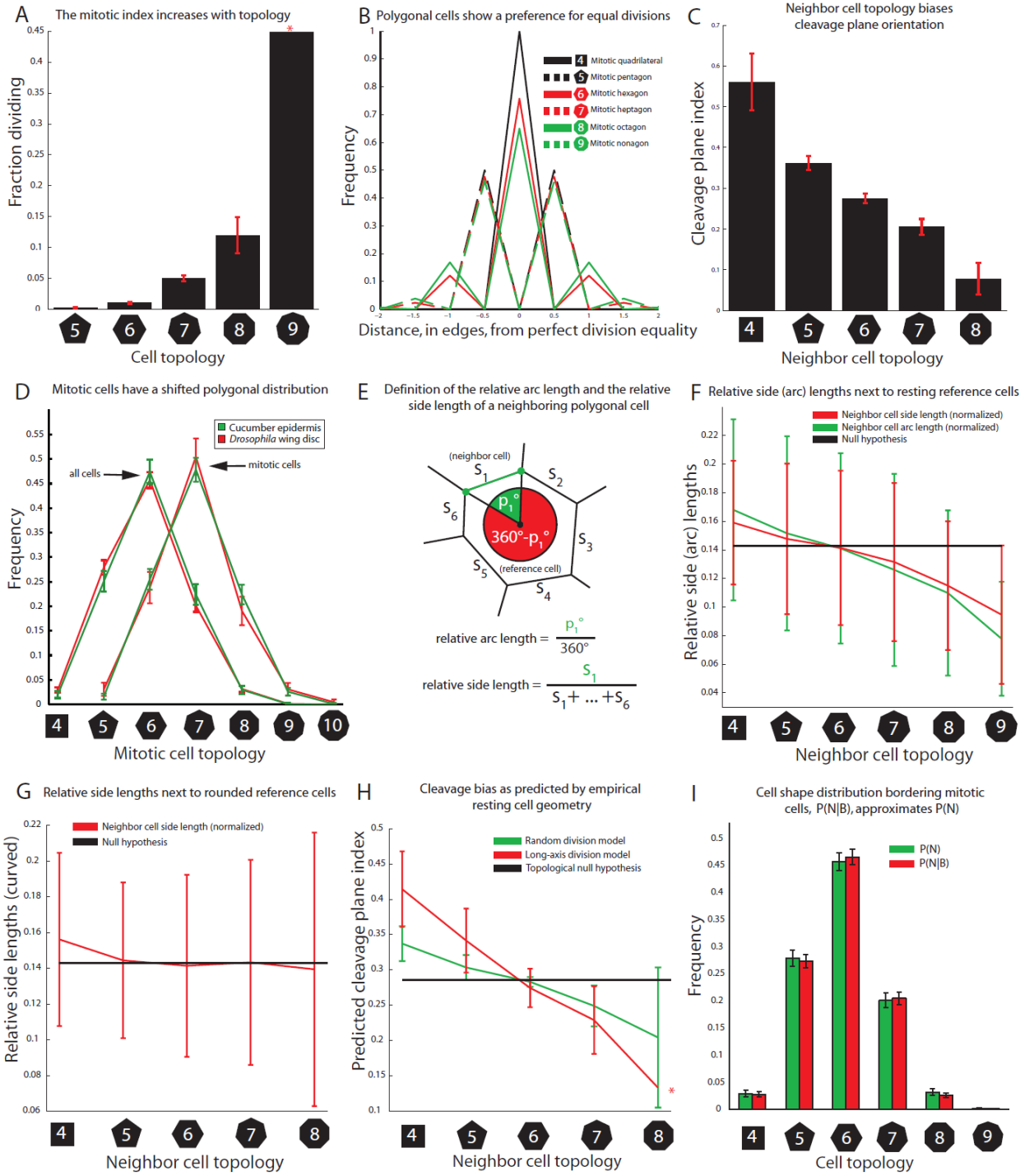


**Figure 2.S2, related to Figure 2.3: Tissue measurements reveal the kinetics and mechanisms operating during cell shape emergence in the *Drosophila* wing disc epithelium.**

**(A)** The conditional mitotic index,  $P(D|N)$ , of a polygonal cell depends its number of sides,  $N$ . For example, about 5% of heptagons ( $N=7$ ) are dividing, whereas about 10% of octagons ( $N=8$ ) are dividing. The star for nonagons ( $N=9$ ) indicates that the sample size is too small to reliably estimate the standard deviation. **(B)** Polygonal cells exhibit a strong preference to divide their junctions evenly. On the horizontal axis, zero indicates perfect division symmetry, which can only be achieved by cells when  $N$  is even (solid lines). For smaller  $N$  values, a greater frequency of divisions is perfectly symmetric. **(C)** Neighbor cell topology biases cleavage plane orientation in dividing cells (see main text, figure 2.3). **(D)** Both in *Drosophila* and in *Cucumis*, the distribution of mitotic cells recapitulates the global distribution of cell shapes, except that it is shifted by a single polygon class. **(E)** A schematic diagram illustrating two metrics: relative arc length and relative side length. Relative side length is measured in terms of a neighbor cell's perimeter. It is defined as the fraction of that perimeter. Relative arc length of a cell, by contrast, is the fraction of the internal angle in the neighboring cell, as measured from the center of mass to the pair of shared vertices. **(F)** Neither relative side length (*red*) nor relative arc length (*green*) varies substantially as a function of polygon class when the reference cell is non-mitotic (resting). **(G)** Relative side length does not vary substantially as a function of topology when the reference cell (see panel E) is a rounded-up cell, just prior to cytokinesis. **(H)** Based on empirical resting cell geometries, a long-axis division mechanism (*red*) predicts a stronger cleavage plane bias than a randomly-oriented division axis (*green*). **(I)** The distribution of cell shapes surrounding mitotic cells is almost identical to the distribution of cell shapes in the tissue as a whole.

**(2.S3.6) Lewis's law of linear areas in *Drosophila*:** In the context of a monolayer cell sheet, the average surface area of an N-sided polygonal cell is approximately linear in the value of N, a relationship known as Lewis's law (Farhadifar et al., 2007; Lewis, 1928; Patel et al., 2009; Rivier and Lissowski, 1982). Here we have quantified this relationship for the *Drosophila* wing disc. From three digitally annotated cell sheets (see Experimental Procedures), we normalized the cell areas of each sheet with respect to the average hexagonal cell area, and then grouped the cells by polygon class. For the data set, we discarded all 9-sided cells, which were rare, and also one octagonal outlier cell. For each sheet, we then used the `cftool` in Matlab (Mathworks) to fit a straight line to the average normalized cell area, as a function of polygon class. The slopes found, were, respectively, .2404, .3068, and .3357, for an average of .2943 (with standard deviation of .0489). By comparison, the slope for FT Lewis's cucumber cells (when normalized to the average hexagonal area, and excluding nonagons) is closer to .2247 for non-dividing cells, and .104 for dividing cells (Lewis, 1928).

## **(2.S4) Analysis of geometric parameters in the *Drosophila* wing disc**

In order to test whether side length might play a role in cleavage plane bias, we annotated and analyzed the apical geometry of epithelial cells in the *Drosophila* wing disc. Our measurements (Figure 2.S2F-H) suggest that this is unlikely.

**(2.S4.1) Annotation of local neighborhoods of resting cells:** Local neighborhoods surrounding 205 resting, non-mitotic cells were annotated by hand using Microsoft Powerpoint. Multiple focal planes were used to ensure accuracy of annotations. We used custom-built software to digitize the annotations for analysis in MATLAB.

**(2.S4.2) Analysis of local neighborhoods:** Two metrics were used to assess topological variability of neighbor side length in resting cells (Figure 2.S2E). The first metric is linear side length, measured from the first shared node to the second of the shared edge. We normalized this length to the total linearized perimeter of the central cell (i.e. the cell whose neighbors are being studied). The second metric is normalized arc length, which is simply the angle between the two shared nodes, as measured from the central cell's center of mass, normalized by  $360^\circ$  (Figure 2.S2E). We found that neither metric showed substantial difference as a function of polygon class (Figure 2.S2F).

**(2.S4.3) Measurements of rounded cell side lengths:** Side lengths of 100 rounded, mitotic cells were measured by hand, taking curvature into account, using ImageJ. Cell side lengths were normalized to the total perimeter of each rounded cell. We did not observe significant variability of the average normalized side length as a function of polygon class (Figure 2.S2G).

**(2.S4.4) Cleavage plane bias as predicted by resting cell geometry:** In order to estimate the cleavage plane bias that would be expected from resting (non-mitotic) cell geometry in *Drosophila*, we computed an approximate cleavage

plane bias based on a long-axis model of cell division. For comparison, we considered a uniform-random cleavage plane orientation, which was drawn from a random-number generator in MATLAB (Mathworks). We found a significantly stronger bias using the long-axis division rule (Figure 2.S2H).

## **(2.S5) Time lapse analysis of cell division in the *Drosophila* wing imaginal disc:**

In order to test whether cells in the *Drosophila* wing imaginal disc actually obey a long-axis division mechanism, we used time-lapse microscopy to study wing disc epithelial cells as they progressed from interphase through cytokinesis in *ex vivo* culture. Time lapse movies were recorded for the entire wing blade region at 63X magnification. The focal plane was adjusted manually, and guided by the neuroglian-GFP marker to stay at the level of the septate junctions. For an example, see Supplemental Movie S1.

**(2.S5.1) Dataset description:** A total of 210 cells undergoing the division process were annotated, of which 198 started in interphase, as judged by cellular morphology. The geometry of each cell was recorded using the ImageJ polygon selections tool, with nodes placed liberally in order to accurately record cellular morphology. For each such annotation, the orientation for the ellipse of best fit (computed using the ImageJ measuring tool) was recorded. Upon cytokinesis, the cell morphology was again annotated, and a second ellipse fit was made. The recorded deviation of division from the interphase long axis (see Figure 2.4B) was taken to be the angle between the two measurements. Every scoreable dividing cell was measured on the epithelium, with the exception of cells on compartment boundaries, or those rare cells that entered mitosis at the same time as an immediate neighbor. The latter were not scored to control for hypothetical mechanical influences on the spindle due to the neighboring cell's expansion.

**(2.S5.2) The correlation between the orientation of cytokinesis and orientation of the interphase long axis is roughly independent of time:** Based on analysis of 198 dividing cells, we found that the time lag between the measurement of the interphase long axis, and the final measurement of the orientation of cytokinesis, made very little difference in the correlation between the two variables (data not shown). Based on a linear interpolation to the data, on average, the deviation increased by less than one degree for each hour that elapsed between the two measurements. For instance, for those cells dividing about 20 minutes after the initial interphase measurement, the eventual cytokinetic orientation was predicted to be about 26 degrees off the long axis on average. For cells undergoing cytokinesis approximately 220 minutes after the initial measurement, the deviation is about 29 degrees. Therefore, the orientation of a cell's long axis appears to remain relatively constant with time.

**(2.S5.3) The average deviation from a long-axis division mechanism decreases as a function of relative length of the long axis to the short axis:** Based on analysis of 198 dividing cells, we found that the deviation from the long-axis division mechanism was partly a function of cell geometry. Specifically, the larger the ratio of the long axis length to the short axis length, the smaller the deviation from a long-axis division mechanism (data not shown). Specifically, cells having a long- to short-axis length ratio close to one showed a deviation from the long axis division mechanism close to the theoretically predicted value of  $45^\circ$  for a random cleavage plane. By contrast, cells having a well-defined long axis more closely obeyed the long-axis division rule. A linear fit to the data suggests that a cell having a long- to short-axis length ratio at or above approximately 4.5 should perfectly obey the long-axis division mechanism (data not shown). To conclude, this suggests that in the *Drosophila* wing disc, the spindle orientation mechanism is sensitive to the degree of elongation of the cell.

**(2.S5.4) Incorporation of the measured deviation into the original cleavage plane bias prediction:** The average measured deviation between the interphase long axis and the eventual cytokinetic orientation was approximately 27 degrees. To test the influence of this deviation on cleavage plane bias, we re-computed the bias using a 27-degree deviation from the short axis to predict the cleavage plane. We controlled for the influence of topological relationships by using the same local neighborhoods as were measured from the empirical data (see Figure 2.3). Interestingly, when including the measured deviation, we obtained a much improved bias prediction which is significantly closer to the empirically measured values (see Figure 2.4C; compare red and black curves). A similar result is obtained when the deviation from long-axis division is simulated as Gaussian noise with a 27 degree standard deviation (data not shown).

**(2.S5.5) Cell size is not predicted to play a strong role in guiding the mitotic cleavage plane:** We followed the immediate neighbors of 60 dividing cells as those cells progressed from interphase, through prophase, and into cytokinesis. To test the hypothesis that cell size might be capable of biasing cleavage plane orientation, we studied the interphase sizes of those neighbor cells which later on occupied the cleavage plane position of their mitotic neighbor. Out of 120 possible such neighbors in the cleavage plane (two for each of the 60 dividing cells), we were able to observe 116. We normalized the areas of such cells based on the average neighbor area value for each local neighborhood. Based on the data (see Figure 2.S4D), neighbor cell size is not likely to play a strong role in orienting the cleavage plane. The distribution of neighbor cell sizes in the cleavage plane position is, on average, very close to the average size for a cell neighboring a dividing cell (ie, close to 1 on average). For the 116 cells in the cleavage plane position, we computed a value of 1.0016 for the average normalized area, and a standard deviation of .2202.

## (2.S6) Empirical analysis of proliferation parameters in the dataset for *Cucumis*:

**Polygon-specific cleavage plane bias in *Cucumis*:** To compute the cleavage plane bias for the cucumber, we used an historical data set gathered by F. T. Lewis (1928) which includes three cell shape distributions of interest for cucumber cells. The first is the tissue-wide distribution of polygonal cell shapes (Lewis, 1928),  $P(N)$ , which closely resembles the distribution of cell shapes in a variety of other organisms (Gibson and Gibson, 2009), including *Drosophila* (Figure 2.S2D, *compare red and green distributions for all cells*). The second distribution measured by Lewis is that of mitotic cells,  $P(N|D)$ , which again closely resembles the distribution seen in *Drosophila* (Figure 2.S2D, *compare red and green distributions for mitotic cells*). The third distribution is  $P(N|G,B)$ . This is essentially the distribution of polygonal cell shapes located in the division plane position of cytokinetic cells (Lewis, 1928).

It is instructive to consider the ratio of the number of  $N$ -sided cells in the division plane position (i.e. the cells having edges bisected by mitotic cleavage planes) to the number of  $N$ -sided cells throughout the tissue. Upon computing this ratio, it is apparent that there is strong enrichment for some polygon classes over others in the division plane position. Below, using only the very mild assumption that cell divisions are sparsely distributed throughout the tissue, we formalize this reasoning and compute a very close approximation to the cleavage plane bias for the cucumber.

The cleavage plane bias is formally represented as  $P(G|N,B)$ , which can be understood as the *fraction of  $N$ -sided cells* neighboring a mitotic cell that are in the division plane position. In order to compute this from existing data, we can use Bayes' rule. For the cucumber, we have expressed  $P(G|N,B)$  in terms of 5 other distributions:

1.  **$P(N|G,B)$** : This is the distribution of cell shapes located in the division plane position of cytokinetic cells, as measured by FT Lewis (1928).
2.  **$P(B|G)$** : This is the fraction of cells occupying the division plane position of mitotic cells that gain a side, which is true for all such cells. Therefore,  $P(B|G)$  is always equal to one.
3.  **$P(G)$** : This is the fraction of all cells in the division plane positions of mitotic cells. Assuming sparse divisions, this is equal to twice the mitotic index, or 2 times  $P(D)$ .
4.  **$P(N|B)$** : This is the distribution of cell shapes for cells that border a cytokinetic cell. Both based on our studies of this distribution in *Drosophila* (see Figure 2.S2I) and based on maximum entropy estimates (Peshkin et al., 1991), this distribution is closely approximated by the tissue-wide distribution of cell types,  $P(N)$ .
5.  **$P(B)$** : This is the fraction of cells neighboring mitotic cells. Assuming sparse divisions, and based on the distribution of dividing cells (Figure 2.S2D), which have an average of 7 neighbors, this is approximately equal to 7 times  $P(D)$ .

Using Bayes' rule, we can approximately compute the cleavage plane bias in the following manner:

$$P(G|N, B) = \frac{P(N|G, B)P(B|G)P(G)}{P(N|B)P(B)} \quad (2.S7).$$

As discussed above,  $P(B|G)$  is equal to one, and the ratio of  $P(G)$  to  $P(B)$  is almost exactly  $2/7$ , because these two quantities are, respectively, 2 and 7 times the mitotic index,  $P(D)$ . Moreover,  $P(N|B)$  is very well approximated (see Figure 2.S2I) by  $P(N)$ . Therefore, we find that the cleavage plane bias for cucumber epidermis is well approximated by the following:

$$P(G|N, B) \approx \frac{2P(N|G, B)}{7P(N)} \quad (2.S8).$$

Both  $P(N|G, B)$  and  $P(N)$  were measured by F. T. Lewis using sample sizes of 1000 cells each, which enables us to estimate the error on the calculation. Remarkably, the cleavage plane bias for cucumber is almost indistinguishable from that of *Drosophila* (see Figure 2.3H).

## **(2.S7) Empirical analysis of cell geometry in *Cucumis* epidermis.**

To test whether a naïve long-axis model for cell division is sufficient to generate cleavage plane bias in *Cucumis*, we analyzed the epidermis of freshly-collected *Cucumis* specimens using confocal microscopy. For sample preparation details, see Experimental Procedures. The specimens, being approximately 10cm in length, and 2cm in diameter, were similar in size to those used in Lewis's original study (Lewis, 1928). The steps in our analysis are outlined below.

**(2.S7.1) The epidermis-wide distribution of cellular shapes:** We first gathered empirical statistics for the epidermis-wide distribution of polygonal cell shapes. Cells were scored in terms of the number of neighbors, from large, contiguous epidermal regions of 400 cells or more. In total, we scored 2464 cells, which have the distribution shown in Figure 2.S3B (*green*).

**(2.S7.2) Unbiased selection of a shifted cell shape distribution:** We next selected cells having the same polygon class distribution as the dividing cells collected in Lewis's original study, which is shifted to have a heptagonal mean (Lewis, 1928). For each class of  $N$ -sided cell, we selected contiguous regions of tissue, and densely scored the  $N$ -sided cells in the region before enlarging the territory to look for additional cells. We therefore obtained an unbiased sampling of cells, selected solely on the basis of polygon class, having the same distribution of polygonal shapes as the mitotic cells studied by Lewis.

**(2.S7.3) Annotation of the selected cell shapes, and determination of neighbors in the short-axis position:** For each of the selected 501 cells, we

Figure 2.S3:

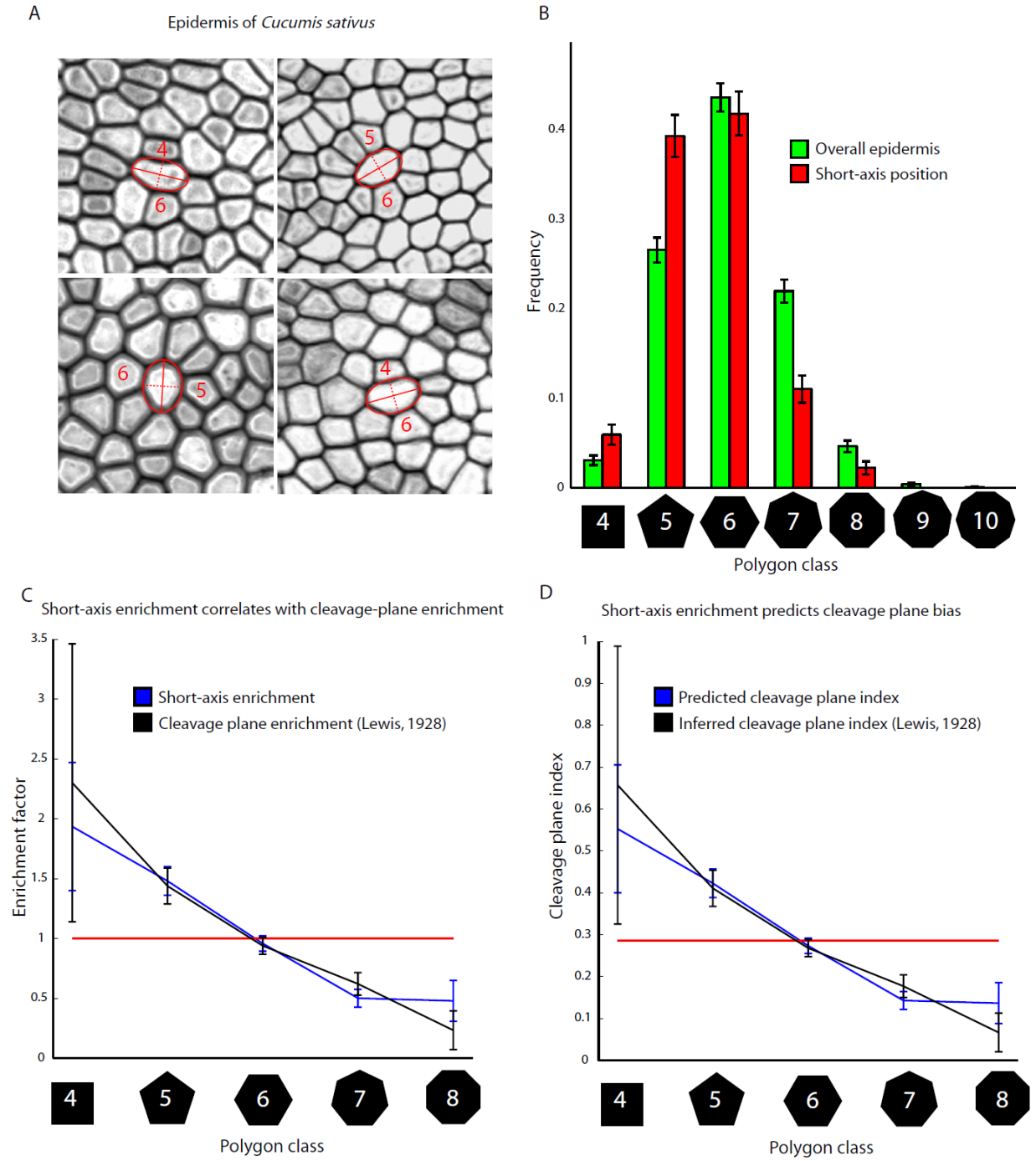
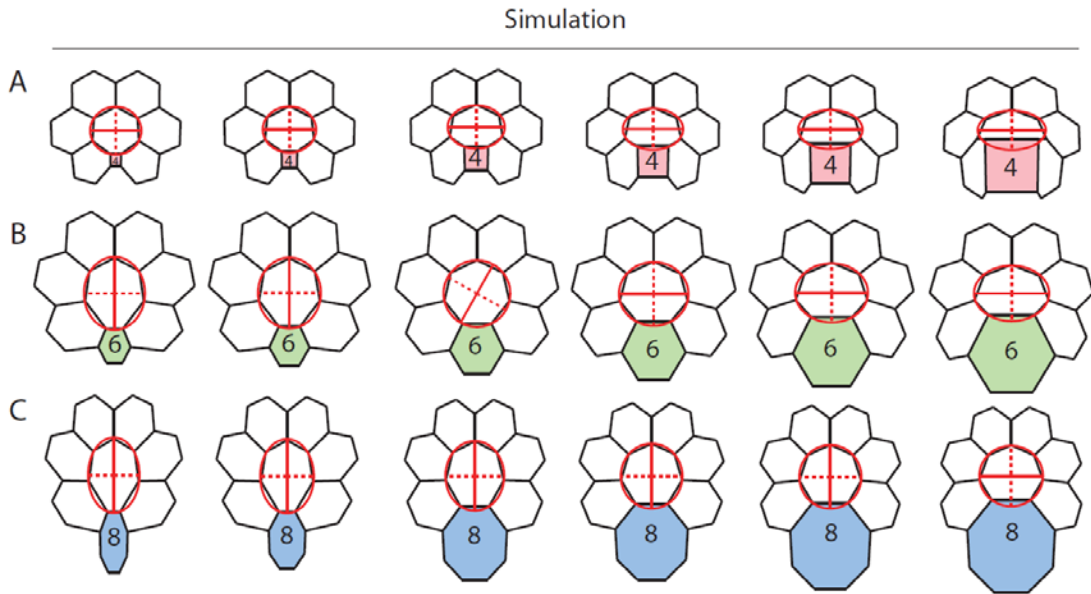


**Figure 2.S3, related to Figure 2.2.4: A long-axis division mechanism, in combination with cucumber cell geometry, is sufficient to reproduce the inferred cleavage plane bias for *Cucumis sativus*.**

**(A)** Maximum intensity projections of Z-stack, confocal images of cucumber epidermis stained with Calcofluor white. For image clarity, white content has been adjusted using Adobe Photoshop. Ellipses of best fit are shown in red, with dotted lines representing the short axis, or presumed cleavage plane. Red lettering gives the polygon class of neighboring cells in the short axis position. **(B)** Cells in the short axis position have a skewed distribution as compared with cells in the general population for cucumber epidermis. To generate the population of 1002 cells in the short axis position, in an unbiased manner, we selected 501 cells having the (shifted) distribution of cell shapes measured in Lewis's population of dividing cells (Lewis, 1928). Ellipses were then fit to these cells, which determined the population of the 1002 neighbors in the short axis position. Note the enrichment for 4-sided and 5-sided cells in the short-axis cell population. **(C)** The polygon-class specific enrichment factors (as compared with the overall epidermis) closely match between Lewis's 1928 study of 1000 cells on the ends of 500 cleavage planes, and our study of 1002 cells on the ends of 501 short axes. **(D)** The predicted cleavage plane bias correspondingly matches the inferred cleavage plane bias measured from Lewis's original data (Lewis, 1928).

Figure 2.S4:



Measurement based on live imaging

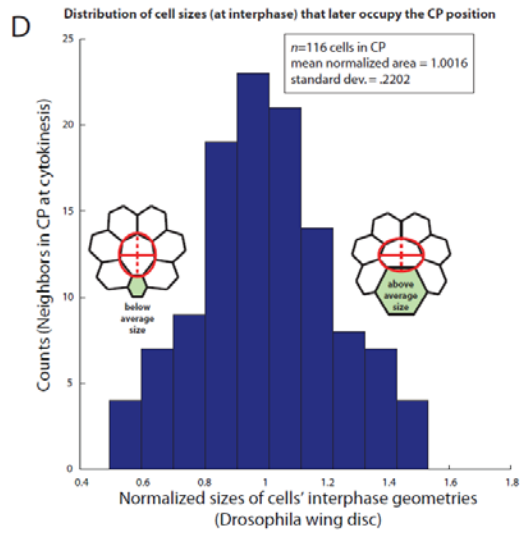


**Figure 2.S4, Related to Figure 2.5: Cleavage plane bias is robust to cell size differences in the N-sided cell,  $N$ .**

**(A)** For the case of quadrilaterals, the (effective) attraction of the short axis is robust to large variation in cell size. **(B)** Bias due to a hexagonal cell of variable size is an unstable point due to symmetry breaking. Slight perturbation above or below the target apical surface area is sufficient to rotate the long and short axes by  $90^\circ$ . **(C)** For the case of octagons, the (effective) repulsion of the short axis is robust to cell size differences, except for cases of unnatural and excessive cell enlargement (far right). **(D)** Based on live imaging analysis of 60 local neighborhoods surrounding dividing cells in the *Drosophila* wing disc, neighbor cell size at interphase is not likely to play a role in orienting the division plane. Excluding the area of the central mitotic cell, interphase cell areas were normalized to the total apical area of each local neighborhood (the average normalized area of a cell in each neighborhood is 1.0). Of the 116 observable cells in the cleavage position at cytokinesis, the average normalized area for the same cells at interphase was 1.0016 with a standard deviation of .2202. Hence, cells in the cleavage plane position at cytokinesis are of approximately average size at interphase.

manually annotated the polygonal cell geometry using the Polygon Selections tool in ImageJ. Based on these annotations, we used the measure tool in ImageJ to compute the ellipse of best fit, and a custom-made macro to plot the ellipse, along with the long and short axes. The short axis impinged on exactly two neighboring cells for each ellipse, and these were taken to be the neighbors in the cleavage plane position. From the sample of 501 annotated cells, we obtained 1002 cells in the cleavage plane position, which have the distribution shown in Figure 2.S3B (*red*).

**(2.S7.4) Computation of topological enrichment:** Note that in Figure 2.S3B, relative to the epidermis-wide distribution of cellular shapes (*green*), the frequencies of four-sided and five-sided cells are higher in the short-axis position (*red*), whereas the frequencies of heptagons and octagons are lower. To quantify the enrichment or under-representation of each polygon class, we plotted the ratio of the short-axis measurements to the epidermis-wide measurements (Figure 2.S3C, *blue*). For comparison, we also plotted the enrichment pattern for the cleavage plane position from Lewis's original data (Figure 2.S3C, *black*). Note that in both cases, there is a very clear and similar trend. Four-sided cells are enriched approximately two-fold, hexagons show approximately no enrichment, and octagons are under-represented.

**(2.S7.5) Prediction of cleavage plane bias:** Given the similar enrichment patterns in the short axis position of our randomly selected sample, and the cleavage plane position of the mitotic cells in Lewis's original dataset, we decided to compute the predicted bias as based on the short-axis position data using the same procedure used in Extended Experimental Procedures, section 6. This computation tests whether a short-axis division mechanism, combined with the epidermal geometry of *Cucumis*, is sufficient to predict the cleavage plane bias. Notably, when plotted against the cleavage plane bias inferred from Lewis's original data, the two curves are in close agreement (Figure 2.S3D). We conclude that a naïve short-axis division mechanism is sufficient to generate cleavage plane bias in *Cucumis*.

## **(2.S8) Description of global models of tissue proliferation:**

To understand the interaction between cleavage plane bias and cell shape on a tissue-wide scale, we simulated the dynamics of cell shape emergence in the context of proliferative epithelial simulations using the empirically measured parameters (see Extended Experimental Procedures, section 3). Here, we describe the details for how these simulations were implemented.

### **(2.S8.1) Topological Monte-Carlo simulations of tissue proliferation:**

In order to study the effects of cleavage plane bias in an abstract, topological framework independent of geometric parameters, we used a topological Monte-Carlo

simulator of epithelial proliferation based on the empirically measured topological division kinetics (Figure 2.S2A-C; see Extended Experimental Procedures, section 3). A non-empirical version was analyzed in a previous theoretical study (Patel et al., 2009). This framework permits simulation of very large cell sheets (on the order of 30,000 cells or more) that would not be practical in a more geometrically realistic, finite element simulation (Extended Experimental Procedures, section 8.3).

The timing model for the topological simulator is based on the exponential form for the polygon class-specific division probabilities. Cells are chosen for division, with replacement, with probability proportional to  $e^{KN}$ , where  $K$  is a constant set to 1.3 (Extended Experimental Procedures, section 3.4), and  $N$  is the polygon class. The time step is defined in terms of the mitotic index, making it approximately equal to the duration of M-phase in the cell cycle. Consistent with empirical measurements, we have chosen a mitotic index of 2% for each time step. To avoid ambiguous cases in which neighbor cells might influence each others' division probabilities in the same time step, we have forbidden cells that are immediate neighbors from dividing. This is achieved using a rejection procedure that simply re-draws the entire sample of dividing cells if the previous random draw selected at least one pair of immediate neighbor cells.

Once a cell has been chosen to divide, the next step is to specify its division plane. Topologically, this is equivalent to deciding which of the dividing cell's edges will be bisected by the division plane, which is modeled as a straight line. The first edge to be bisected is selected stochastically. This is accomplished by assigning each of the dividing cell's edges a weight according to the topology of the neighbor cell sharing that edge (recall that every edge is shared by exactly two cells). A single edge is selected from the dividing cell's total complement of edges with probability proportional to its weight. Hence, the topological weights determine the likelihood that a neighbor with a given topology will occupy the cleavage plane position. To assign weights, the function used is an inverse exponential, with a base equal to 2.7, which was determined by trial-and-error. To illustrate, a pentagon is 2.7 times as likely as a hexagon to occupy the cleavage plane position, and so on. Intuitively, cleavage plane bias can be removed in this framework by specifying a base of 1.0, in which case all topological neighbors are equally likely to occupy a division plane position. Once the location of the first edge has been determined, a new tri-cellular junction is formed in the center of the chosen edge. The second edge is specified by stochastically sampling from the empirically measured division kernel (see section 3.2 of the Extended Experimental Procedures; Figure 2.S2B), which specifies how evenly the cells divide up their junctions. In most cases, these two constraints are sufficient to specify the division plane. Occasionally, two possible division orientations are equally likely, in which case the weighting scheme is

Figure 2.S5:

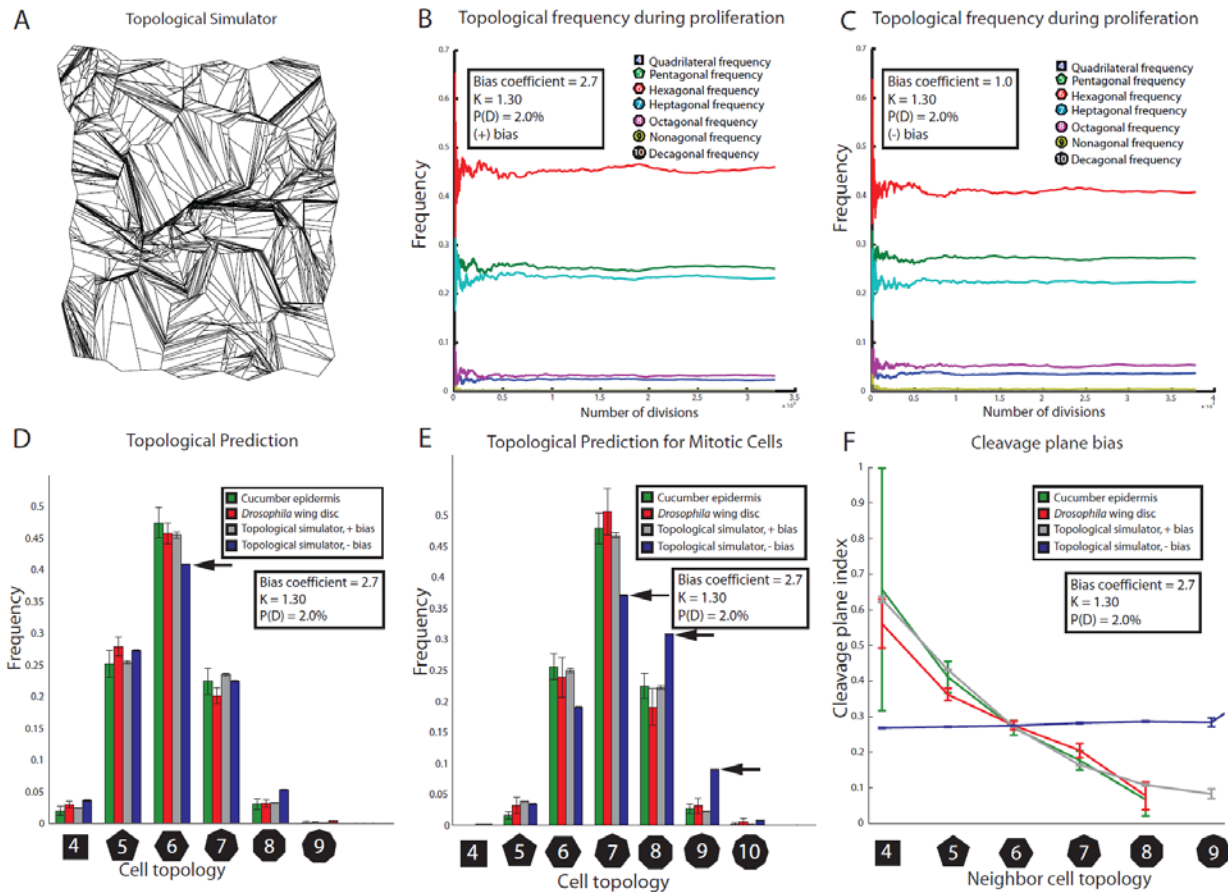


**Figure 2.S5, related to Figure 2.6 (upper panels): A topological simulator based on empirically measured division kinetics accurately captures the steady-state dynamics of the tissue, but only when cleavage-plane bias is present.**

**(A)** The topological simulator does not model cellular mechanics, but does explicitly keep track of topological neighbor relationships. Division likelihood, symmetry, and bias are matched to empirically measured statistics (see Figure 2.S2A-C). **(B-C)** In the presence or in the absence of bias, the system has approximately reached steady-state after 30000+ divisions, after starting from an initial condition of 60% hexagons, 20% pentagons, and 20% heptagons. **(D-F)** “K” refers to the exponential constant specifying the probability of cell division (see Figure 2.S2A). P(D) is the mitotic index, or proportion of all cells that are dividing per time step. The “bias coefficient” governs the strength of the cleavage plane bias (see Extended Experimental Procedures, section 6). **(D)** At steady-state, in the absence of cleavage plane bias, the frequency of hexagons is about 4% lower (*black arrow; blue*) than when cleavage plane bias is present (*gray*). **(E)** Without bias, the distribution of dividing cells shows pronounced alterations. Note

the large differences in heptagonal, octagonal, and nonagonal frequencies in the presence versus absence of bias (*black arrows, gray versus blue*). Note also the comparison with the empirically measured distributions in *Drosophila* (*red*) and *Cucumis* (*green*). **(F)** The topological Monte-Carlo framework closely captures the empirically observed cleavage plane bias.

used a second time with identical topological weights to decide (stochastically) between the two choices. Once the second edge is specified, a tri-cellular junction is inserted into the chosen cellular edge, and the two new tri-cellular junctions are then connected to result in a pair of daughter cells.

### **(2.S8.2) Topological simulation results:**

The topological simulator produces five main results. First, it closely reproduces the shape of the empirically observed cell shape distribution (Figure 2.S5D). Second, it captures cleavage plane bias accurately (Figure 2.S5F). Third, it predicts that hexagonal frequency should drop by approximately 4% in the absence of cleavage plane bias, indicating that cleavage plane bias increases the regularity of the tissue (Figure 2.S5D). Fourth, it captures the distribution of dividing cells accurately when cleavage plane bias is present (Figure 2.S5E). Fifth, when the cleavage plane bias is absent, it predicts pronounced alterations in the distribution of dividing cells. Specifically, it predicts that the frequency of heptagonal cells should decrease, and the frequency of octagons and nonagons should increase, relative to the empirical case, in the dividing cell distribution (Figure 2.S5E; *black arrows*). Taken together, the above results suggest that cleavage plane bias is an integral part of the maintenance of tissue regularity during epithelial sheet proliferation.

### **(2.S8.3) FEM model of tissue proliferation:**

In contrast to the topological simulator, which captures proliferation dynamics and cleavage plane bias in a purely topological framework, the Finite Element Model (FEM) of tissue proliferation incorporates cellular mechanics and geometry to more realistically simulate epithelial sheet proliferation. The mechanical aspects of the FEM have been described elsewhere (Brodland and Veldhuis, 2002; Chen and Brodland, 2000). Briefly, the FEM models apical contractility, cell-cell adhesion, and all other forces along the cellular edge lengths in terms of an equivalent net interfacial tension,  $\gamma$ . Each cellular edge is modeled as a rod-like, constant-force finite element, which generates  $\gamma$ . Cells, which are subject to a volume constraint, are sub-divided into sectors, each having viscosity  $\mu$  and a Poisson's ratio of zero. Thus, cytoplasm can move within the cell, but not between cells. At each dimensionless time step, subject to the volume constraint, we solved for the resultant network geometry due to interfacial tensions along the cellular edge lengths. We have incorporated polygon-specific volume constraints,  $V_N$ , in order to impose Lewis's linear law of polygonal areas (section 3.6 of the Extended Experimental Procedures), using a slope of 0.3 when cell areas are normalized to the hexagonal mean. In terms of absolute areas, the hexagonal mean was set to 60000. For our simulations, tension  $\gamma$  and viscosity  $\mu$  were, respectively, 9900 and 20. The

initial topological mesh consisted of 20 cells, with a symmetric distribution of 20% pentagons, 60% hexagons, and 20% heptagons. The simulations were run for approximately 5300 divisions. Each data point is averaged over three runs.

The timing model used for the FEM simulator is identical to the one used for the topological Monte-Carlo simulator (section 6.1 of the Extended Experimental Procedures). Once a cell is chosen to divide, its division plane is determined in one of two ways for the FEM. The first option is a uniform random division, which is implemented as a straight line passing through the cell's center, with its orientation drawn from a uniform random distribution, from 0 to  $2\pi$ . The second option is division of the long axis, which for the FEM is taken to be the principle axis of inertia. This division rule produces cleavage plane bias that is extremely close the empirically measured values (Figure 2.S6H). Here, the division plane is taken to be a straight line through the cell's center, orthogonal to the long axis. We also tested a similar algorithm using the centroid, which yielded similar results (data not shown). Following determination of the division plane, tri-cellular junctions are placed at the two points of intersection of the division plane with neighboring cells' edges, thus forming a pair of polygonal daughter cells.

In addition to mitosis, the FEM framework permits T1-type cellular rearrangements. T1 transitions (Figure 2.S6N) occur when edge lengths shorten beyond a threshold fraction,  $l_{crit}$ , of the tissue-wide average edge length. Here,  $l_{crit}$  is set to 1/20. A 4-way junction is temporarily formed, created by shrinking the original edge to zero length. Next, the 4-way junction resolves into a new pair of tri-cellular junctions, with the opposite orientation of the previous edge (Figure 2.S6N). The length of the newly-formed edge due to the subsequent T1 transition is specified by the parameter  $l_{flip}$ , which is here set to 3 times  $l_{crit}$ .

#### **(2.S8.4) FEM results:**

The results of the FEM simulator strongly support the predictions of the topological Monte Carlo simulator. For comparison, we can draw a parallel between the long-axis division mechanism used in the the FEM simulator and the topologically biased division plane orientations of the topological Monte-Carlo simulator; both mechanisms reproduce the empirically measured cleavage plane bias (Figures 2.S6H and 2.S5F). We also note similar results for the random-axis division model in the FEM simulator and the case of topologically unbiased division orientations in the topological Monte Carlo simulator (Figures 2.S6H and 2.S5F). Both of these division mechanisms effectively remove the bias. Therefore, we can directly compare the presence or absence of bias in the FEM simulator with that of the topological simulator. Like the topological

Figure 2.S6:

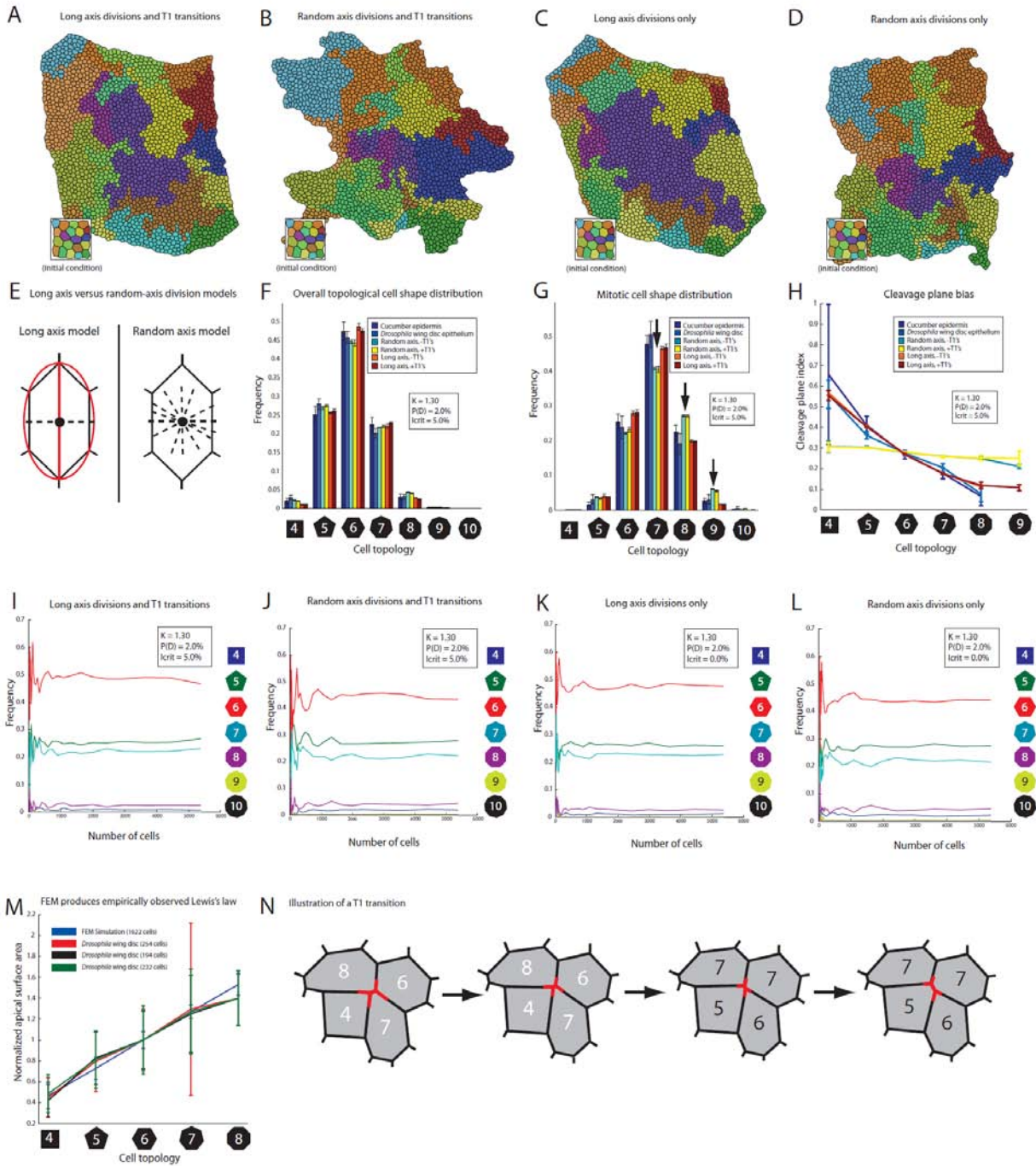


**Figure 2.S6, related to Figure 2.6 (lower panels): A finite element simulator based on empirically measured parameters accurately captures the steady-state dynamics of the tissue, but only when long-axis divisions are used.**

**(A-D)** Graphical output from the finite element model. T1 transitions result in more regular tissue patterns, and allow the cells to rearrange in order to relieve stress. Note that panels (A-D) use toroidal (wrapping) boundary conditions. Therefore, the shapes of the tissue boundaries should not be taken to indicate tissue regularity. **(E)** A graphical comparison between long-axis divisions and (uniform) random-axis divisions. **(F)** Long-axis divisions result in an increased hexagonal frequency relative to random-axis divisions. T1 transitions do not qualitatively alter this result. The FEM closely captures the empirically observed  $p^*$  distribution using the *in vivo* parameters. **(G)** The shape of the mitotic cell distribution is substantially altered relative to the empirical values when random-axis divisions are used instead of long-axis divisions (*black arrows*). This suggests that cleavage plane bias plays a role in setting the topological division rates (and hence the mitotic shift, see figure 2.S2D), and in the kinetics of side gaining. **(H)** Using random-axis divisions effectively removes the cleavage plane bias. By contrast, long axis divisions faithfully reproduce the empirically observed cleavage plane biases in fly and cucumber. **(I-L)** The system is approximately stable after 5300 divisions. **(M)** Based on polygon-specific volume constraints, the FEM simulation approximately obeys Lewis's linear law of areas, as judged by a comparison with empirical data. **(N)** During a T1-type transition, a pair of tri-cellular junctions moves closer together as the edge separating them shrinks. In our simulations, the T1 transition is only implemented if the edge length separating these two vertices drops below a critical fraction,  $l_{crit}$  of the average edge length throughout the sheet. Just prior to the transition, the edge length has shrunk to zero, forming an unstable 4-way junction (not shown). Following this unstable intermediate, the system relaxes with the opposite orientation, resulting in the generation of a new edge. Note that one pair of cells gains one edge each, whereas the other pair of cells loses one edge each.

simulator, the FEM simulations closely reproduce the empirical distribution of polygonal cell shapes, and also recapitulate the drop in hexagonal frequency in the absence of bias (Figure 2.S6F). Additionally, as predicted by the topological simulator, the distribution of mitotic cells is noticeably altered in the FEM when cleavage plane bias is absent. The frequency of dividing heptagons declines significantly, whereas the frequencies of dividing octagons and nonagons increase (Figure 2.S6G). Taken together, the above results suggest that the cleavage plane bias will have similar topological effects irrespective of the spatial or statistical mechanism used to generate it. Such topological effects appear to extend both to the population of cells as a whole, and also to the population of dividing cells.

The FEM simulator also provides additional geometrical results that cannot be predicted by the topological simulator, because the latter does not model cell geometry. We made three observations on the basis of the FEM simulator alone. First, we tested whether the presence or absence of T1 transitions would significantly alter our results. As implemented ( $l_{crit}=1/20$  the average edge length), we did not find that the presence or absence of T1 transitions qualitatively changed the simulation results. Second, for simulations including T1 transitions, we tested whether simulated tissues using random axis divisions would be more prone to T1 rearrangements, relative to simulations using long-axis divisions. Indeed, we found that the frequency of T1-type transitions was more than sevenfold higher in the random-axis division case compared with the long-axis division case. Third, we found that FEM simulations using long-axis division mechanisms produce simulated tissues that are more regular in appearance (Figure 2.S6A,C). FEM simulations using random-axis divisions, by contrast, seem to produce more irregular and mechanically frustrated tissues (Figure 2.S6B,D). Taken together, the above results suggest that long-axis division mechanisms may promote geometric in addition to topological regularity.

### **(2.S9) Geometrical analysis of cleavage plane bias:**

For the special case of a regular  $N$ -sided cell surrounded by a planar hexagonal network, we can analytically compute the approximate length of the long axis for the hexagons immediately adjacent to the  $N$ -cell. For a diagram, see figures 2.5B-C in the text (Figure 2.5C is the general case). We consider an orientation for which the  $N$ -cell,  $N$ , has its top-most edge horizontal with respect to the observer (Figure 2.5A-C, 2.5E-F). Our analysis concentrates on the hexagon that is vertically above the  $N$ -cell, here referred to as “ $M$ ,” although the same analysis would apply to any of the other hexagons.

To compute the horizontal axis,  $d_m$ , of  $M$ , we first computed the internal angles of  $M$  and  $N$  (Figure 2.5C). From geometry, the internal angles of  $N$  are found as:  $\alpha_n = \pi(N-2)/N$ . The adjacent internal angles  $\beta_m$  for  $M$  (Figure 2.5C) satisfy the condition

$\alpha_n + 2\beta_m = 2\pi$ , from which we find  $\beta_m = \pi(N+2)/(2N)$ . For the case when all edges are of unit length ( $L=1$ ; see Figure 2.5C), these internal angle constraints specify the following length for the horizontal axis of  $M$ :  $d_m = 1 + 2\sin(\pi/N)$ . For purposes of comparison with the simulation data, we have computed the approximate height of  $M$  in terms of the ellipse of best fit to the cell's vertices. For simplicity, we assume that the upper and lower halves of  $M$  are symmetrical.

To compute the vertical height (in the  $y$ -direction) of the ellipse, we used a parametric representation, where  $x(t)$  is  $A\cos(t)$  and  $y(t)$  is  $B\sin(t)$ . We chose a coordinate system such that the center of  $M$  was located at the origin. Because  $M$  is symmetric about its long and short axes, we were able to fit an ellipse to  $M$  using information from only two of its vertices: one of the two vertices at the ends of the horizontal axis, and one of the four other points. We arbitrarily chose the point  $(1/2, \cos(\pi/N))$  as well as the horizontal point  $(1/2 + \sin(\pi/N), 0)$ . To determine the parameter  $A$ , we assumed that the ellipse must pass through  $(1/2 + \sin(\pi/N), 0)$ . This constraint is equivalent to imposing a horizontal axis of  $d_m$ , which is reasonable because the ellipse is meant to represent the shape of  $M$ . To make use of the second constraint, we first solved for the  $t$  value,  $t^*$ , when the function  $A\cos(t)$  would pass through the second point (ie, when  $x$  equals  $1/2$ ). Based on  $t^*$ , we solved for a  $B$  value, which along with  $A$  determines the ellipse. Over a wide range of  $N$  values, we found that this approximation agrees with a direct least-squares elliptical fit (Fitzgibbon et al., 1999) to 13 decimal places or better (the two computations may be equivalent). Therefore, using the parameters  $A$  and  $B$ , we can accurately compute the long and short axes of the ellipse of best fit. The values of  $A$  and  $B$  are the following:

$$A = \frac{1}{2} + \sin\left(\frac{\pi}{N}\right) \quad (2.S9)$$

$$B = \frac{\cos\left(\frac{\pi}{N}\right)}{\sqrt{1 - \frac{1}{(2\sin\left(\frac{\pi}{N}\right) + 1)^2}}} \quad (2.S10).$$

We can determine which axis of  $M$  (either  $h_m$  or  $d_m$ ) is the longest axis for a given  $N$  value by comparing the ratio of  $d_m$  to the height of the vertical axis,  $h_m$ . This ratio (equivalent to the ratio  $A:B$ ) is the following:

$$\frac{d_m}{h_m} \approx \sec\left(\frac{\pi}{N}\right) \sqrt{\sin\left(\frac{\pi}{N}\right) \left(1 + \sin\left(\frac{\pi}{N}\right)\right)} \quad (2.S11).$$

The approximation comes from the assumption that  $M$  is symmetrical about its long and short axes (see above). When  $d_m/h_m$  is less than 1,  $h_m$  is the long axis. When  $d_m/h_m$  is

greater than 1,  $h_m$  is the short axis. This corresponds to the case when  $N$  is predicted to be in the division plane position of  $M$ . Because the ratio  $d_m/h_m$  is a decreasing function of  $N$  in the biological range (red, Figure 2.5D), it assumes the value  $d_m/h_m=1$  (gray, Figure 2.5D) at exactly one  $N$ -value. We refer to this value as the “critical point,” because it determines when the long and short axes rotate by  $90^\circ$ . Solving for the critical point therefore summarizes the behavior of the system. In this case, the critical point is  $N=6$ . For  $N$  values smaller than six,  $h_m$  is the short axis, which points towards  $N$ , just as we observe both in simulation and *in vivo*. Conversely, for  $N$  values larger than six,  $d_m$  is the short axis, and is parallel to the  $N$ - $M$  interface.

For the more general case when  $N$  has edges of length  $L$ , we find a different value for the horizontal axis:  $d_m = L + 2\sin(\pi/N)$ . For this case, both the ratio  $d_m/h_m$  and the critical point depend on the  $L$  value (Figure 2.5D). Using an identical procedure as before, for the ellipse we find the following values for  $A$  and  $B$ :

$$A = \frac{L}{2} + \sin\left(\frac{\pi}{N}\right) \quad (2.S12)$$

$$B = \frac{\cos\left(\frac{\pi}{N}\right)}{\sqrt{1 - \frac{L^2}{(L + 2\sin\left(\frac{\pi}{N}\right))^2}}} \quad (2.S13).$$

Here, the ratio  $d_m/h_m$  is the following:

$$\frac{d_m}{h_m} \approx \sec\left(\frac{\pi}{N}\right) \sqrt{\sin\left(\frac{\pi}{N}\right) \left(L + \sin\left(\frac{\pi}{N}\right)\right)} \quad (2.S14).$$

Larger  $L$  values tend to increase the critical point, whereas smaller  $L$  values tend to reduce it (Figure 2.5D). Given that the standard deviation is about 34% of the mean (data not shown), we wondered whether variability in  $L$  might push the critical point outside of the empirically observed range of polygonal cell shapes, making topology irrelevant. Our analysis suggests that this is extremely unlikely, because  $L$  would need to change by about 40% in order to shift the critical point by even a single polygon class (Figure 2.5D). To answer the question empirically, we computed an “effective”  $L$  value based on empirical hexagonal geometry. The effective  $L$  value is computed by considering the space of  $N$ -sided cells neighboring the set of all hexagonal cells. The edge length separating each  $N$ -cell/hexagonal cell pair is computed, and then divided by the average value of the remaining five edge lengths of the hexagon. Based on this simple algorithm, the effective  $L$  values for the *Drosophila* wing disc are summarized in table 1 (main text).

Although there is variance about the mean of about 40%, the average effective L value is close to one over a range of polygon classes. Therefore, the critical point may vary from cell to cell by a single polygon class, but on average it should be close to our analytical predictions. This suggests that angular constraints are the dominant influence behind cleavage plane bias in the *Drosophila* wing disc and potentially all other monolayer cell sheets, with lesser contributions from the differential side lengths.

## Chapter 2 Supplemental References:

Bashein, G., and Detmer, P.R. (1994). Centroid of a Polygon. In Graphics Gems IV, P.S. Heckbert, ed. (San Diego, CA, Academic Press), pp. 3-6.

Fitzgibbon, A.W., Pilu, M., and Fisher, R.B. 1999). Direct least-squares fitting of ellipses. IEEE Transactions on Pattern Analysis and Machine Intelligence 21, 476-480.

Gibson, W., and Gibson, M. (2009). Cell topology, geometry, and morphogenesis in proliferating epithelia. Current Topics in Developmental Biology 89, 87-114.

## Chapter 3

### On the origins of the mitotic shift in proliferating cell layers

William T. Gibson<sup>1,2,3,4,\*</sup>, Boris Y. Rubinstein<sup>2,\*</sup>, Radhika Nagpal<sup>4</sup>, & Matthew C. Gibson<sup>2</sup>

(1) Program in Biophysics, Harvard University (Cambridge, MA 02138, USA)

(2) Stowers Institute for Medical Research (Kansas City, MO 64110, USA)

(3) Department of Genetics, Harvard Medical School (Boston, MA 02115, USA)

(4) School of Engineering & Applied Sciences, Harvard University (Cambridge, MA 02138, USA)

\*Denotes equal contribution

### **Author contributions for Chapter 3**

Supervision of research: BR, RN, MCG.

Paper writing: WTG, MCG, RN.

Figures: WTG, BR.

Analytical computations & proofs: BR & WTG.

Data analysis: WTG, RN.

**Summary:** Across diverse species of plants and animals, monolayer cell sheets display a highly stereotyped distribution of polygonal cell shapes ranging from quadrilaterals to decagons. Intriguingly, in both the plant *Cucumis* and the insect *Drosophila*, a very similar distribution of polygonal shapes describes the population of dividing cells. Yet by comparison with the overall distribution of cell shapes, there is one major difference for the dividing cells: The mitotic cell shape distribution is shifted to have a heptagonal average, in contrast to the overall distribution of cell shapes, which has a hexagonal average. Here we examine the origins and implications of this *mitotic shift*, with particular emphasis on biological significance. We first established that the mitotic shift is completely absent for division processes exhibiting either perfectly synchronous or perfectly random mitoses. Next, using steady-state analysis, we computationally solved for the range of possible mitotic cell shape distributions. To further probe the origins of the mitotic shift, we critically examined the correlation between division probability and polygon class. Although past studies have assumed that the correlation between polygon class and division probability is always positive, in principle the relationship could be far more complex. We therefore analyzed the emergence of the mitotic cell shape distribution for an arbitrary relationship between these two variables. In the context of an analytical model of interphase cell shape evolution due to neighboring mitotic events, our analysis confirmed that a positive correlation between division probability and polygon class is most consistent, and a negative correlation least consistent, with the empirical *Drosophila* and *Cucumis* data. The simplicity of the model, combined with its quantitative accuracy, strongly suggests that side gaining due to neighboring cell mitoses is a major process in the emergence of the mitotic shift in these organisms, if not the dominant one. Having identified a plausible mechanism for generating the shifted form of the mitotic cell shape distribution, we next examined the range of possible cell shape distributions consistent with the hypothesized mechanism. Our analysis identifies severe constraints on the set of possible cell shape distributions for a system exhibiting both a mitotic shift and a monotone increasing division probability function. Given the broad conservation of these distributions in animal cells, the most parsimonious conclusion is that the mitotic shift reflects intrinsic constraints on cell shape emergence in proliferating cell layers.

## **Introduction:**

In proliferating epithelial sheets, cell shape emerges both from cell autonomous and from cell non-autonomous effects. Mitosis alters cell geometry cell-autonomously by reducing the number of neighbors of a dividing cell (ie, a hexagon may divide into a pair of pentagons). Simultaneously, mitosis also acts cell non-autonomously by generating new neighbor interfaces for cells adjacent to the recent site of division. Numerous theoretical and simulation studies, in combination with live-imaging experiments and clonal analysis in *Drosophila*, suggest that epithelial cell shape emerges due to the combined effects of cell division and cell sorting, with cell division being the dominant influence (Aegerter-Wilmsen et al., 2010; Dubertret et al., 1998; Dubertret and Rivier, 1997; Farhadifar et al., 2007; Gibson et al., 2006; Gibson et al., 2011; Rivier et al., 1995).

Notably, despite the broad range of possible cell shape distributions that have been uncovered in simulation studies using different division rule sets (Patel et al., 2009; Sahlin et al., 2009; Sahlin and Jonsson, 2010), many plant and animal species nevertheless converge on a narrow range of distributions having approximately 25% pentagons, 45% hexagons, and 20% heptagons (Gibson et al., 2006; Korn and Spalding, 1973; Lewis, 1928). The form of the distribution is likely constrained entropically (Rivier et al., 1995). Intriguingly, for both *Drosophila* and the plant *Cucumis*, the form of the mitotic cell shape distribution is nearly identical to the overall distribution, with the critical difference being that it is shifted by a single polygon class to have a heptagonal mean, in contrast to the hexagonal mean characteristic of the overall distribution (shown schematically in Figure 3.1A). The interpretation of this *mitotic shift* has been a subject of controversy. The chicken-egg nature of the debate centers on how to interpret the shift in terms of the mitotic cell cycle. In particular, based on the positive correlation between division likelihood and polygon class that can be inferred from the shift in *Drosophila* and in *Cucumis*, previous studies have suggested that polygon class might actually modulate the cell cycle (Aegerter-Wilmsen et al., 2010; Lewis, 1943). Other studies have argued that the mitotic shift would emerge even in the absence of active regulation, and may even be an unavoidable consequence of cell division (Dormer, 1980; Gibson et al., 2006; Gibson et al., 2011; Korn and Spalding, 1973; Rivier et al., 1995). Hence, there is not currently a consensus as to whether the presence or absence of a mitotic shift might reflect fundamental constraints on cell shape emergence. If such constraints exist, they might shed light on the plausibility of active regulation of the cell cycle.

Here, using a combination of computational and mathematical analysis, we critically examine the origins and implications of the mitotic shift. First, in the context of a memoryless division process, which lacks a refractory period following cell division, we establish that the mitotic shift is completely absent, and hence not required for a proliferating cell layer. We also find that a mitotic shift is absent for a cell layer dividing with perfect synchrony. Second, using a flux-balance approach, we computationally solve for the mitotic cell shape distribution in terms of fundamental mitotic parameters in order to identify the mitotic distribution's range of possible forms. Third, in order to study the emergence of the mitotic shift in terms of elementary processes, we develop an analytical framework in which to compute the expected mitotic cell shape distribution for an arbitrary relationship between division probability and polygon class. Using this framework, we establish that an increasing division likelihood function is most consistent – and a decreasing function least consistent – with the empirically observed mitotic shift in *Drosophila* and in *Cucumis*. Last, we mathematically prove that only a tiny fraction of possible cell shape distributions could exhibit both a mitotic shift and an increasing division probability function. Given the broad conservation of these distributions in animal cells, we suggest that the mitotic shift reflects intrinsic constraints on cell shape emergence in proliferating cell layers.

## Results:

*A mitotic shift is absent in a perfectly random or in a perfectly synchronous population of dividing cells.*

Previous work has suggested that at steady-state, the average polygonal cell shape for a mitotic cell should be heptagonal in the case of roughly uniform but asynchronous cell cycle times (Dormer, 1980). Moreover, empirical and computational studies have consistently demonstrated *in vivo* and *in silico* that the average dividing cell has approximately seven sides (Aegerter-Wilmsen et al., 2010; Gibson et al., 2006; Lewis, 1928). The consistency of these arguments and observations raises the question of whether a shifted cell shape distribution having a heptagonal mean is an inevitable outcome. Here we provide two counter-examples to show that a mitotic shift is in fact not a required feature of a proliferating cell layer.

For the first counter-example, consider the case of a proliferation pattern that takes the form of a Poisson process. In each time interval, consistent with this framework, we assume that there is a tiny probability  $q$  that any particular cell will divide in that interval. The value of  $q$  is small enough and the time interval short enough to ensure that the probability of dividing twice in the same interval is negligible. We find *in silico* (data not shown) that this process has no mitotic shift whatsoever. To analyze this result, we can write the conditional probability  $P(D|N)$  that a cell will divide given that it has  $N$  neighbors in terms of Bayes rule:

$$P(D|N) = \frac{P(N|D)P(D)}{P(N)} \quad (3.1),$$

where  $P(N|D)$  is the distribution of dividing cells,  $P(D)$  is the fraction of dividing cells per time step, and  $P(N)$  is the steady-state distribution of polygonal cell shapes. Note that by construction, for the memoryless Poisson process, every cell has the same division probability  $q=P(D)$  irrespective of its number of neighbors. Therefore, in the above relationship, mitotic distribution  $P(N|D)$  is identically equal to the overall cell shape distribution  $P(N)$ , and the mitotic shift is completely absent.

For a second counter-example, consider a population of dividing cells exhibiting perfect synchrony. In this example, every cell has an identical cell cycle length and the cell cycles are perfectly synchronized. Here, because every cell divides simultaneously, the fraction of dividing hexagonal cells is identically equal to the fraction of hexagonal cells overall. Similar reasoning leads to the same conclusion for all other polygon classes. Therefore, a mitotic shift is also impossible for the case of perfect synchrony.

The above examples stand in contrast to the situation in the *Drosophila* wing disc and in the epidermis of *Cucumis*, in which cell cycle progression is neither perfectly synchronous nor perfectly random. In these systems, moreover, the mitotic distribution is shifted to have a heptagonal mean. While stochastic in their division cycles, cells in these systems nevertheless have a refractory period imposed by the cell cycle during which division is temporarily precluded (Milan et al., 1996). The refractory period may participate in the emergence of the heptagonal mean by allowing cells time to gain additional neighbors prior to the next division. Nevertheless, this refractory period is not sufficient to generate the shifted overall form of the mitotic distribution, which has been

Figure 3.1:

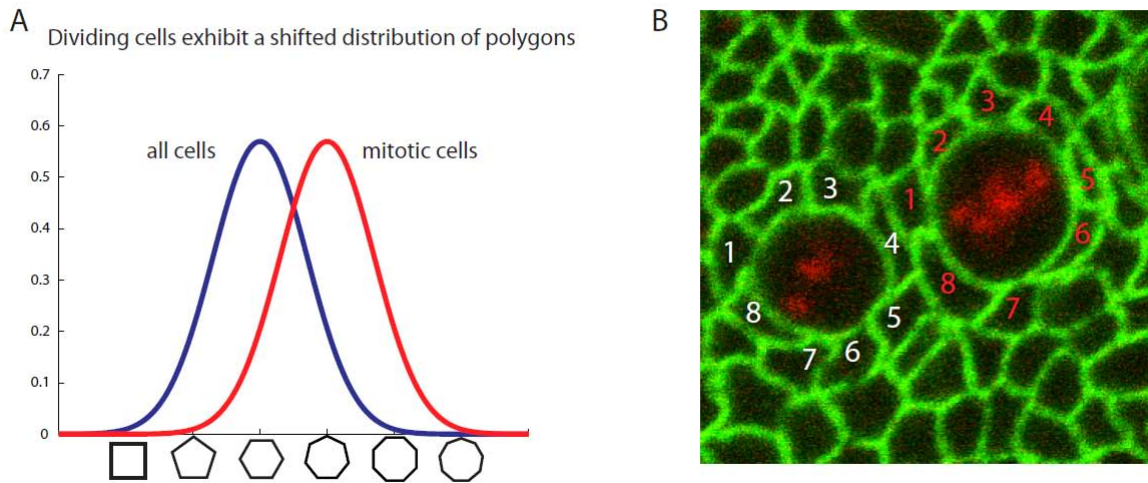


**Figure 3.1: (A)** A schematic illustration of the mitotic shift. Cell shape distributions are depicted as being perfectly Gaussian. The overall distribution of cellular shapes (*blue*) has a hexagonal mean. By contrast, the mitotic cell shape distribution (*red*) is shifted to have a heptagonal mean. Hence, one distribution is approximately a shifted version of the other. **(B)** An image of two cells entering metaphase in a live-imaged epithelium of the *Drosophila* wing imaginal disc. Neuroglian-GFP (*green*) marks the septate junctions. Histone H2RFP (*red*) marks chromatin.

shown by simulation studies to be emergent and model dependent (Aegerter-Wilmsen et al., 2010; Gibson et al., 2011). Below, we consider the constraints on the form of the mitotic cell shape distribution, and the constraints on its emergence.

### *A flux-balance approach to identify a steady-state mitotic cell shape distribution*

For an approximate set of constraints on the form of the mitotic cell shape distribution, we can adapt a previously studied equation describing the steady-state topological balance in the tissue, re-writing it to emphasize the relationship between the distribution of mitotic cells and the overall distribution of cells (Rivier et al., 1995):

$$\begin{aligned}
 P(N|D) = & 2 \left[ \sum_{k=N}^{\infty} P(k|D) \Gamma(k \rightarrow N) \right] \\
 & - P(N)[A(N) + D] \\
 & + P(N-1)[A(N-1) + B]
 \end{aligned} \tag{3.2}$$

$P(N|D)$  is the frequency of  $N$ -sided mitotic cells, and  $P(N)$  is the frequency of  $N$ -sided cells in the tissue overall. The first term represents the aggregate pool of daughter cells produced autonomously by mitosis. Specifically, it is the probability that a dividing cell has  $k$  sides,  $P(k|D)$ , times the probability that a dividing  $k$ -sided cell gives rise to an  $N$ -sided daughter,  $\Gamma(k \rightarrow N)$ , summed over all possible values of  $k$ . The factor of two is present because there are two opportunities to create an  $N$ -sided daughter at every division (mother cells give rise to two daughters). The second term represents the aggregate loss of  $N$ -sided cells to the  $N+1$  sided cell pool due to neighbor gaining events resulting from neighbor cell mitoses. The third term represents the aggregate gain of  $N$ -sided cells from the  $N-1$  sided cell pool due to neighbor cell mitoses. The parameters  $A$ ,  $B$ , and  $D$  are each functions of a single tissue-specific parameter and the first negative moment of  $P(N|D)$  (Rivier et al., 1995). Using data from previous studies, in which empirical measurements were made for  $\Gamma(k \rightarrow N)$  and  $P(N)$ , we can search the function space of mitotic cell shape distributions,  $P(N|D)$ , as the tissue-specific parameter varies (Aegerter-Wilmsen et al., 2010; Gibson et al., 2011; Lewis, 1928).

Interestingly, we find that the solution obtained for  $P(N|D)$  is exquisitely sensitive to the tissue-specific parameter, both for the case of *Drosophila* and for the case of *Cucumis*. In a disjoint but severely narrow range of parameter values for each organism, we obtain a well-defined probability distribution, with a heptagonal maximum (Figure 3.2A-B). This approach may suggest that other factors besides the division kernel are at work, because the results do not perfectly match the empirical data. However, the result is ambiguous, because it is sensitive to noise in the measured parameters. Moreover, equation (3.2) assumes that cleavage planes are randomly oriented with respect to neighboring polygons, which recent work suggests is an oversimplification (Gibson et al., 2011). Nevertheless, equation (3.2) suggests that strong algebraic constraints limit the form of the mitotic cell shape distribution when the division

kernel and the resting cell shape distribution are determined.

### *A probabilistic framework for studying the emergence of the mitotic shift*

While the population-level, flux-balance methods used in the previous section are powerful, such approaches are not ideal for considering systems involving active regulation of the cell cycle by geometrical feedback, which previous studies have suggested might be at work (Aegerter-Wilmsen et al., 2010; Lewis, 1943). Therefore, we developed an approach that would permit investigation of theoretical division rules having arbitrary correlations between division likelihood and polygon class. Our method does not require mechanistic knowledge of the causal basis for these correlations, which previous work suggests are emergent and potentially very complex (Aegerter-Wilmsen et al., 2010; Dubertret et al., 1998; Dubertret and Rivier, 1997; Gibson et al., 2011; Korn and Spalding, 1973; Rivier et al., 1995; Sahlin et al., 2009; Sahlin and Jonsson, 2010). An added benefit of this approach is its efficiency. To restrict the search space of potential correlation functions, we can infer an approximate correlation from equation (3.1), and then search the parameter space so as to minimize the distance between the empirical and the predicted form of mitotic cell shape distribution. This approach is simpler than searching the large parameter space of equation (3.2). Our analysis depends on the following two assumptions:

- (1) The distribution of neighboring cells surrounding dividing cells is approximately the same as the overall distribution of cell shapes,  $P(N)$ , which is at steady-state. This eliminates the tissue-specific parameter used in the previous section and is approximately correct empirically.
- (2) Cell rearrangement is minimal or absent. Hence, our analysis focuses exclusively on mitosis.

In addition to these assumptions, we additionally impose the following two relationships, which permit arbitrary functional dependence:

- (3) The conditional division probability  $P(D|N)$  has some arbitrary functional form  $F(N)$  at steady-state.
- (4) The conditional probability  $Q(m)$  that a dividing  $m$ -sided cell orients its cleavage plane so as to cleave its common interface with an  $N$ -sided cell has some functional dependence, which is either completely random, given by  $\frac{2}{m}$ , or given by the empirical values described in a previous study, which are biased in the direction of smaller  $N$ -values (Gibson et al., 2011).

The algorithm to compute the mitotic cell shape distribution is written exclusively in terms of side-gaining events. Side-gaining is a direct consequence of neighbor cell mitosis, wherein the mitotic neighbor cleaves its common interface with the cell in question, thereby creating two edges where only one existed previously, and hence

Figure 3.2:

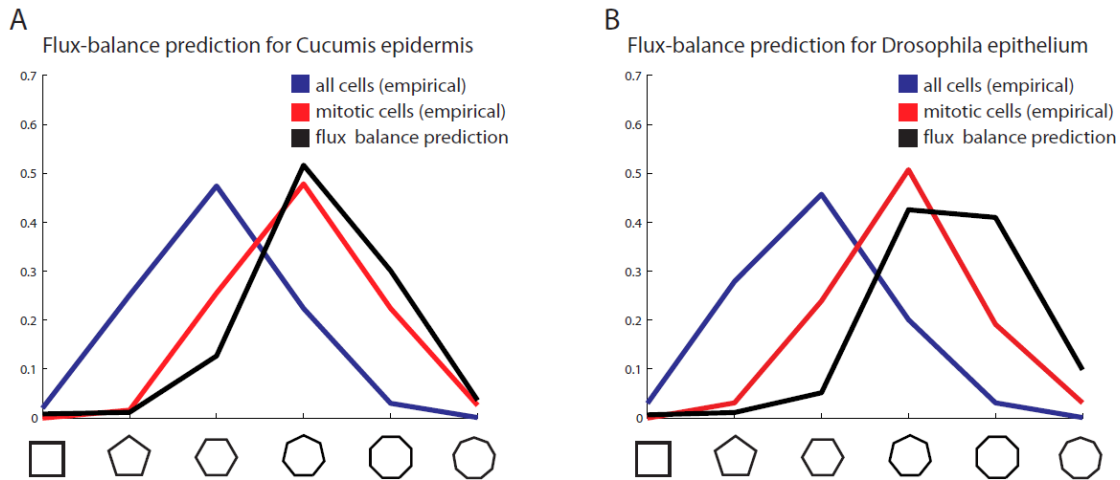


**Figure 3.2:** Flux-balance predictions for the mitotic shift in the *Drosophila* wing disc epithelium and in the epidermis of the plant *Cucumis*. **(A)** In *Cucumis*, the empirical mitotic cell shape distribution (red) is approximately an integer shift of the empirical, tissue-wide distribution of shapes (*blue*). The flux-balance prediction for the mitotic cell shape distribution (*black*) takes empirical parametric measurements, the empirical cell shape distribution, and a single tissue-specific parameter as inputs. Note the deviation from the empirical curve. **(B)** For *Drosophila*, the flux-balance prediction (*black*) is less accurate (*compare black and red curves*), potentially suggesting that other factors are required to predict the emergence of the mitotic shift.

increasing the recipient cell's polygon class by a single edge. Note that side gaining only occurs when the mitotic neighbor's cleavage plane orients in the cell's direction; otherwise no such common interface is cleaved, and the cell's polygon class remains unchanged. Side-gaining is therefore a binary event; for each neighbor cell division, the cell in question either gains a single side or it does not.

For analysis, we assume that cell cycle times are asynchronous and stochastic. Using this approach, after  $k$  neighbor cell divisions, a polygonal cell can gain at minimum zero sides (if none of the cleavage planes point in its direction), and at most  $k$  sides (if all of the cleavage planes point in its direction). Side-gaining events are assumed to be independent.

In order to approximately compute the subset of these neighbors that divide in the orientation of the cell in question, we introduce the probability  $Q(m)$  that an  $m$ -sided cell gains a new cell contact due to the mitosis of a neighboring cell.  $Q(m)$  has previously been reported to negatively correlate with the polygon class,  $m$  (Gibson et al., 2011). In terms of  $Q(m)$ , we developed a simple framework in which to compute the probability  $G(m,k,V)$  that an  $m$ -sided cell gains  $k$  sides after  $V$  of its neighbor cells have divided (see Figures 3.3A-B). For example, the probability  $G(m,0,V)$  that the  $m$ -sided cell gains zero sides after  $V$  divisions is the following:

$$G(m,0,V) = (1 - Q(m))^V \quad (3.3)$$

This is simply the probability of *not* gaining a side,  $1 - Q(m)$ ,  $V$  times in a row. The opposite situation occurs when *every* neighbor cell division results in a side-gaining event. For this case:

$$G(m,k,k) = \prod_{r=0}^{k-1} Q(m+r) \quad (3.4)$$

where  $r$  is an index, and  $G(m,k,k)$  is the probability of gaining  $k$  sides after  $k$  divisions. For instance, the probability that a hexagon gains two sides after two neighbor cell divisions is simply the probability  $Q(6)$  that a hexagon gains one side due to a neighboring division to become a heptagon, times the probability  $Q(7)$  that the newly-formed heptagon gains one side to become an octagon.

Visually, the function  $G(m,k,V)$  can be represented as a simple binary tree (Figure 3.3A-B). Figure 3.3A illustrates that multiple stochastic trajectories can lead to the same eventual side-gaining outcome. For instance, the chance that a hexagon gains zero, one, or two sides after two neighboring divisions is illustrated graphically in Figure 3.3B. In order to compute the chance of a particular eventual outcome, the paths leading to that outcome must be integrated. For instance, there is only one path leading to a hexagonal fate (Figure 3.3B, bottom line). By contrast, the heptagonal fate has two paths impinging on it, which must be summed to determine the chance of the hexagon transitioning to a heptagon.

Algebraically, the probability  $G(m,k,V)$  that an  $m$ -sided polygon gains  $k$  sides after  $V$  neighbor cell divisions can be computed in terms of the following recursion relation:

$$G(m,k,V) = G(m,k,V-1)(1-Q(m+k)) + G(m,k-1,V-1)Q(m+k-1) \quad (3.5).$$

The recursion relation has two terms because there are two ways to reach  $G(m,k,V)$  from the previous division step  $V-1$ . One way is to have gained  $k$  sides already after  $V-1$  divisions, and then to gain no sides on the  $V^{\text{th}}$  division. This is equivalent to following a horizontal path on the binary tree (Figure 3.3A). The other way is to have gained  $k-1$  sides after  $V-1$  divisions, and to gain the  $k^{\text{th}}$  side on the  $V^{\text{th}}$  division. This corresponds to taking one of the inclined paths on the binary tree. In this simple Markovian framework, it is then straightforward to compute the likelihood of each possible trajectory for the side-gaining dynamics of an  $m$ -sided cell.

Having defined the side-gaining probability of a cell given a particular number of neighboring cell divisions, we next determined the expected number of dividing neighbors  $J_m$  for a polygonal cell having  $m$  neighbors. In particular, we computed the average number of such neighbors expected to divide prior to the  $m$ -sided cell itself. To derive  $J_m$  in terms of the function  $F$  (see assumption #3 above), we modeled proliferation as a Poisson process in which  $P(D|N)$  is given by  $F(N)$ .

For this analysis, time is partitioned into tiny intervals of width  $\Delta$ . The probability that the  $m$ -cell divides is  $d_m$ , and the probability that the  $k$ -cell divides is  $d_k$ . Hence, there are four possibilities that can occur in a given time bin:

- (1) Both cells divide in the time window, with probability  $d_m d_k$ .
- (2) Neither cell divides in the time window, with probability  $1 - d_m - d_k + d_m d_k$ .
- (3) The  $m$ -cell divides but the  $k$ -cell does not, with probability  $d_m - d_m d_k$ .
- (4) The  $k$ -cell divides but the  $m$ -cell does not, with probability  $d_k - d_m d_k$ .

We choose a sufficiently small  $\Delta$  such that the probability of more than one event occurring in the same time bin is negligible, for any combination of polygon classes. For this choice of  $\Delta$ , the term  $d_m d_k$  effectively drops out of the above expressions. This allows us to classify a given time bin into one of two categories. In the first and overwhelming majority of bins, no event will occur, which happens approximately with probability  $1 - d_m - d_k$ . The second category concerns time bins in which either the  $m$ -cell or the  $k$ -cell alone undergoes division, which approximately occurs with probability  $d_m$  or  $d_k$ , respectively. Considering the very first time bin for which a division event occurs, the probability that the  $k$ -cell divides first is approximately the following:

$$P(k = \text{first}) \approx \frac{d_k}{d_m + d_k} \quad (3.6).$$

Because we have imposed a conditional division probability function  $F(N)$  for an  $N$ -sided polygonal cell, we can compute the chance that a given neighboring cell divides prior to the central cell for a given function  $F$ . For an arbitrarily selected  $m$ -sided cell

Figure 3.3:

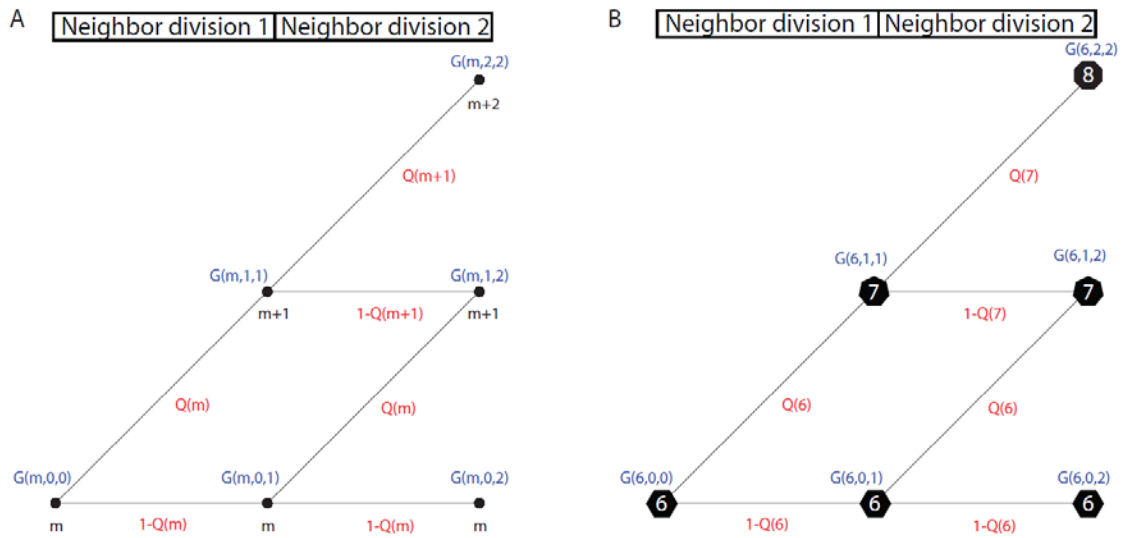


**Figure 3.3:** A binary tree representation of the side-gaining process. **(A)** The function  $G(m,n,V)$  represents the probability that an  $m$ -sided cell gains  $n$  sides after  $V$  of its immediate neighbors have divided. Side-gaining is a binary event which occurs when a neighboring cell's cleavage plane impinges on a common interface. For each neighboring division, either one or zero sides is gained.  $Q(m)$  is the probability that an  $m$ -sided cell gains a side due to a single neighboring division. On the binary tree, horizontal paths represent a failure to gain a side, which occurs with probability  $1-Q(m)$ . Elevated paths represent side-gaining events. Note that to compute  $G(m,n,V)$ , multiple paths representing different stochastic trajectories must be integrated. **(B)** A more concrete representation of the side-gaining process, which here depicts the different cell shape trajectories for a hexagon, and its potential transitions to a heptagonal or octagonal state due to side-gaining.

randomly situated in the epithelium, the chance that a single one of its neighbors divides before it does is the following:

$$\sum_{k=4}^9 \frac{F(k)}{F(m) + F(k)} P(k) \quad (3.7),$$

where the ratio term is simply equation (3.6) re-written in terms of the F function. Because the cell has  $m$  neighbors, we obtain the following average value of  $J_m$ :

$$J_m = \left\lceil m \sum_{k=4}^9 \frac{F(k)}{F(m) + F(k)} P(k) \right\rceil \quad (3.8).$$

where  $\lceil a \rceil$  denotes the least integer  $\geq a$ . This formula allows us to compute  $J_m$  unambiguously for different F functions. Our framework does not explicitly address the case in which a cell divides more than once prior to the division of a neighboring cell. Such cases are handled implicitly using the steady-state assumption and by averaging.

Having computed the expected number of sides gained due to an arbitrary number  $V$  of neighbor cell divisions in equation (3.5), for the value  $V$  we can substitute in the expected value of  $J_m$  from equation (3.8). Hence, we obtain an estimate for the number of sides gained over the course of a cell's lifetime. The expected mitotic cell shape distribution  $S(n)$  based on differential side-gaining as follows:

$$S(n) = \sum_{m=4}^n G(m, n - m, J_m) P(m) \quad (3.9).$$

The emergent form of the mitotic distribution  $S$  will in general depend on the choice of the function  $F$  (see equations 3.7-3.8). In principle, the expression for  $S$  admits completely arbitrary functional forms for  $F$ . Nevertheless, for biological systems, topological and cell-biological arguments suggest certain constraints on  $F$ 's form. For instance, we might expect the division probability to increase monotonically with polygon class, on average. The reasoning behind this hypothesis is that, irrespective of polygon class, cells would inevitably be expected to gain sides due to the divisions of neighboring cells over the course of the cell cycle, which imposes a reproducible time delay, albeit with significant stochasticity (Korn and Spalding, 1973; Milan et al., 1996). Supporting this hypothesis, analysis of the shifted distribution of cellular shapes for *Drosophila* and for *Cucumis* suggests a monotone-increasing relationship in these organisms (Dubertret et al., 1998; Gibson et al., 2011; Lewis, 1928). Specifically, the probability that an  $N$ -sided cell will divide in a short time period is well fit by an exponential or by a power-law (Supplemental Information, Section I). Below, we exploit these empirical constraints on  $F$ 's form to test the validity of the approach.

### *An empirical test of the modeling framework*

To test whether our modeling framework is able to predict the form of the mitotic cell shape distribution in a proliferating polygonal network, we focused on two well characterized tissue networks: the epidermis of the plant *Cucumis* and the epithelium of the *Drosophila* wing imaginal disc. In each case, we assumed either an exponential or power-law form for the function  $F$  (see Supplemental Information, Section I), and searched the parameter space of increasing, decreasing, and flat  $F$  functions. To measure the distance between the empirical and the predicted form of the mitotic cell shape distribution, we used the square of the L2-norm,  $(L2\text{-norm})^2$ . Strikingly, for increasing  $F$  functions, the predicted mitotic distribution  $S(n)$  closely matches the empirical distribution of mitotic cells (Figures 3.4B-B'; 3.4C-C'). By contrast, flat or decreasing  $F$  functions failed to match the data closely (Figures 3.4B-B'; 3.4C-C'). Intriguingly, we find that cleavage plane bias improves our estimate (compare blue and red bars, Figures 3.4A-B). These results, which are consistent with more exhaustive modeling approaches, suggest that our analysis is accurate for the case of these biological networks. The results also suggest that this approach may have more general applications for simulated networks in which the function  $F$  is more elaborate. Moreover, our results are consistent with the hypothesis that side-gaining is an essential process in the emergence of the mitotic shift, if not the dominant one.

### *A mitotic shift constrains the set of possible $F$ functions*

Having examined the emergence of the mitotic cell shape distribution, we next investigated how the presence of a mitotic shift might constrain the function  $F(N)$ . While the shift observed in *Drosophila* and in *Cucumis* is approximate, for analysis we assume the case of a perfect integer shift such that the mitotic cell shape distribution  $P(N|D)$  is equal to  $P(N-1)$ , the preceding value of the overall cell shape distribution. Our analysis takes the form of a mathematical proof. We first offer the following definition:

**Definition 3.1:** A function  $G(\mathbf{X})$  is defined to be a “mean-field increasing” function if there exists *at least one* value  $X_0$  such that:

$$G(X) > G(X_0) \text{ for all } X > X_0 \quad (3.10)$$

$$G(X) < G(X_0) \text{ for all } X < X_0. \quad (3.11)$$

**Statement 3.1:** If the equilibrium cell shape distribution  $P(N)$  is uni-modal and the mitotic cell shape distribution  $P(N|D)$  is a positive unit integer shift of  $P(N)$ , then the function  $P(D|N)$  describing the proportion of diving  $N$ -sided cells is mean-field increasing in  $N$ .

Figure 3.4:

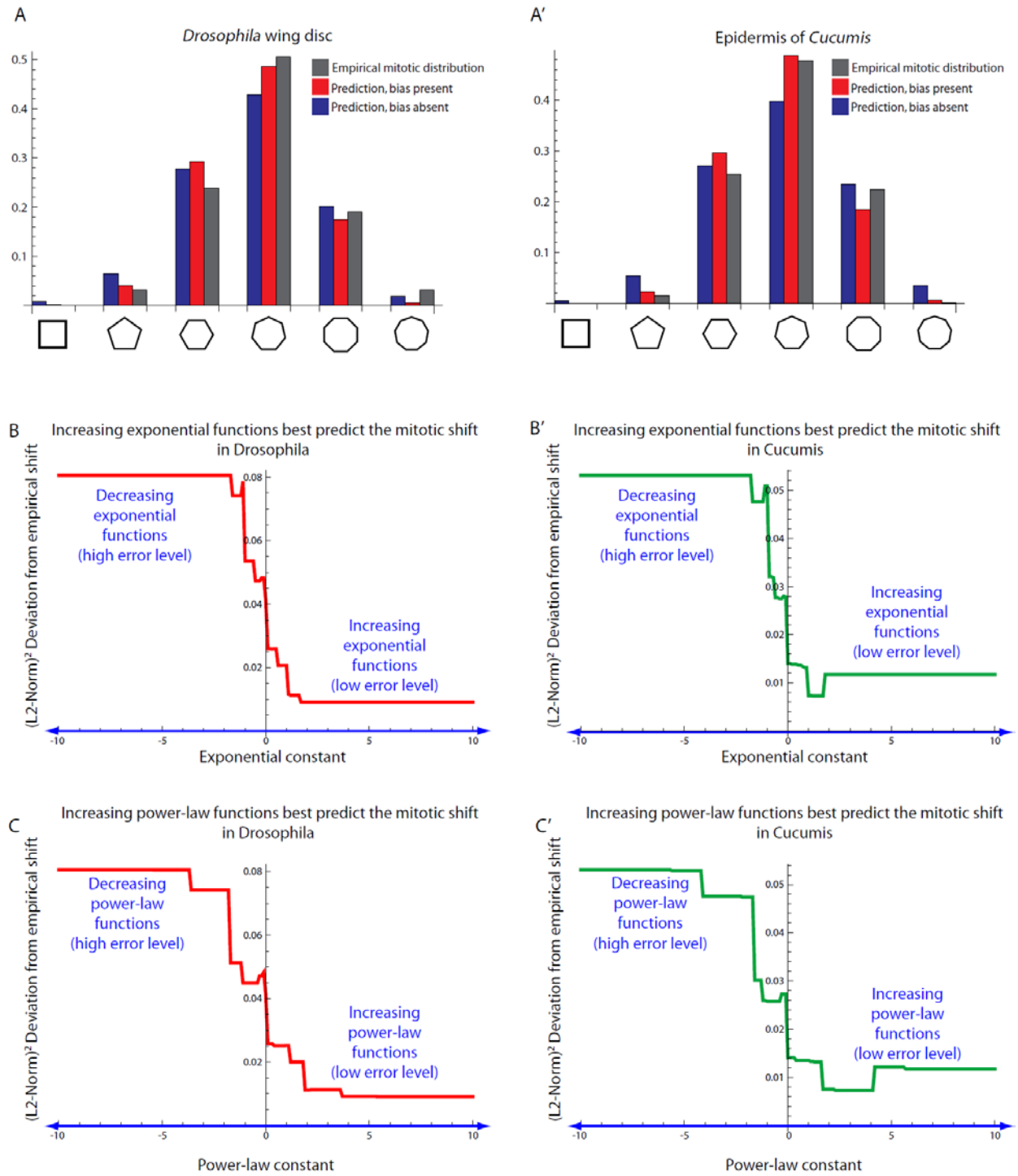


**Figure 3.4:** Computational predictions of the mitotic shift for *Drosophila* and for the plant *Cucumis* based on a stochastic model of the side-gaining process. **(A)** Prediction of the mitotic cell shape distribution for the *Drosophila* wing disc epithelium (*empirical values shown in gray*). In the absence of cleavage plane bias (*blue*), the computational prediction is not quite as accurate as when the bias is included (*red*). **(A')** Prediction of the mitotic cell shape distribution in the epidermis of *Cucumis*. Here, cleavage plane bias similarly improves the accuracy of the prediction. **(B)** For the *Drosophila* prediction, a plot of the (L2-norm)<sup>2</sup> deviation from the empirical mitotic cell shape distribution as a function of the relationship between division likelihood and polygon class. Here, division likelihood is assumed to increase exponentially as a function of polygon class. The ordinate (exponential constant) gives the precise form of the exponential. Note that positive values strongly outperform negative values. Hence, a model in which division likelihood increases with polygon class is more consistent with the data than a model in which it decreases or remains the same. **(B')** For *Cucumis*, the results are nearly identical to those of *Drosophila*. Notably, the most accurate predictions occur in a small valley in the curve (*green*), which are close to the empirically inferred values. Such fine-tuned predictions suggest that the stochastic model of side-gaining is accurate. **(C)** For the *Drosophila* prediction, a plot of the (L2-norm)<sup>2</sup> deviation from the empirical mitotic cell shape distribution as a function of the relationship between division likelihood and polygon class. Here, division likelihood is assumed to increase as a power law function of polygon class. As in the case of the exponential model, positive values strongly outperform negative values. **(C')** For *Cucumis*, the results are similar to those of *Drosophila*. As in the exponential case, the valley in deviation from the empirical values occurs in a parameter regime consistent with empirically inferred values, thus confirming that the model of side gaining is accurate.

### Proof of statement 3.1:

From equation (3.1), recall that the following relationship holds:

$$P(D|N) = \frac{P(N|D)P(D)}{P(N)}$$

where  $P(D)$  is fraction of dividing cells per time step,  $P(N|D)$  is the distribution of dividing cell shapes, and  $P(N)$  is the overall distribution of cell shapes. A perfect mitotic shift implies that the distribution of dividing cells  $P(N|D)$  is equivalent to  $P(N-1)$ .

$$P(N|D) = P(N-1) \quad (3.12).$$

Re-name  $P(D|N)$  to be called  $F(N)$ :

$$F(N) = \frac{P(N|D)P(D)}{P(N)} \quad (3.13).$$

Substituting (3.12) into (3.13), we have:

$$F(N) = \frac{P(N-1)P(D)}{P(N)} \quad (3.14).$$

Using (3.14), for the case of a perfect mitotic shift, we know the following:

$$P(N+1) = \frac{P(D)}{F(N+1)} P(N) \quad (3.15).$$

Note that this means the following:

$$P(N+1) < P(N) \text{ when } F(N+1) > P(D) \quad (3.16).$$

$$P(N-1) < P(N) \text{ when } F(N) < P(D) \quad (3.17).$$

By definition, the local maximum  $P(N')$  occurs at  $N'$  when the following conditions hold:

$$P(N) < P(N') \text{ for all } N > N' \text{ in a local neighborhood} \quad (3.18).$$

$$P(N) < P(N') \text{ for all } N < N' \text{ in a local neighborhood} \quad (3.19).$$

Therefore, using (3.16) and (3.17), a local maximum  $P(N')$  occurs at  $N'$  when the following is true:

$$F(N') < P(D) < F(N'+1) \quad (3.20).$$

Therefore, a local maximum occurs at  $N'$  when  $F$  crosses the value  $P(D)$  *from below*. Empirically we know that the function  $P(N)$  is uni-modal. Therefore, the local maximum of  $P(N)$  is also the global maximum. Hence,  $F$  must cross the value  $P(D)$  from below exactly once, and  $P(D|N)$  is a mean-field increasing function in  $N$ .

***Q.E.D.***

Practically speaking, the proof shows that for the case of a perfect mitotic shift, cells having more sides are more likely to divide as an average tendency on either side of the  $N$  value at which the distribution achieves its maximum. However, the proof does not imply monotonicity. That is, the average octagon ( $N=8$ ) is not necessarily more likely to divide than the average heptagon ( $N=7$ ). As a second example, the average quadrilateral ( $N=4$ ) is not necessarily less likely to divide than the average pentagon ( $N=5$ ). In the next proof, we show the conditions under which monotonicity is expected to hold. To facilitate description of these conditions, we offer the following two definitions:

**Definition 3.2:** A positive, monotone decreasing sequence of numbers  $H(N)$  can be said to decrease super-exponentially in  $N$  if the ratio of successive terms  $H(N):H(N+1)$  increases with each  $N$ .

**Definition 3.3:** A positive, monotone increasing sequence of numbers  $H(N)$  can be said to increase sub-exponentially in  $N$  if the ratio of successive terms  $H(N+1):H(N)$  decreases with each successive  $N$ .

**Statement 3.2:** If the steady-state polygon cell shape distribution  $P(N)$  is uni-modal with maximum  $P(N')$  at  $N'$  and the mitotic cell shape distribution  $P(N|D)$  is a positive unit integer shift of  $P(N)$ , and if the following two statements are also true:

- (i) Values of  $P(N)$  for  $N < N'$  increase sub-exponentially.
- (ii) Values of  $P(N)$  for  $N > N'$  decrease super-exponentially.

then the function  $F(N) = P(D|N)$  describing the proportion of  $N$ -sided dividing cells is strictly monotone increasing.

**Proof of statement 3.2:**

Using equation (3.14), we can compute the ratio of  $F(N+1):F(N)$  in the following manner:

$$\frac{F(N+1)}{F(N)} = \left[ \frac{P(N)}{P(N+1)} \right] \left[ \frac{P(N)}{P(N-1)} \right] \quad (3.21).$$

In order to find the set of  $P(N)$  distributions such that  $F$  is monotone increasing in  $N$ , it is sufficient to find those for which the ratio in equation (3.21) is always larger than one. Equivalently, the condition for monotonicity can be satisfied by the following condition:

$$\frac{P(N)}{P(N+1)} > \frac{P(N-1)}{P(N)} \quad (3.22).$$

The maximum value  $P(N')$  at  $N'$  will necessarily satisfy  $F(N'+1):F(N') > 1$ , because  $P(N')$  is (by the definition of a maximum) strictly bigger than  $P(N'+1)$  and  $P(N'-1)$ . Therefore, condition (3.22) holds at  $N'$ . In this case,  $N' = 6$ .

For values of  $N$  in the neighborhood of  $N < N'$ , we know that the following relationship holds:

$$P(N-1) < P(N) < P(N+1) \quad (3.23)$$

because  $P(N)$  is a monotone increasing function in this region due to the uni-modal constraint that we imposed on  $P(N)$ . Note that the only way to satisfy condition (3.22) is for the ratio of successive values of  $P(N):P(N-1)$  to decrease with  $N$ . That is,  $P(N):P(N-1) > P(N+1):P(N)$ , etc. Hence, when definition (3.3) is obeyed, and the function increases strictly sub-exponentially in the region  $N < N'$ , condition (3.22) is satisfied.

For the values of  $N$  in the neighborhood  $N > N'$ , we know that the following relationship holds:

$$P(N+1) < P(N) < P(N-1) \quad (3.24)$$

because  $P(N)$  is a monotone decreasing function in this region due to the uni-modal constraint on  $P(N)$ . By contrast with the previous situation, for  $N > N'$  the only way for  $P$  to satisfy condition (3.22) is to decrease super-exponentially such that  $P(N-1):P(N) > P(N):P(N+1)$ . Hence, when definition (3.2) is obeyed, and the function decreases strictly super-exponentially in the region  $N > N'$ , condition (3.22) is satisfied.

Because condition (3.22) can be satisfied for the maximum  $N'$ , for  $N < N'$  when definition (3.3) holds, and for  $N > N'$  when definition (3.2) holds, these conditions are sufficient to show the result for all  $N$ .

**Q.E.D.**

### **Corollary of Statement 2:**

If the steady-state polygonal cell shape distribution  $P(N)$  is uni-modal with maximum  $P(N')$  at  $N'$  and the mitotic cell shape distribution  $P(N|D)$  is a positive unit integer shift of  $P(N)$ , and if  $F(N) = P(D|N)$  describing the proportion of  $N$ -sided dividing cells is strictly monotone increasing:

Then, the following two statements are true:

- (i) Values of  $P(N)$  for  $N < N'$  increase sub-exponentially.
- (ii) Values of  $P(N)$  for  $N > N'$  decrease super-exponentially.

To see this, note that we are assuming that  $F(N)$  is monotone increasing. That is,

$$\frac{F(N+1)}{F(N)} > 1 \forall N \quad (3.25).$$

We are also assuming a unit-integer mitotic shift. Therefore,  $P(N|D) = P(N-1)$ . Using Bayes's rule, we can re-write  $F(N+1)$  as  $k \cdot P(N)/P(N+1)$ , and  $F(N)$  as  $k \cdot P(N-1)/P(N)$ , where  $k$  is a scaling factor equal to  $P(D)$ . Substituting these expressions into equation

(3.25), we obtain:

$$\frac{F(N+1)}{F(N)} = \left[ \frac{P(N)}{P(N+1)} \right] \left[ \frac{P(N)}{P(N-1)} \right] > 1 \forall N \quad (3.26).$$

Rearranging expression (3.26), we are really assuming equation (3.22) for all  $N$ :

$$\frac{P(N)}{P(N+1)} > \frac{P(N-1)}{P(N)} \forall N \quad (3.27).$$

Because we have assumed that  $P(N)$  is uni-modal, we can consider the implications of equation (3.27) both in the increasing region of  $P(N)$  and in the decreasing region of  $P(N)$ . In the increasing region of  $P(N)$ , equation (3.27) implies sub-exponential increase. To see this, note that equation (3.27) implies the following:

$$\frac{P(N+1)}{P(N)} < \frac{P(N)}{P(N-1)} \forall N \quad (3.28).$$

Hence, with each successive  $N$ , the fold-change increase decreases, which is the definition of sub-exponential increase. In the decreasing region, this also implies that the fold-change decrease increases. Hence, the function is decreasing super-exponentially, ie faster than an exponential.

**Q.E.D.**

Our analysis suggests that only certain forms of a uni-modal  $P(N)$  distribution could exhibit both a mitotic shift and a probability function that is monotone increasing with  $N$ . Thus, despite the conservation of an approximate mitotic shift in *Drosophila* and in *Cucumis*, a mitotic shift appears to be the exception, not the rule in the space of possible uni-modal cell shape distributions. While there is insufficient evidence to test for the presence of a mitotic shift in all previously studied biological cell layers, our results suggest requirements on the form of the overall cell shape distribution.

Assuming that  $F(N)$  must be monotone increasing, as our biological data and computational arguments suggest, and that  $P$  is uni-modal, we can use condition (3.27) to effectively rule out cell shape distributions that are not compatible with a mitotic shift. We refer to a tissue whose  $P(N)$  distribution obeys condition (3.27) as being “shift competent,” because a mitotic shift remains theoretically possible with a monotone  $F$  function based on the structure of  $P(N)$ .

In order to test for shift competency in a range of different cell shape distributions, using data from three previous studies, we gleaned empirically measured  $P(N)$  distributions from three animal species and five plant species (Gibson et al., 2006; Korn and Spalding, 1973; Lewis, 1928). Because the maxima of these (uni-modal) distributions always satisfy condition (3.27), we focused our analysis on the distributions’ left and right sides (with respect to the maximum value, which was hexagonal in all cases). For each distribution, we computed the following five ratios of cell shape frequencies: (1) pentagonal to quadrilateral frequencies, (2) hexagonal to pentagonal, (3) heptagonal to hexagonal, (4) octagonal to heptagonal, and (5) nonagonal to octagonal frequencies. The data is enumerated in Table 3.1, below:

**Table 3.1**

<b>Species name</b>	<b>5-sided:4-sided ratio</b>	<b>6-sided:5-sided ratio</b>	<b>7-sided:6-sided ratio</b>	<b>8-sided:7-sided ratio</b>	<b>9-sided:8-sided ratio</b>
<i>Drosophila</i>	9.469	1.639	0.440	0.158	0.044
<i>Cucumis</i>	12.550	1.888	0.473	0.134	0.033
<i>Xenopus</i>	7.625	1.479	0.424	0.272	0.154
<i>Hydra</i>	9.938	1.748	0.450	0.184	0.044
<i>Allium</i>	7.550	1.364	0.439	0.260	0.319
<i>Euonymus</i>	9.666	1.379	0.550	0.300	0.000
<i>Dryopteris</i>	6.500	1.635	0.482	0.244	0.400
<i>Anacharis</i> (leaf, abaxial)	9.600	2.479	0.1681	0.350	0
<i>Anacharis</i> (leaf, adaxial)	7.286	2.235	0.2281	0.077	0
<i>Anacharis</i> (bud)	5.364	1.525	0.444	0.000	Undefined

In Table 3.1, a species that obeys condition (3.27) will show a decreasing ratio across its entire row. By this criterion, note that the samples taken from all three of the animal species – *Drosophila*, *Hydra*, and *Xenopus* – obey condition (3.27). Moreover, two of the plant species – *Cucumis* and *Euonymus* – do as well. Of the two plant species that do not follow the rule (*Dryopteris* and *Allium*), the violation occurs for the ratio of nonagons to octagons. The measurement noise is expected to be greatest for this value, because octagons and especially nonagons are quite rare. The last tissue, *Anacharis*, is inconclusive because both its octagonal and nonagonal cells have a sample frequency of zero in its bud. In the abaxial and adaxial leaf tissues, the relationship is violated in the nonagon to octagon ratio for one case, but not in the other (Korn and Spalding, 1973). To conclude, the majority of the organisms (5/8) obey criterion (3.27). Of those that narrowly miss obeying it (3/8), the violation or inconclusive data occurs in the very noisiest region of the dataset. Therefore, a mitotic shift remains theoretically possible in these organisms.

### *Discussion*

The results presented here raise a number of important questions. A currently unresolved issue concerns the significance of the polygon-specific division probability  $F(N)$ . The framework that we have developed to model the emergence of the mitotic shift also offers a framework for testing hypotheses about the meaning of a particular form of  $F$ . For instance, a source of controversy in the field is whether the shape of a cell (or some mechanical variable correlating with shape) is involved in active modulation of the cell cycle (Aegerter-Wilmsen et al., 2010; Gibson et al., 2011; Lewis, 1943). In principle, based on a small number of assumptions, our framework could be used to detect the presence of active regulation. Given the expected  $F$  value for a particular cell cycle model, we could compare the  $F$  function that best fits the empirical data, and thus attempt to rule out one model or the other. A remaining challenge is thus to define a mapping from a particular division rule set to a particular  $F$  function.

Closely related to meaning of the polygon-specific division probability  $F(N)$  is the significance of the mitotic shift itself. Our analyses suggest that while the mitotic shift is not a required property for a proliferating cell layer, strong population-level algebraic and parametric constraints may be partly or fully responsible for its emergence, consistent with previous work (Dormer, 1980). Yet because our complementary analysis combines side gaining with an explicit  $F$  function, we can capture a broader range of possible mitotic cell shape distributions, some of which might involve active regulation, which cannot presently be ruled out (Aegerter-Wilmsen et al., 2010). Moreover, assuming the presence of the mitotic shift and an increasing  $F$  function, we find strong constraints on the form of the cell shape distribution, which are closely obeyed by 5/8 biological organisms, and narrowly violated only by the noisiest part of the dataset in 3/8 organisms. Such adherence leaves open the theoretical possibility that these organisms exhibit a mitotic shift. A critical challenge is thus to identify the minimal number of biological, geometrical, algebraic, and/or thermodynamic constraints required to predict the existence of a mitotic shift.

As a final consideration, independent of the constraints imposed by biological systems, our analysis may have implications for the space of possible *in silico* networks that could be generated by mitotic processes. Unlike biological cell layers, which we hypothesize to have very stereotyped F functions, in a simulated network, the F function could be quite elaborate. Rather than speculating about the possibility of active regulation, proliferation could be driven by such considerations. Such questions should form the basis for future work.

## References

- Aegerter-Wilmsen, T., Smith, A.C., Christen, A.J., Aegerter, C.M., Hafen, E., and Basler, K. (2010). Exploring the effects of mechanical feedback on epithelial topology. *Development* 137, 499-506.
- Dormer, K.J. (1980). *Fundamental tissue geometry for biologists* (Cambridge, UK, Cambridge University Press).
- Dubertret, B., Aste, T., Ohlenbusch, H.M., and Rivier, N. (1998). Two-dimensional froths and the dynamics of biological tissues. *Physical Review E* 58, 6368–6378
- Dubertret, B., and Rivier, N. (1997). The renewal of the epidermis: a topological mechanism. *Biophys J* 73, 38-44.
- Farhadifar, R., Roper, J.C., Aigouy, B., Eaton, S., and Julicher, F. (2007). The influence of cell mechanics, cell-cell interactions, and proliferation on epithelial packing. *Curr Biol* 17, 2095-2104.
- Gibson, M.C., Patel, A.B., Nagpal, R., and Perrimon, N. (2006). The emergence of geometric order in proliferating metazoan epithelia. *Nature* 442, 1038-1041.
- Gibson, W.T., Veldhuis, J.H., Rubinstein, B., Cartwright, H.N., Perrimon, N., Brodland, G.W., Nagpal, R., and Gibson, M.C. (2011). Control of the mitotic cleavage plane by local epithelial topology. *Cell* 144, 427-438.
- Korn, R.W., and Spalding, R.M. (1973). The Geometry of Plant Epidermal Cells. *New Phytologist* 72, 1357-1365.
- Lewis, F.T. (1928). The Correlation Between Cell Division and the Shapes and Sizes of Prismatic Cells in the Epidermis of Cucumis. *The Anatomical Record* 38, 341-376.
- Lewis, F.T. (1943). The geometry of growth and cell division in epithelial mosaics. *Am J Bot* 30, 766-776.
- Milan, M., Campuzano, S., and Garcia-Bellido, A. (1996). Cell cycling and patterned cell proliferation in the wing primordium of *Drosophila*. *Proc Natl Acad Sci U S A* 93, 640-645.
- Patel, A.B., Gibson, W.T., Gibson, M.C., and Nagpal, R. (2009). Modeling and inferring cleavage patterns in proliferating epithelia. *PLoS Comput Biol* 5, e1000412.
- Rivier, N., Schliecker, G., and Dubertret, B. (1995). The stationary state of epithelia. *Acta Biotheoretica* 43, 403-423.
- Sahlin, P., Hamant, O., and Jönsson, H. (2009). Statistical Properties of Cell Topology and Geometry in a Tissue-Growth Model In *Complex Sciences: First International Conference, Complex 2009, Shanghai, China, February 23-25, 2009 Revised Papers, Part 1*, J. Zhou, ed. (Springer Berlin Heidelberg), pp. 971-979.
- Sahlin, P., and Jonsson, H. (2010). A modeling study on how cell division affects properties of epithelial tissues under isotropic growth. *PLoS One* 5, e11750.

## Supplementary Information

### I. Computation of $J_m$ in terms of power-law and exponential $F$ functions

To compute the quantity  $J_m$ , the expected number of dividing neighbors for an  $m$ -sided cell, for the case of a power-law function, we assume the following form for  $F$ :

$$F(N) = a(N - \xi)^Q \quad (3.S1),$$

where “ $a$ ” and “ $Q$ ” are constants, and  $N$  is the cell’s number of neighbors. The value  $\xi$  is slightly less than 4. For this case, the expression for  $J_m$  is the following:

$$J_m = \sum_{k=4}^9 \frac{mP(k)}{1 + (k - \xi)^{-Q} (m - \xi)^Q} \quad (3.S2).$$

For the case of the exponential function, we assume the following expression for  $F(N)$ :

$$F(N) = be^{aN} \quad (3.S3),$$

where “ $a$ ” and “ $b$ ” are constants, and  $N$  is the number of neighbors for the cell. In this case, the expression for  $J_m$  is the following:

$$J_m = \sum_{k=4}^9 \frac{mP(k)}{1 + e^{a(m-k)}} \quad (3.S4).$$

For the special case when “ $a$ ” is  $\gg 1$ , we find the following approximate formula:

$$J_m = m \left[ \frac{P(m)}{2} + \sum_{i=m+1}^9 P(i) \right] \quad (3.S5).$$

where  $P(m)$  is the fraction of  $m$ -sided cells in the overall cell population. For this case, all cells having  $m+1$  sides or greater, and  $\frac{1}{2}$  of cells having  $m$  sides are expected to divide prior to an arbitrarily selected  $m$ -sided cell, consistent with intuition.

## **Chapter 4**

### **Implications and future directions**

William T. Gibson<sup>1</sup>

(1) Program in Biophysics, Harvard University (Cambridge, MA 02138, USA)

## **Author contributions for Chapter 4**

Paper writing: WTG.

**Summary:** In this thesis, for a packed, proliferating monolayer cell sheet in which a balance between edge-length tensions and internal pressures generates cell shape, we have characterized a bi-directional feedback loop wherein neighbor cell shape and neighbor cell division exert topological and geometrical influences on each other via mitosis. Here, we consider the broader implications of our findings, as well as potential extensions to other systems, both biological and non-biological. We first discuss the degree to which non-standard division rules might influence the cleavage plane index, and then describe whether cleavage plane bias (Chapter 2) might have a three-dimensional analogue. Next, we consider the possibility of a mitotic shift (Chapter 3) in three dimensions. Last, we discuss whether inorganic networks, such as crack patterns or political territories, might also display a mitotic shift. Our discussion illustrates both the power and the limitations of a topological approach for analyzing proliferating cellular networks.

## ***Introduction***

In this thesis, we have presented two principle findings. First, in Chapter 2 we showed that in cell layers for which edge-length tensions and internal pressures generate cell shape, there is an emergent correlation between the long axis orientation of a dividing cell and the polygonal shapes of its immediate neighbors. This correlation partially derives from angular constraints on the packing relationships of neighboring polygons. For the case of a cell layer in which mitotic cleavage planes are oriented in a direction orthogonal to the cellular long axis, we predicted and empirically confirmed that cleavage planes are stochastically biased to cleave the cell's common interfaces with sub-hexagonal neighbors, and to avoid cleaving interfaces with super-hexagonal neighbors. Moreover, consistent with previous reports, we found that such biased cleavage planes are expected to increase the frequency of hexagons in a cell layer [1].

The second principle finding of this thesis (presented in Chapter 3) is that, in the context of a cell layer, only certain classes of division timing models for mitotic polygonal cells would result in a shifted distribution of mitotic cell shapes, as is observed both in the *Drosophila* wing disc epithelium and in the epidermis of the plant *Cucumis* [2-4]. Interestingly, we determined that the mere presence of a mitotic shift implies that the mitotic cell shape distribution of an epithelium is strongly constrained. In terms of a mechanistic understanding, we also found that the accumulation of cell-cell contacts due to neighboring cell divisions plays a strong role in generating the shift. While such influences may be sufficient to generate the shift, our analysis was not able to rule out the possible influence of mechanical or geometrical feedback on the cell cycle, as has been suggested by previous studies [3, 5].

Building on the results discussed in Chapters 2-3, here we consider the broader implications of our findings, as well as several possible extensions. First, we consider how altering the division rules might modify the cleavage plane bias. Next, we discuss three-dimensional extensions of the metrics developed in Chapters 2-3, as well as further implications of these metrics for cell shape evolution in three dimensional tissues. Finally, we consider the possibility of the mitotic shift in the context of non-biological networks. While speculative, our discussion will illustrate the potential strengths and limitations of the framework developed here for studying the more general space of proliferating cellular structures, both biological and non-biological.

## ***Cleavage plane bias in cell layers having non-standard division rules***

In Chapter 2, we analyzed cell divisions for which the orientation of mitotic cleavage is roughly orthogonal to the cellular long axis, which our data and previous studies suggest is consistent with the cell division patterns in both the *Drosophila* wing disc and the epidermis of *Cucumis*, among others [2, 6, 7]. Yet alternative division rules certainly exist. In particular, cells

in the dorsal epiblast of the zebrafish embryo divide with an orientation orthogonal to the short axis of the cell (rather than the long axis) and thus follow the exact opposite division rule. Moreover, this non-standard division rule requires the planar cell polarity pathway, and so is imposed by the molecular-genetic program [8]. Our unpublished simulation results suggest that such a division rule would actually create a cleavage plane bias with opposite orientation to that found in the *Drosophila* wing disc. In particular, cleavage planes would be expected to cleave common interfaces with super-hexagonal cells (such as octagons) with elevated frequency, whereas cleavage events would orient towards sub-hexagonal cells (such as quadrilaterals) with diminished frequency. Hence, the orientation of cleavage plane index may depend strongly on the particular division rule being implemented. In Chapter 2 we showed that noise in the cleavage plane orientation can weaken the cleavage plane bias generated by a long axis division mechanism. Intuitively, such effects would also be expected for the case of alternative rule sets, thus implicating division plane noise as a possible modulator of the strength of cleavage plane bias. Future work may elucidate the cleavage plane indices generated by the full spectrum of division rule sets [1, 6, 9-12].

### ***The possibility of cleavage plane bias in three dimensions***

A natural question concerns whether an analogue of the cleavage plane bias might exist in three dimensions, where cell-cell contacts are polygonal faces rather than linear edges, and cleavage planes are proper two-dimensional structures rather than lines or curves. Analysis is non-trivial for the three dimensional case, because the geometrical constraints on a packed system of convex polyhedral cells are considerably more complex than for the case of a two-dimensional cellular monolayer. We therefore propose that future work should first address this question computationally. Previous work has developed mechanical simulations of tightly packed, three-dimensional tissues [13, 14]. To probe the possible existence of a cleavage plane bias in three dimensions, the most direct approach would be to use a method analogous to the ellipse fitting procedure described for the two-dimensional case in Chapter 2. This procedure would involve fitting an ellipsoid to the three-dimensional cellular geometry, and then finding the intersection points between the faces of adjacent cells and a plane oriented orthogonal to the dividing cell's longest axis. Notably, more than two cells would be intersected by the cleavage plane, unlike in the two-dimensional case. If confirmed, a three-dimensional analogue of cleavage plane bias might have important implications for spindle orientation and cleavage plane orientation in multi-layer tissues.

As an example of an application in three dimensions, in a stem cell niche, packing geometry-mediated control of the mitotic spindle could in principle serve as a tumor suppressing mechanism. One recent study suggests that murine intestinal crypt shape is altered in the context of pre-cancerous APC mutations, which also have aberrant spindle orientations[15]. While not conclusive, this result suggests the possibility that neighbor cell shape could play a role in orienting stem cell divisions.

### ***The possibility of the mitotic shift in three dimensional tissues***

In Chapter 3, we described the conditions under which a mitotic shift can exist in a two-dimensional cell layer. In particular, we found that a mitotic shift cannot exist for two particular limiting cases: (1) the case of a memoryless division process and (2) the case of a perfectly synchronized tissue, wherein all cells proliferate in rounds simultaneously. While the range of cellular topologies in a three-dimensional tissue would be considerably greater than for the case of a monolayer cell sheet, the same arguments apply. That is, for a three-dimensional tissue at steady-state, the mitotic cell shape distribution (where "shape" refers to local tissue topology) would be identically equal to the overall distribution. Moreover, the same argument would hold

for the case of simultaneous and synchronized divisions. Thus, the limiting cases are similar for two- and three- dimensional systems.

While the above examples demonstrate the absence of a mitotic shift for perfectly random or perfectly synchronized divisions, it is far less clear what the actual mitotic cell shape distribution (or, indeed, the tissue-wide cell shape distribution) would look like for the case of a three-dimensional tissue in the intermediate range between perfectly random and perfectly synchronized cell divisions. A crude estimate is to assume a Gaussian-like distribution, which is actually a reasonable approximation for even the two-dimensional case [16]. Yet the two-dimensional side-gaining arguments that were used in Chapter 3 to model the emergence of the mitotic cell shape distribution may be insufficient to describe the emergence of the cell shape distribution in a three-dimensional tissue, where cell contacts are gained in terms of new cell faces, and more than two neighboring cells contact the cleavage plane. However, it is clear that even if the mitotic cell shape distribution were (for a particular division rule and physical model) a shifted version of the overall cell shape distribution in the three-dimensional case, it would certainly not be an integer shift of a single unit as it is for the two-dimensional case. To see this, note that for every round of divisions in which a population of  $N$  cells becomes  $2N$  cells (for large  $N$  in a convex tissue), more than  $2N$  neighbors are gained (more than one neighbor per cell), thus implying that the shift would be greater than unity. While we would not expect to see a single unit mitotic shift in three-dimensional tissues, a mitotic integer shift of multiple units remains a possibility.

### ***The possibility of a mitotic shift in non-biological systems***

Although this thesis has emphasized proliferation in biological cell layers, the physics community has long investigated diverse cellular systems in non-biological contexts [16-20]. In Chapter 3, we established two limiting cases under which a mitotic shift is impossible for a proliferating cell layer. The assumptions used for those arguments are sufficiently general so as to also guarantee applicability to non-biological cellular systems. However, few cellular systems, whether biological or non-biological, perfectly obey the rules imposed by these special cases. Rather, most proliferating cellular systems, such as crack patterns in cornstarch or territorial boundaries during human colonization of a land mass, display elements of both synchronization and stochasticity (our unpublished observations). For these cases, an important question is whether a mitotic shift would be expected. The analysis of Chapter 3 suggests that the presence or absence of a shift will depend heavily on the timing model and on the division rules being implemented, which must be determined empirically. Our preliminary investigation into networks formed by human colonization has yielded an interesting result, which is that, historically, county boundaries in the United States exhibited a partial mitotic shift during the gradual division of territories into counties, and then counties into smaller counties, over the course of American history. Thus, the mitotic cell shape distribution may also be shifted in some non-biological cellular networks. Certainly, the underlying processes driving mitosis are completely different in cracks versus counties or cells, but fundamental packing constraints restrict the topological dynamics of these systems, thus facilitating comparison across systems and scales. Future work will determine whether mitotic shifts are found in cornstarch cracks and in other networks that proliferate via fragmentation.

### ***Conclusions***

In this thesis, we have characterized a feedback between cell shape and the division process in adjacent polygonal cells. While the implications for simple, monolayer tissues are clear, much work remains to be done in order to establish whether the feedbacks examined in this thesis would apply to more complex, three dimensional tissues or to non-biological systems. An

equally important challenge will be to understand the emergent properties of such feedbacks in the context of multi-layer systems in which the constraints on cell packing geometry are non-trivial. A further challenge will be to integrate the analysis presented here with more sophisticated modeling and simulation methodologies, which could incorporate mechanical as well as active, biological influences. Combined with tissue engineering, stem cell reprogramming, and *in vitro* models of organ growth, we anticipate that in the future, such efforts will approach a systems-level theory of development.

## Chapter 4 References

1. Patel, A.B., et al., *Modeling and inferring cleavage patterns in proliferating epithelia*. PLoS Comput Biol, 2009. **5**(6): p. e1000412.
2. Lewis, F.T., *The Correlation Between Cell Division and the Shapes and Sizes of Prismatic Cells in the Epidermis of Cucumis*. The Anatomical Record, 1928. **38**: p. 341-376.
3. Aegerter-Wilmsen, T., et al., *Exploring the effects of mechanical feedback on epithelial topology*. Development, 2010. **137**(3): p. 499-506.
4. Gibson, M.C., et al., *The emergence of geometric order in proliferating metazoan epithelia*. Nature, 2006. **442**(7106): p. 1038-41.
5. Lewis, F.T., *The geometry of growth and cell division in epithelial mosaics*. American Journal of Botany, 1943. **30**(10): p. 766-776.
6. Gibson, W.T., et al., *Control of the mitotic cleavage plane by local epithelial topology*. Cell, 2011. **144**(3): p. 427-38.
7. Mao, Y., et al., *Planar polarization of the atypical myosin Dachs orients cell divisions in Drosophila*. Genes Dev, 2011. **25**(2): p. 131-6.
8. Gong, Y., C. Mo, and S.E. Fraser, *Planar cell polarity signalling controls cell division orientation during zebrafish gastrulation*. Nature, 2004. **430**(7000): p. 689-93.
9. Sahlin, P., O. Hamant, and H. Jönsson, *Statistical Properties of Cell Topology and Geometry in a Tissue-Growth Model in Complex Sciences: First International Conference, Complex 2009, Shanghai, China, February 23-25, 2009. Revised Papers, Part 1*, J. Zhou, Editor. 2009, Springer Berlin Heidelberg. p. 971-979.
10. Sahlin, P. and H. Jonsson, *A modeling study on how cell division affects properties of epithelial tissues under isotropic growth*. PLoS One, 2010. **5**(7): p. e11750.
11. Farhadifar, R., et al., *The influence of cell mechanics, cell-cell interactions, and proliferation on epithelial packing*. Curr Biol, 2007. **17**(24): p. 2095-104.
12. Besson, S. and J. Dumais, *Universal rule for the symmetric division of plant cells*. Proc Natl Acad Sci U S A, 2011. **108**(15): p. 6294-9.
13. Hutson, M.S., et al., *Cell sorting in three dimensions: Topology, fluctuations, and fluidlike instabilities*. Physical Review Letters, 2008. **101**(14).
14. Honda, H., M. Tanemura, and T. Nagai, *A three-dimensional vertex dynamics cell model of space-filling polyhedra simulating cell behavior in a cell aggregate*. Journal of Theoretical Biology, 2004. **226**(4): p. 439-453.
15. Quyn, A.J., et al., *Spindle orientation bias in gut epithelial stem cell compartments is lost in precancerous tissue*. Cell Stem Cell, 2010. **6**(2): p. 175-81.
16. Rivier, N., G. Schliecker, and B. Dubertret, *The stationary state of epithelia*. Acta Biotheoretica, 1995. **43**: p. 403-423.
17. Weaire, D. and N. Rivier, *Soap, Cells and Statistics - Random Patterns in 2 Dimensions*. Contemporary Physics, 1984. **25**(1): p. 59-99.
18. Bohn, S., L. Pauchard, and Y. Couder, *Hierarchical crack pattern as formed by successive domain divisions. I. Temporal and geometrical hierarchy*. Physical Review E, 2005. **71**(4).
19. Bohn, S., et al., *Hierarchical crack pattern as formed by successive domain divisions. II. From disordered to deterministic behavior*. Physical Review E, 2005. **71**(4).
20. Rivier, N. and A. Lissowski, *On the correlation between sizes and shapes of cells in epithelial mosaics*. J. Phys. A: Math. Gen., 1982. **15**: p. L143-L148.

## **Appendix A**

# **Topological characterization of wing disc epithelia in *Dachsous* mutant animals**

William T. Gibson<sup>1</sup>

(1) Program in Biophysics, Harvard University (Cambridge, MA 02138, USA)

**Author contributions for Appendix A**

Research/Paper Writing: WTG.

**Summary:** In this appendix, we describe the topological kinetics of the *Drosophila* wing imaginal disc in *Dachsous* mutant animals, in which cleavage plane orientations are randomized with respect to the global tissue axes. Such cleavage patterns stand in contrast to the wild-type situation, in which cleavage planes are globally polarized along the DV axis (and spindles are polarized along the AP axis) [1]. Based on analysis of fixed preparations, we infer that for the case of *Dachsous* mutant discs, the topological dynamics are very similar to those of wild type discs. In terms of cleavage plane bias (Chapter 2), the mitotic shift (Chapter 3), and the division kernel (Chapter 2 Extended Experimental Procedures), mutant dynamics are not noticeably different from wild-type dynamics either quantitatively or qualitatively. Our findings suggest: (1) that global control of mitotic cleavage plane orientations does not significantly affect topological dynamics and (2) that the means by which spindles are globally controlled in the wild type situation might involve local control of the cellular long axis. This latter conclusion is consistent with our own research (Chapter 2) and is supported by a theoretical/experimental study suggesting that planar polarized distribution of the atypical myosin Dachs might be the mechanism by which the cellular long axis is controlled [2, 3]. Our results suggest that cleavage plane bias (Chapter 2) may be minimally affected by global polarity in division plane orientation for this particular global control mechanism. However, we cannot rule out such influence for alternative mechanisms of global control, especially those mechanisms that are uncoupled from local cellular geometry.

## **Brief Introduction**

The atypical cadherin *Dachsous* is required for diverse developmental patterning programs at the larval, pupal, and adult stages. *Dachsous* functions either directly or indirectly at multiple levels of scale, and in the *Drosophila* wing disc alone is required for oriented cellular divisions, wild-type proportions and morphology, and wild-type cellular flows [1, 4, 5]. In the larval wing imaginal disc epithelium, a hetero-allelic *Dachsous* background based on the  $ds^{UA071}$  and  $ds^{36D}$  alleles results in randomized spindle orientations with respect to the global tissue axes, in contrast to the wild type case, in which cellular divisions are planar polarized [1]. The mathematical and computational analyses of topological dynamics explored in Chapters 2 and 3 neglect the complexity associated with global orientation of cellular divisions. Therefore, an important question is whether this added layer of molecular-genetic regulation would affect the topological dynamics of a cell layer. To test this, we examined fixed *Dachsous* mutant wing disc epithelia, and quantitatively scored topological dynamics based on a combination of statistical analysis, imaging, and manual scoring.

## **Methods**

To facilitate scoring and to visualize the septate junctions, we recombined both the  $ds^{UA071}$  and  $ds^{36D}$  mutant lines (each of which is carried over a CurlyO-Twist-Gal4 UAS-GFP balancer, abbreviated “CTG”) with a neuroglian-GFP trap line [1, 6]. Under the

dissecting scope, animals carrying only a *nrg*-GFP construct can be easily distinguished (under high magnification) from animals carrying both a *nrg*-GFP line and a CTG balancer, due to the latter construct's vastly more intense GFP signal, which is often punctuate. This distinction can be made easily even at 18° C, when the Gal4 expression is weakest. The genotypes for the two stock lines are as follows:

$\frac{nrg - GFP^{TRAP}}{y / nrg - GFP^{TRAP}}; \frac{ds^{UA071}}{CTG}$  and  $\frac{nrg - GFP^{TRAP}}{y / nrg - GFP^{TRAP}}; \frac{ds^{36D}}{CTG}$ . By crossing virgins of one line with males from the other line, we obtain viable larvae, pupae, and adults displaying a *Dachsous* phenotype, consistent with previous literature [1]. For examination of *Dachsous* mutant wing discs, we selected larvae having the following genotype(s) by selecting against the CTG balancer:  $\frac{nrg - GFP^{TRAP}}{y / nrg - GFP^{TRAP}}; \frac{ds^{36D}}{ds^{UA071}}$ . We verified that we could select such animals with 100% accuracy by allowing large numbers of them (> 50) to develop into adults, which always produced adults having *Dachsous* mutant phenotypes (a wide body, rounded wings, and short, stubby legs, among others).

To test for altered topological dynamics, we scored 200 dumbbell-shaped cytokinetic figures (Figure A1B) from the wing imaginal discs of *Dachsous* mutant animals. Wing discs were dissected in Ringer's solution from third-instar wandering larvae and fixed in 4% paraformaldehyde in PBS. Discs were mounted in 70% glycerol/PBS, and imaged on a Leica SP2 with 63X glycerol objective. Dumbbell-shaped cytokinetic figures were scored in multiple focal planes to ensure accuracy of topological scorings. Digitally scored images of the individual cytokinetic figures (1 for each figure) are archived at the following address: [http://eecs.harvard.edu/group/ssr/tyler-archive/DS\\_Dumbbells](http://eecs.harvard.edu/group/ssr/tyler-archive/DS_Dumbbells).

## Results

### ***Dachsous* mutant animals exhibit a wild-type cleavage plane index**

We hypothesized that if the spindle orientations of dividing cells are oriented by a global mechanism that acts independently of cell shape, then cleavage plane bias (Chapter 2) might act in opposition to this competing mechanism, resulting in a diminished cleavage plane bias in wild type wing discs. We therefore reasoned that in a *Dachsous* mutant background where this global orienting cue is knocked out, we might expect to unmask the stronger default cleavage plane bias. To test whether the cleavage plane index might be altered in *Dachsous* mutant wing disc epithelia, we computed the cleavage plane index from 200 dumbbell-shaped cytokinetic figures (Figure A1B) in *Dachsous* mutant discs (see methods; see also Chapter 2 for a full treatment of the cleavage plane index). We obtained a negative result (Figure A2). Preliminary data suggests that the cleavage plane bias in *Dachsous* mutant discs is very similar or nearly identical to the bias measured in wild type tissue. This suggests that the mechanism orienting the global distribution of spindle orientations may be locally controlled via cell shape, consistent with our work in Chapter 2 and with modeling and experimental work implicating the atypical myosin Dachs as a possible

orienting cue [2, 3]. To conclude, in this particular system, cleavage plane bias probably does not act in opposition to the mechanism globally orienting mitotic spindles and cleavage planes. Rather, we suggest that cleavage plane bias and global control of mitotic spindles are produced by the same mechanism, which may act locally and correlate with local cell shape.

### ***Dachsous mutant animals exhibit a mitotic shift.***

To investigate whether *Dachsous* might have altered cell shape dynamics in spite of having a normal cleavage plane index, we tested whether *Dachsous* mutant wing discs might display an altered mitotic shift (the subject of Chapter 3). Based on the 200 dividing cells discussed in the previous section, we plotted the frequencies of the individual polygon classes for dividing cells. For comparison, we plotted both the overall distribution of polygon cell shapes in *Dachsous* discs and the distribution of neighbor cell shapes (ie, the cell shapes neighboring cytokinetic figures). As in wild-type wing discs, we observe a shifted distribution of shapes for the mitotic cells (Figure A3). Without further analysis, it is not possible to determine whether the shapes of the overall and mitotic cell shape distributions are significantly different from those of wild-type organisms. Such differences, if they exist, are subtle.

### ***Dachsous mutant wing disc cells exhibit a division kernel that is not noticeably different from the wild type case.***

To test whether *Dachsous* mutant wing disc cells might have an altered division kernel (which is a matrix describing the probability that an  $m$ -sided cell gives rise to a  $j$ -sided daughter, where  $m$  and  $j$  are arbitrary; see Chapter 2 Extended Experimental Procedures for a full treatment), we computed the division kernel from the same set of 200 dumbbell-shaped cytokinetic figures. In wild-type wing discs, 80% of dividing cells exhibit maximally symmetric topological cell divisions (based on 420 dividing cells). In *Dachsous* mutant wing discs, we find that 85% of divisions are maximally symmetric (based on 200 dividing cells). Hence, the topological symmetry of cell divisions does not appear to be noticeably altered in *Dachsous* mutant discs. To conclude, the topological dynamics of *Dachsous* mutant discs are not only similar to those of wild-type organisms in terms of the cleavage plane index and the mitotic shift, but also in terms of the division kernel.

### ***Triangular cells are more frequent in Dachsous mutant discs***

Empirically, we find that triangular cells, which are absent in wild-type discs, are more frequent in *Dachsous* mutant discs. While the percentage of such cells is extremely small, the very presence of triangles is noteworthy because it suggests one of the following: (1) increased cell-cell rearrangement, (2) a partial disruption of the division kernel, or (3) altered cell cycle dynamics. Yet our data suggest that the topological kinetics are roughly normal. Resolving this issue will require further analysis. In particular, we suggest that time-lapse imaging may help to resolve whether subtle differences in topological kinetics produce this phenotype, or whether other, more complex mechanisms are responsible.

## ***Conclusions and implications***

The results presented here are preliminary, but they suggest that the topological kinetics of an epithelial sheet are not dramatically altered in *Dachsous* mutant discs. On a preliminary basis, we suggest that the topological analysis developed in Chapters 2-3 may not be very sensitive to at least some classes of oriented cell division. Here, the proposed mechanism governing oriented cell division is believed to be local control of the cellular long axis [2, 3]. Future work should more thoroughly investigate the degree to which topological dynamics are uncoupled from oriented cell division under different theoretical mechanisms governing oriented cell division.

To this end, we suggest that spatially explicit, finite-element simulators could be compared with time-lapse movies of proliferating tissues. Of particular interest would be the relationship between the orientation of a dividing cell with respect to the global tissue axes and the lengths of its edges as a function of that orientation. Depending on whether oriented cell division occurs according to division of the cellular long axis (as occurs in *Drosophila*), or division of the cellular short axis (as occurs in the Zebrafish dorsal epiblast), different topological dynamics might be expected [2, 3, 7]. For instance, repeated divisions of the cellular short axis might enrich for very short edge lengths, and thus increase the rate of cellular rearrangement, or alter the cleavage plane index or division kernel. Such spatial feedbacks constitute an important avenue for future work.

**Figure A1**

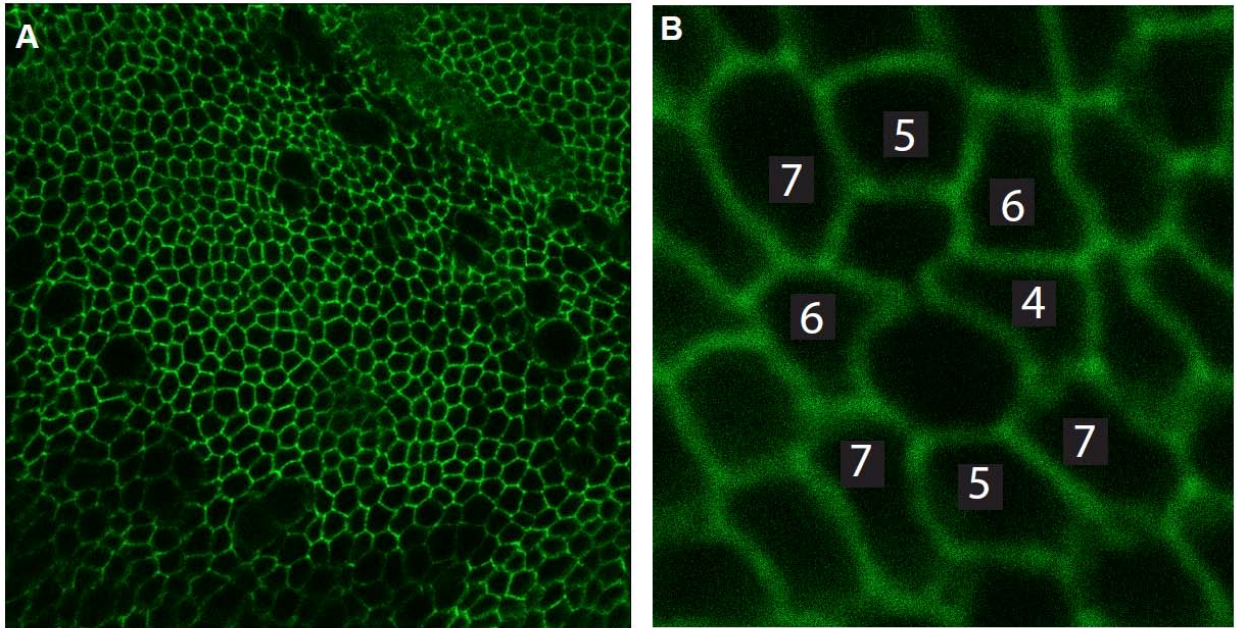


**Figure A1: Epithelial morphology in *Dachsous* mutant animals.** **(A)** A third instar wing imaginal disc epithelium containing the following combination of mutant *Dachsous* alleles:  $ds^{UA071}$  and  $ds^{36D}$ . Septate junctions (*green*) are marked with neuroglian-GFP [6]. Note the regularity of the polygonal cell shapes in this mutant background. **(B)** A dumbbell-shaped cytokinetic figure in the same hetero-allelic mutant background. Note that the cell shapes are less regular in this particular disc and/or region of the tissue. This may represent mixed penetrance of the cell shape regularity phenotype.

**Figure A2**

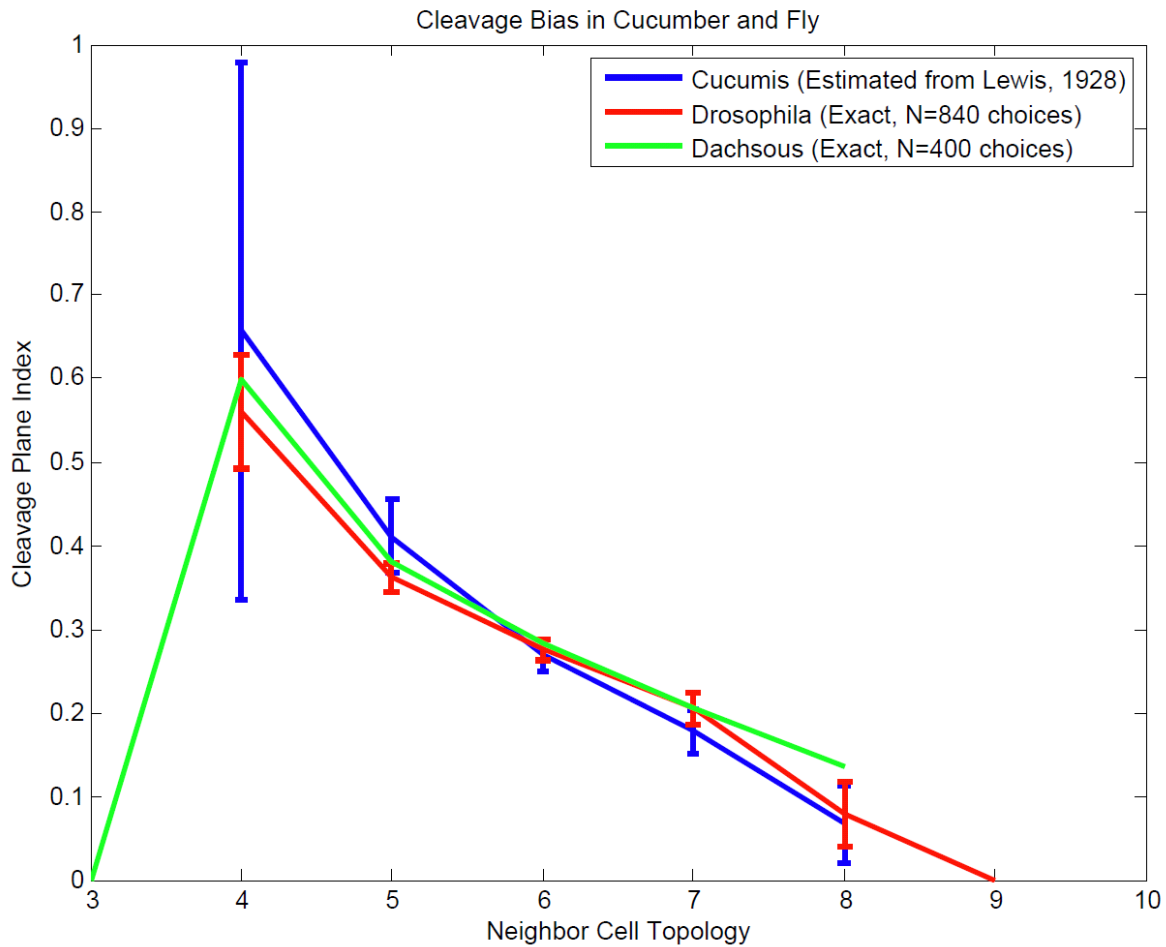


**Figure A2: *Dachsous* mutant animals exhibit a wild-type cleavage plane index curve:** Preliminary analysis of 200 dumbbell-shaped cytokinetic figures suggests that the cleavage plane index is unaltered in *Dachsous* mutant epithelia (*green*) when compared with wild-type tissue (*red*). Error bars are not shown for *Dachsous* mutant animals. Exact scorings of all figures can be found at the following address: [eecs.harvard.edu/group/ssr/tyler-archive/DS\\_Dumbbells](http://eecs.harvard.edu/group/ssr/tyler-archive/DS_Dumbbells). Error bars would be expected to be significantly greater for the *Dachsous* measurements, because the sample size is less than half as large as for the wild type case. Note that 3-sided neighbors are more common in *Dachsous* animals, although it is unclear whether cleavage planes bias in their direction (the sample size is very small).

**Figure A3**

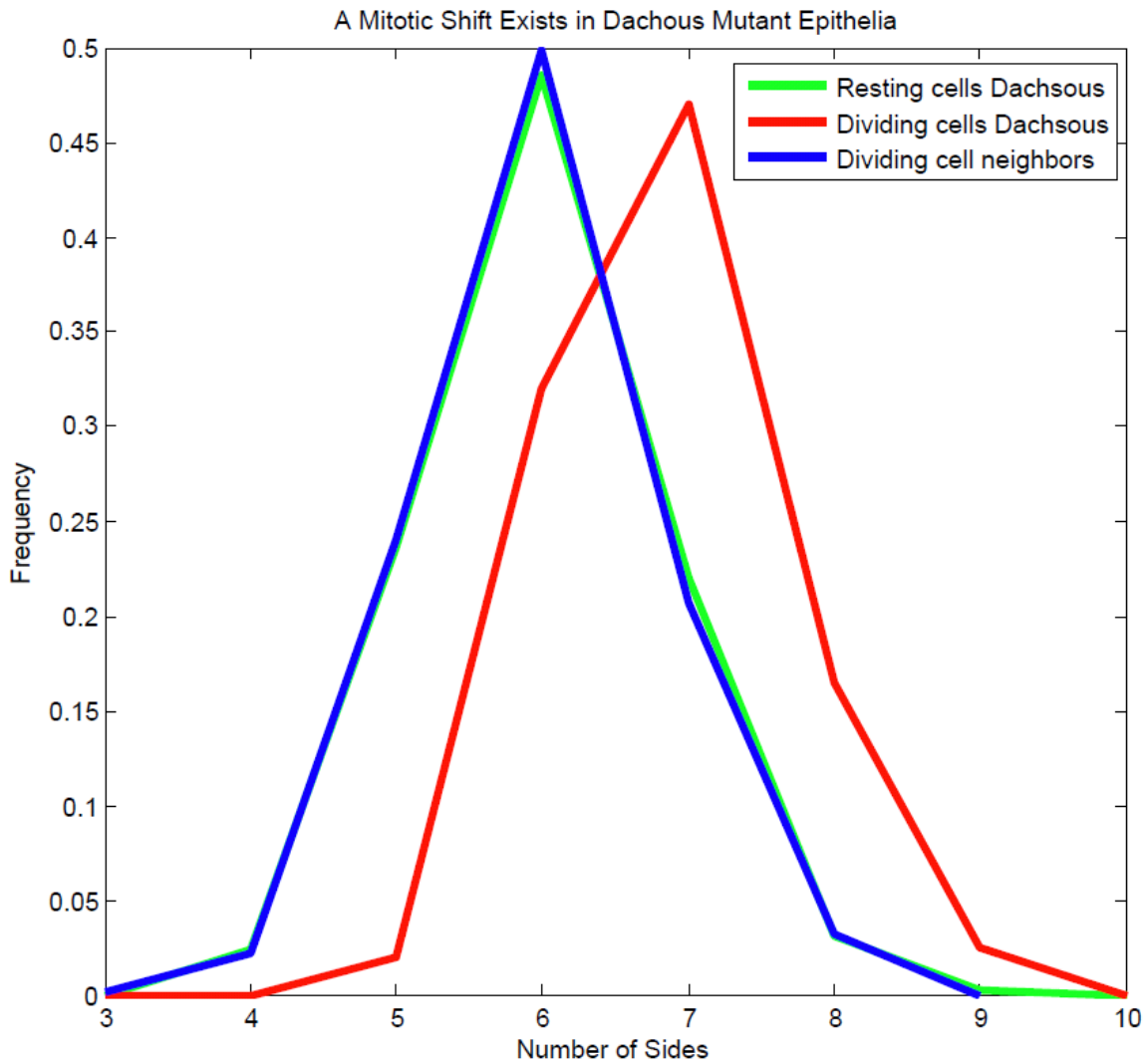


**Figure A3: *Dachsous* mutant animals exhibit a mitotic shift:** Preliminary analysis of 200 dumbbell-shaped cytokinetic figures suggests that the mitotic is present in *Dachsous* mutant epithelia (compare the distribution of mitotic cells, depicted in *red*, and the overall distribution of cellular shapes, depicted in *blue*).

## References:

1. Baena-Lopez, L.A., A. Baonza, and A. Garcia-Bellido, *The orientation of cell divisions determines the shape of Drosophila organs*. *Curr Biol*, 2005. **15**(18): p. 1640-4.
2. Mao, Y., et al., *Planar polarization of the atypical myosin Dachs orients cell divisions in Drosophila*. *Genes Dev*, 2011. **25**(2): p. 131-6.
3. Gibson, W.T., et al., *Control of the mitotic cleavage plane by local epithelial topology*. *Cell*, 2011. **144**(3): p. 427-38.
4. Aigouy, B., et al., *Cell flow reorients the axis of planar polarity in the wing epithelium of Drosophila*. *Cell*, 2010. **142**(5): p. 773-86.
5. Strutt, D., *Organ shape: controlling oriented cell division*. *Curr Biol*, 2005. **15**(18): p. R758-9.
6. Morin, X., et al., *A protein trap strategy to detect GFP-tagged proteins expressed from their endogenous loci in Drosophila*. *Proc Natl Acad Sci U S A*, 2001. **98**(26): p. 15050-5.
7. Gong, Y., C. Mo, and S.E. Fraser, *Planar cell polarity signalling controls cell division orientation during zebrafish gastrulation*. *Nature*, 2004. **430**(7000): p. 689-93.

## **Appendix B**

### **Current and future directions for the Twin Spot Generator and Split Gal4 clone induction systems.**

William T. Gibson<sup>1,2</sup>, Dong Yan<sup>2</sup>, Ruth Griffin<sup>2</sup>, Christians Villalta<sup>2</sup>, Richard Binari<sup>2</sup>, and  
Norbert Perrimon<sup>2</sup>

(1) Program in Biophysics, Harvard University (Cambridge, MA 02138, USA)

(2) Department of Genetics, Harvard Medical School (Boston, MA 02115)

## **Author contributions for Appendix B**

Imaging, clone induction, and staining: WTG, DY

Paper writing: WTG

Design & direction of research: NP

DNA constructs: RG

DNA construct injection: CV

Fly line construction: RB, RG, WTG

**Summary:** In this appendix, we discuss current progress and future directions for baseline testing, optimization, and application of the Twin Spot Generator (TSG) and Split Gal4 systems to problems of growth and tissue topology. We first discuss a biological application, measurement of sibling clone noise, for which such systems are uniquely positioned to provide new, biological insight about *in vivo* cell cycle variability in sibling daughter cells and their progeny. Next, we describe the technical state of the most recent version of the system, the Gal4::VP16 version of the Split Gal4 system. In particular, we address the death of UAS-CD8::GFP labeled clones, and discuss potential interpretations and follow-up experiments. We also discuss whether cell death in the CD8::GFP clones could be suitable for use as a cell-competition model. Finally, we conclude with a technical description of the lines being built for the next set of experiments. This appendix is intended to provide technical context and ideas for biological application to scientists who are beginning to work with the TSG and/or Split Gal4 systems.

## **Introduction**

Clonal analysis based on heritable cell labeling is a powerful method for studying developmental processes in *Drosophila*, *Mus musculus*, and *Arabidopsis*, with applications ranging from stem cell biology to growth control and neuroscience [1-10]. In *Drosophila*, two viable, independent approaches have been recently developed to fluorescently label both a clone and its adjacent twin-spot following the division of the original mother cell in which the dual clone induction event occurred [1, 9, 10]. Such systems are functionally similar to the MADM tools developed for use in mice [11, 12]. In particular, the Twin-Spot Generator approach provides an elegant double-labeling system in which mutations can be easily recombined onto one or more of the chromosomal arms into which the system has been inserted, thus providing a spatially local and temporally synchronized internal control clone with which to compare mutant clonal phenotypes[1]. While such applications are feasible in principle using the Twin Spot MARCM method, the latter method's greater complexity prevents routine use as a labeling stock with which to recombine mutations [9].

In order to synergistically combine Twin-Spot Generator capabilities with the Gal4-UAS system, recently a Split-Gal4 system has been developed, which drives Gal4 expression in one of the two sibling clones (RG and NP, unpublished) [13]. In combination with UAS-based RNAi hairpin over-expression and/or other UAS-based over-expression constructs, the Split Gal4 system permits screening of RNAi-based or over-expression based phenotypes alongside a temporally synchronized, spatially local internal control. In the context of cell competition, such capabilities will permit quantitative assessment of relative shape and size differences in local, competing cell populations descended from a single progenitor.

While the advantages of the TSG and Split Gal4 systems are clear, these systems are still being optimized technically so as to maximally leverage their capabilities for particular biological applications. Here, we first propose a biological application for which this system can be uniquely and powerfully applied in a particular developmental context (sibling clone noise in the *Drosophila* larval wing disc). Next, we describe the

technical state of the current version of the system, which uses Gal4::VP16. Using a UAS-CD8::GFP marker for the Gal4-specific clone, we describe a cell death phenotype in the GFP cells based on Caspase-III staining. We offer interpretation for the basis of this phenotype. Finally, we discuss follow-up experiments, and describe fly lines being built for that purpose. Our discussion is framed as an introduction for scientists planning to use TSG-based or Split-Gal4 based approaches for developmental applications.

### ***An application for the TSG and/or Split Gal4 systems: Sibling clone noise***

The TSG and Split Gal4 systems will be useful for an unlimited range of developmental applications, but they are ideally suited for studying variability in clone growth due to cell cycle noise during proliferation. Such noise is an intrinsic property of growth and is a fundamental application for which these systems are uniquely suited. While the Split Gal4 system permits characterizing such noise under asymmetric, local RNAi perturbations, characterizing this noise in the wild type situation (in the absence of RNAi hairpins) may be maximally informative (Eric Wieschaus, personal communication). By comparing the sibling clone noise present in *Drosophila* wing discs based on TSG measurements with the sibling clone noise present in murine tissues based on MADM measurements, it may be possible to pursue general statements about sibling clone noise -- and growth more generally -- using these doubly marked systems.

Flp-Out based clone induction in the *Drosophila* wing disc suggests that clonal proliferation in this tissue is stochastic. Indeed, some cells have divided multiple times before others have divided even once [14]. The evidence for this claim derives from the distribution of clone sizes (in terms of the number of cells in the clone), which is variable, even when clone induction takes place over a brief time interval [14]. The following two alternative hypotheses can also explain this data: (1) cell-cell rearrangement and (2) simultaneous, independent induction of Flp-Out events in neighboring cells. The first hypothesis can be ruled out as a primary explanation based on live-imaging of the wing imaginal disc (in which cell-cell rearrangements are almost never observed), and also based on the contiguity of large clones (ie, clones resulting from many cell divisions rarely exhibit single, non-contiguous clonally marked cells in the immediate surrounding tissue, suggesting that marked cells do not separate from the clone) [15, 16]. The second hypothesis can be ruled out on statistical grounds. If the probability of a clone induction event is very rare, then the probability of two adjacent clone induction events is ultra-rare (and can be neglected for sufficiently short induction periods). Supporting this reasoning, previous work suggests that there are not local regions of the disc which especially favor clone induction [17]. Therefore, we conclude that cell cycle times are noisy in this tissue, thus raising the issue of how such noise can be measured.

The TSG and Split Gal4 systems are ideal for measuring clonal noise, because they include a temporally synchronized, spatially local internal control. Importantly, for sibling clones there is zero uncertainty about the time point of induction; sibling clones derive from the same mother cell, which underwent FRT-mediated recombination at a single point in time. By contrast, when we compare the relative clone sizes of Flp-Out

clones within a single disc, it is unclear whether differences in clone sizes may reflect differences in the time of clone induction, because inductions occur at random time points during heat shock. Therefore, the TSG system reduces measurement noise by eliminating heterogeneity in the pair-wise ages of clones to be compared. This distinction would be especially important if cell cycle times were very noisy (ie far from uniform), because small initial differences in clone size could grow over time. Hence, these systems facilitate quantitative measurement of intrinsic cell cycle noise *in vivo* and offer greater accuracy than conventional clone induction methods.

The Carl Zeiss microscope recently purchased by the Perrimon lab would provide an added technological boost for scoring many TSG clones simultaneously. This microscope permits taking stacks through a large number of wing discs mounted on a slide and then stitching the images together, thus permitting rapid acquisition of clonal data. Moreover, the ability to scroll through the stacks, and hence, the depth of the tissue offline, permits fine discrimination between individual cells and increased certainty in identifying labeled versus unlabeled cells at the borders of clones. The latter capability also permits scoring of cells in cases for which interkinetic nuclear migration obscures neighbor relationships. Thus, the data acquisition phase could be greatly expedited.

### ***Comparison with MADM-based measurements in mice & formulation of simple quantitative models***

To complement the above measurements, a second source of data from an alternative, mammalian system can be obtained using the original MADM system in murine tissues. An interesting systems biology question to address concerns how similar the dynamic clone size distributions are in the two organisms when time is re-scaled so that the average number of divisions per cell per time is the same in the two animals. If the re-scaled sibling clone noise were similar in flies and in mice, given the long span of evolutionary time between these two organisms, this might suggest fundamental constraints on clone growth. Such work could be complemented by very simple mathematical analysis of the clone growth process for the two organisms. In brief, the cross-comparison between these two distantly related organisms could be a rich source of fundamental information about proliferation dynamics that would be most powerfully revealed by these doubly marked systems.

### ***Current state of the Split-Gal4 system***

As tested, the Split-Gal4 system currently works as intended. That is, induced clones either show Gal4 expression (as assessed based on UAS-CD8::GFP reporter) and UAS-RFP expression in cells simultaneously (due to either G1 or G2 recombination or G2-Z segregation), or one of the above in each of two separate sibling clones (due to G2-X segregation). While the system currently works in this regard, we see a phenotype that appears to be localized in the Gal4 expressing cells. In particular, based on Caspase-III staining and qualitative assessment, we notice cell death at an elevated rate in Gal4 clones in comparison with their larger RFP counterparts at 25° C. Caspase-III staining (which uses the same 2° anti-body as anti-RFP) is unambiguous,

and was confirmed by close inspection of individual channel images. It is definitely not an artifact of bleed-through from the GFP channel. Moreover, widespread tiny vesicles of GFP bits are observable in surrounding cells (Figure B1), thus suggesting engulfment of the green cells. Caspase-III staining is almost never observed in exclusively red clones, but is frequently observable in both green clones and in yellow clones (Figure B2). During G2-X segregation, one copy of the construct undergoes recombination, and the other does not [1]. This latter observation argues against the hypothesis that toxic, un-recombined intermediate proteins are responsible for the cellular death, because in yellow clones both protein forms are properly recombined. Moreover, the phenotype is not due to a gain of function effect in the RFP cells, because surrounding “unlabeled” cells expressing both “unrecombined” proteins do not undergo cell death. The cause of the increase in cell death is currently unknown.

In the present version of the system, Gal4 expression is based on Gal4 VP16. To test whether the phenotype can be rescued by using a lower temperature, and thus reducing the Gal4 expression, we repeated clone induction and raised larvae at 18°C. Notably, we did not see an obvious reduction in the cell death phenotype at 18°C (data not shown). To test whether over-expression of dMyc could rescue the Gal4 clones, we merged the Split Gal4 system with a line containing UAS-dMyc on Chromosome II [18]. Preliminary data is inconclusive about whether this experiment resulted in partial rescue, because induced clones were not sufficiently large. These experiments will need to be re-examined at 48 hours post heat shock or later for more conclusive evidence. A balanced stock exists from which homozygous individuals can be selected for the experiment. The existing line is as follows:

$$\frac{w[*]/w^-}{y}; \frac{UAS-dMyc}{CyO}; \frac{TSG\#77C4}{TM6B}.$$

These stocks were transferred to author RG during the summer, and are available for immediate use.

It is theoretically possible (although unlikely) that CD8::GFP is causing the cell death observed in the green and yellow clones. To directly test this hypothesis, one could build a Split Gal4 line using Lac-Z instead of CD8::GFP.

For purposes of testing whether blocking cell death is sufficient to rescue the Gal4 clones, the key experiment is to over-express P-35 in the GFP labeled cells. Construction of lines containing UAS-P35 was begun in the spring, and the intermediate lines were transferred to author RG during the summer. The complete crossing scheme is as follows:

$$\text{♂} \frac{w^{[*]}}{y}; \frac{UAS - P35}{UAS - P35}; + \times \text{♀}^v w^{-}; \frac{If^{-}}{CyO}; \frac{MKRS}{TM6B} \quad (\text{Cross 1A})$$

$$\text{♂} \frac{w^{[*]}}{y}; \frac{UAS - P35}{CyO}; \frac{+}{TM6B} \times \text{♀}^v \frac{w^{[*]}}{w^{-}}; \frac{UAS - P35}{CyO}; \frac{+}{TM6B} \quad (\text{Cross 1B})$$

$$\text{♂} \frac{w^{[*]}/w^{-}}{y}; \frac{UAS - P35}{UAS - P35}; \frac{+}{TM6B} \quad (\text{Product 1})$$

$$\text{♂} \frac{w}{yw/y}; \frac{UAS - dmyc}{CyO}; \frac{TSG6\#77C4}{TM6B} \times \text{♀}^v w^{-}; \frac{If^{-}}{CyO}; \frac{MKRS}{TM6B} \quad (\text{Cross 1A'})$$

$$\text{♂} \frac{w^{-}}{y}; \frac{If^{-}}{CyO}; \frac{TSG6\#77C4}{TM6B} \times \text{♀}^v \frac{w^{-}}{yw/w}; \frac{If^{-}}{CyO}; \frac{TSG6\#77C4}{TM6B} \quad (\text{Cross 1B'})$$

$$\text{♀}^v w^{-}/yw/w; \frac{If^{-}}{CyO}; \frac{TSG6\#77C4}{TSG6\#77C4} \quad (\text{Product 1'})$$

$$\text{♂} \frac{w^{[*]}/w^{-}}{y}; \frac{UAS - P35}{UAS - P35}; \frac{+}{TM6B} \times \text{♀}^v w^{-}/yw/w; \frac{If^{-}}{CyO}; \frac{TSG6\#77C4}{TSG6\#77C4} \quad (\text{Cross 2A})$$

$$\text{♂} \frac{w^{-}/yw/w}{w^{-}/yw/w}; \frac{UAS - P35}{CyO}; \frac{TSG6\#77C4}{TM6B} \times \text{♀}^v \frac{w^{-}/yw/w}{y}; \frac{UAS - P35}{CyO}; \frac{TSG6\#77C4}{TM6B} \quad (\text{Cross 2B})$$

$$\text{♂} / \text{♀}^v \frac{w^{-}/yw/w}{\parallel/y}; \frac{UAS - P35}{UAS - P35}; \frac{TSG6\#77C4}{TSG6\#77C4} \quad (\text{Product 2}).$$

## ***Split Gal4 and cell competition***

One hypothesis to explain the Gal4 clone-specific cell death phenotype is that the GFP cells in the Split Gal4 system simply grow and divide more slowly and are out-competed by their RFP-labeled twin spot and surrounding wild-type cells. Currently, this hypothesis cannot be ruled out. If dMyc over-expression were sufficient to rescue the Gal4 clones or to turn these clones into super-competitors, this would be consistent with the cell competition hypothesis. As mentioned above, lines to test this hypothesis already exist and have been used to induce clones. These are available for immediate use.

At the same time, complex, ambiguous results are also possible. For instance, even if the Gal4 clones out-compete the neighboring cells (red and non-colored) when over-expressing dMyc, they still might undergo intrinsic cell death themselves. If the Gal4 cells have an intrinsic cell death phenotype, our results suggest that it is a time-delayed effect. Therefore, in this case, one might observe increased cell death in the red clones and clear surrounding cells at early stages, but relatively higher cell death in the green clones later on. An important control will be to make sure that blocking cell death using P35 over-expression is sufficient to fully suppress the phenotype. If this is not the case, then cell competition by itself is unlikely to explain the cell death phenotype. The intermediate P35 lines were transferred to author RG while under construction (see the crossing sequence, above). Either the intermediate lines, or a later stage, are available for use, but the final test stocks are not yet available.

***Discussion:*** Doubly marked clones represent an important step forward for *in vivo* characterization of developmental processes. Here we have proposed a biological application for doubly marked clones in order to maximally leverage the distinct information that they yield about stochasticity in the cell cycle as it pertains to stochasticity in clone size. We have also provided a description of the current state of the Split Gal4 system, which has many other applications beyond the study of sibling clone noise. Last, we have proposed future experiments in order to further characterize the dynamics of the current version of the Split Gal4 system. Future iterations of this system will use alternative markers such as mCherry, alternative non-VP16 Gal4 drivers, and complementary drivers such as LexA and Gal4 in the apposed clones. Such improvements will extend the scope of application to live imaging, cell competition, and growth control screens.

**Figure B1**

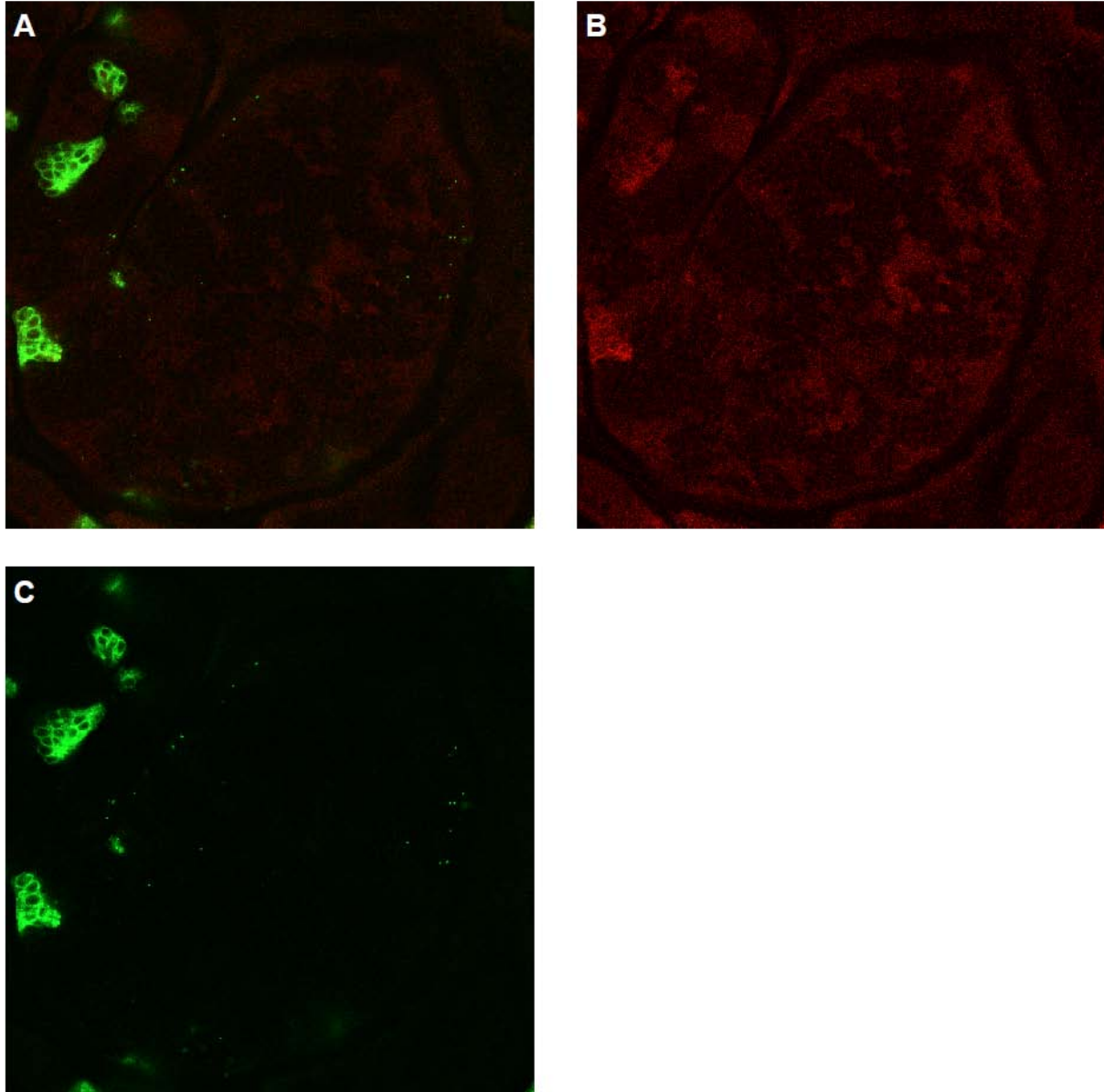


**Figure B4:** A phenotype is observed in the GFP-positive cells in the Split-Gal4 system. UAS-CD8::GFP is driven by a Gal4 VP16 construct. RFP has been stained with anti-dsRed. (A) Overlay of the GFP channel with the RFP channel reveals that red cells outnumber green cells. Note the punctate nature of the remaining bits of green cells. (B) The RFP channel. Brightness has been adjusted using Adobe Photoshop. (C) The GFP channel.

**Figure B2**

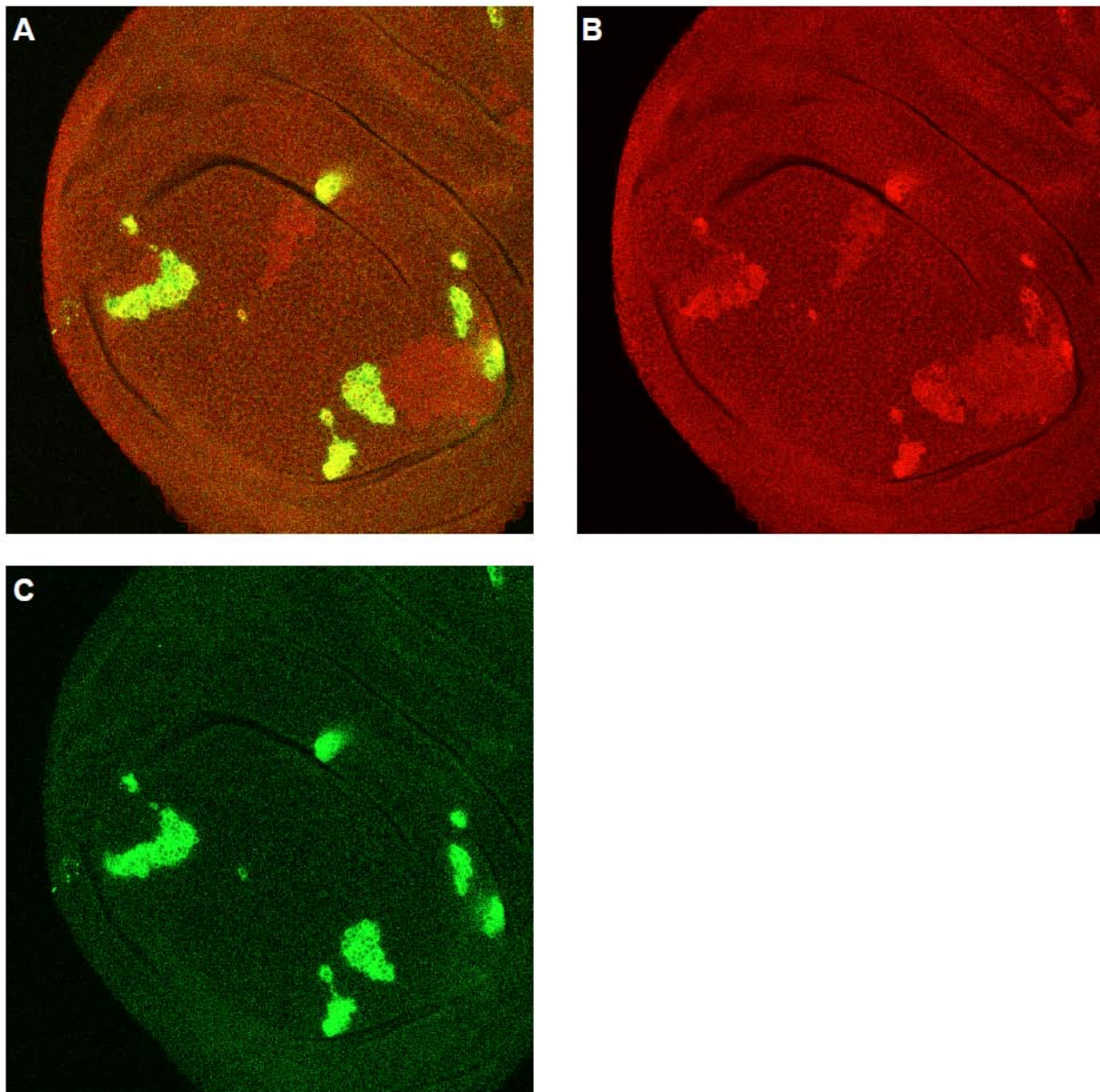


**Figure B5:** Caspase-III staining is concentrated in green and yellow (green+red) clones. UAS-CD8::GFP marks Gal4::VP16 clones. Red clones are stained with anti-dsRed. Caspase and RFP clones (red channel) are marked by different primary antibodies but the same secondary antibody. (A) An overlay of the red & green channels. The red channel includes both Caspase staining and anti-RFP staining. (B) The red channel. Very bright red indicates Caspase staining. Dull red indicates RFP staining. (C) The green channel. Green indicates the presence of UAS-CD8::GFP.

## References for Appendix B:

1. Griffin, R., et al., *The twin spot generator for differential Drosophila lineage analysis*. Nat Methods, 2009. **6**(8): p. 600-2.
2. Hadjieconomou, D., et al., *Flybow: genetic multicolor cell labeling for neural circuit analysis in Drosophila melanogaster*. Nat Methods, 2011. **8**(3): p. 260-6.
3. Hampel, S., et al., *Drosophila Brainbow: a recombinase-based fluorescence labeling technique to subdivide neural expression patterns*. Nat Methods, 2011. **8**(3): p. 253-9.
4. Livet, J., et al., *Transgenic strategies for combinatorial expression of fluorescent proteins in the nervous system*. Nature, 2007. **450**(7166): p. 56-62.
5. Struhl, G. and K. Basler, *Organizing activity of wingless protein in Drosophila*. Cell, 1993. **72**(4): p. 527-40.
6. Lee, T. and L. Luo, *Mosaic analysis with a repressible cell marker for studies of gene function in neuronal morphogenesis*. Neuron, 1999. **22**(3): p. 451-61.
7. Lee, T. and L. Luo, *Mosaic analysis with a repressible cell marker (MARCM) for Drosophila neural development*. Trends Neurosci, 2001. **24**(5): p. 251-4.
8. Wachsman, G., R. Heidstra, and B. Scheres, *Distinct cell-autonomous functions of RETINOBLASTOMA-RELATED in Arabidopsis stem cells revealed by the brother of brainbow clonal analysis system*. Plant Cell, 2011. **23**(7): p. 2581-91.
9. Yu, H.H., et al., *Twin-spot MARCM to reveal the developmental origin and identity of neurons*. Nat Neurosci, 2009. **12**(7): p. 947-53.
10. Yu, H.H., et al., *A complete developmental sequence of a Drosophila neuronal lineage as revealed by twin-spot MARCM*. PLoS Biol, 2010. **8**(8).
11. Zong, H., et al., *Mosaic analysis with double markers in mice*. Cell, 2005. **121**(3): p. 479-92.
12. Liu, C., et al., *Mosaic analysis with double markers reveals tumor cell of origin in glioma*. Cell, 2011. **146**(2): p. 209-21.
13. Brand, A.H. and N. Perrimon, *Targeted gene expression as a means of altering cell fates and generating dominant phenotypes*. Development, 1993. **118**(2): p. 401-15.
14. Milan, M., S. Campuzano, and A. Garcia-Bellido, *Cell cycling and patterned cell proliferation in the wing primordium of Drosophila*. Proc Natl Acad Sci U S A, 1996. **93**(2): p. 640-5.
15. Gibson, W.T., et al., *Control of the mitotic cleavage plane by local epithelial topology*. Cell, 2011. **144**(3): p. 427-38.
16. Gibson, M.C., et al., *The emergence of geometric order in proliferating metazoan epithelia*. Nature, 2006. **442**(7106): p. 1038-41.
17. Dubatolova, T. and L. Omelyanchuk, *Analysis of cell proliferation in Drosophila wing imaginal discs using mosaic clones*. Heredity, 2004. **92**(4): p. 299-305.
18. de la Cova, C., et al., *Drosophila myc regulates organ size by inducing cell competition*. Cell, 2004. **117**(1): p. 107-16.